

A
QC
851
S6
NO.72-
12
c.1

12

December 1972

A NUMERICAL EXPERIMENT ON THE SIMULATION AND
MODIFICATION OF HURRICANE RAINBAND CLOUDS

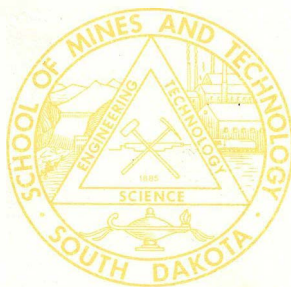
FINAL REPORT

By: H. D. Orville, W. J. Chang, and F. J. Kopp

Prepared for:

National Hurricane Research Laboratory
National Oceanic & Atmospheric Administration
Coral Gables, Florida 33124

Contract No. N22-3-72(G)



Institute of Atmospheric Sciences
South Dakota School of Mines and Technology
Rapid City, South Dakota 57701

A
QC
851
S6
no. 72-1
e.1

Report 72-12

December 1972

A NUMERICAL EXPERIMENT ON THE SIMULATION AND
MODIFICATION OF HURRICANE RAINBAND CLOUDS

FINAL REPORT

By: H. D. Orville, W. J. Chang, and F. J. Kopp

Prepared for:

National Hurricane Research Laboratory
National Oceanic & Atmospheric Administration
Coral Gables, Florida 33124

Contract No. N22-3-72(G)

Institute of Atmospheric Sciences
South Dakota School of Mines and Technology
Rapid City, South Dakota 57701

ATMOSPHERIC SCIENCES
LIBRARY
FEB 13 1973
N.O.A.A.
U. S. Dept. of Commerce

ABSTRACT

A numerical model of cloud growth over a mountain has been modified to simulate the formation and development of hurricane rainband clouds. The first and the third equations of motion, a thermodynamic energy equation, and water conservation equations for cloud substances, rain, and precipitating ice are solved numerically. The model is time-dependent, two-dimensional, covering a region 20 km square in the x- and z-directions with 200 m equal grid intervals. Initial conditions are taken from a mean hurricane atmospheric sounding. Water vapor and temperature perturbations are introduced in the lower levels. In addition, horizontal convergence is modeled in the lower kilometer and compensating divergence above a fixed level to simulate forced convection in the boundary layer. The formation of rain from cloud water follows ideas of Kessler and Berry. An equation due to Saunders is used to convert the cloud-liquid to cloud-ice isobarically at a predetermined temperature. The rainwater content is frozen, consistent with an equation due to Bigg, to form precipitating ice. A Marshall-Palmer distribution is hypothesized for the precipitating ice, utilizing the observations of Takeuchi. The growth of precipitating ice is calculated by the accretion of cloud-liquid, cloud-ice, and rain.

The effect of boundary layer horizontal convergence is tested on the simulated hurricane rainband clouds. The results show that the convergence has a marked influence on the cloud development.

Three experiments are conducted to test concepts of hurricane modification by "seeding" the rainband clouds. (Seeding is simulated by freezing the supercooled cloud water, instantaneously and isobarically.) The purpose of the seeding is to stimulate the rainband clouds so that the air converging to the hurricane eyewall is "short-circuited" by the rainbands and, in addition, so that more of the water vapor from the boundary layer is processed in the rainband clouds thus limiting the amount available for the eyewall clouds. Both of these processes would weaken the eyewall circulation. The three seeded cases simulate:

- (1) seeding of an isolated cloud element;
- (2) early seeding of all clouds so that their cloud liquid transforms to cloud ice as they rise past a prescribed temperature level in the atmosphere; and
- (3) later seeding of all clouds so that a considerable depth of supercooled cloud liquid is transformed instantaneously to cloud liquid.

The results show that clouds of moderate size are generated which become stimulated by the seeding. In the first seeded case the cloud elements interact with one another showing that the seeded cloud tends to dampen the growth of the unseeded cloud. In the second seeded case (early seeding) over 2 km of additional growth and slight additional precipitation occur. In the third case (late seeding) about 1 km of additional growth occurs (but no additional precipitation).

No "long lasting" hurricane rainband clouds have been simulated, which precludes calculations of the source of the water vapor in such clouds. The most vigorous convection results from a simulation which includes strong low-level inflow.

TABLE OF CONTENTS

	<u>Page</u>
ABSTRACT	iii
LIST OF FIGURES	vii
LIST OF TABLES	ix
1. INTRODUCTION	1
2. CLOUD MODEL	2
2.1 The Hydrodynamic Equations	2
2.2 Cloud Physics Equations	6
2.3 Thermodynamic Energy Equations	11
2.4 The Boundary Conditions	12
2.5 Initial Conditions	13
3. RESULTS	19
3.1 Effects of Boundary Layer Convergence	20
3.2 The Small Scale Seeding Experiment	25
3.3 The First Type of Seeding Experiment	34
3.4 The Second Type of Cloud Seeding	50
4. DISCUSSION	68
ACKNOWLEDGMENTS	71
REFERENCES	72
APPENDIX 1: Stream Function Formulation	74
APPENDIX 2: List of Symbols	76
APPENDIX 3: Personnel Effort and Special Reports	80

LIST OF FIGURES

<u>Number</u>	<u>Title</u>	<u>Page</u>
1	Cloud physics processes simulated in the model	7
2	Portions of the Skew-T log P chart showing the initial thermodynamic conditions	14
3	The superimposed radial wind velocity	15
4	Initial conditions for Case 1	17
5	The initial fields for Case 3	18
6	The initial fields for Case 2, a case without boundary layer horizontal convergence	21
7	Initial large scale vertical velocity and horizontal divergence distribution	22
8	Case 1 at 108 min	23
9	Case 2 at 108 min	24
10	Small scale seeding case, Case 1A, at 147 min	26
11	Case 1 at 153 min	27
12	Case 1A at 153 min	28
13	Case 1 at 156 min	29
14	Case 1A at 156 min	30
15	Case 1 at 159 min	31
16	Case 1A at 159 min	32
17	Time variations of seeded and unseeded cloud tops	33
18	Case 3 at 96 min	35
19	Case 3 at 102 min	36
20	Case 3A at 102 min	37
21	Case 3 at 108 min	38

LIST OF FIGURES (Continued)

<u>Number</u>	<u>Title</u>	<u>Page</u>
22	Case 3A at 108 min	39
23	Case 3 at 114 min	40
24	Case 3A at 114 min	41
25	Case 3 at 120 min	42
26	Case 3A at 120 min	43
27	Case 3 at 129 min	44
28	Case 3A at 129 min	45
29	Case 3 at 138 min	46
30	Case 3A at 138 min	47
31	Time variations of two cloud tops in Case 3 and Case 3A	48
32	Time variation of maximum updrafts for Case 3 and 3A	49
33	Time variation of kinetic energy for Case 3 and 3A	51
34	The vertical velocity field at 96. min in Case 3	52
35	Case 3 at 174 min	54
36	Case 3 at 180 min	55
37	Case 3B at 180 min	56
38	Case 3 at 186 min	57
39	Case 3B at 186 min	58
40	Case 3 at 189 min	59
41	Case 3B at 189 min	60
42	Case 3 at 192 min	61

LIST OF FIGURES (Continued)

<u>Number</u>	<u>Title</u>	<u>Page</u>
43	Case 3B at 192 min	62
44	Case 3 at 195 min	63
45	Case 3B at 195 min	64
46	Time variation of cloud tops in Case 3 and Case 3B	65
47	Time variation of maximum updrafts in Cases 3 and 3B	66
48	Time variation of kinetic energy in Cases 3 and 3B	67

LIST OF TABLES

<u>Number</u>	<u>Title</u>	<u>Page</u>
1	General Characteristics of the Cases	19

1. INTRODUCTION

Recent work with two and three-dimensional mesoscale numerical models of hurricanes (Rosenthal, 1971; Anthes, 1971) has indicated that the circulation in the hurricane eyewall might be sensitive to the manipulation by cloud seeding of the large convective cells found in hurricane rainbands. Two effects are postulated: 1) the increased convection in the rainband clouds results in additional growth to the main outflow region. Portions of the air flowing towards the eyewall clouds are diverted to this augmented convective area in the rainband cloud thus reducing the circulation of the hurricane due to angular momentum considerations; 2) the additional vapor needed to feed this convection is obtained at the expense of the eyewall clouds, further reducing the intensity of the eyewall circulation.

Rosenthal's study indicated a marked decrease in the wind speed about the eyewall given a $4^{\circ}\text{C hr}^{-1}$ increase in the heating rate at a radius typical for rainband clouds. The fuel for this augmented heat source was, presumably, the heat of fusion from the freezing of super-cooled cloud and rain particles or additional condensation or deposition caused by increased convection.

Anthes conducted a set of simulated rainband seeding experiments and identified the source of vapor to be either the middle troposphere or the lower boundary layer. The effects on the hurricane circulation were quite different, depending on the source region for the vapor. If the rainband clouds were fed from the middle troposphere, very little effect is noticed on the eyewall circulation. If the source is the surface boundary layer, then a 40 percent decrease is noticed in the eyewall circulation.

These results focus attention on the interaction of the large convective cells embedded in the rainbands and their reaction to stimulation by silver iodide seeding. Simpson *et al.* (1967) have pointed out that the tropical cumulus clouds which were seeded in a field experiment either grew explosively, experienced cutoff growth of the seeded tower, or failed to grow. The cutoff growth mode for rainband clouds would have very little effect on the hurricane circulation. Maximum effect would occur if the rainband clouds could be stimulated to grow to the main hurricane outflow region at 45,000 to 50,000 ft (13 to 15 km) with the cloud circulation extending from there to the surface boundary layer. The inflow to the eyewall would then be "short-circuited" and, in addition, the vapor available to the eyewall would be depleted.

The purpose of this study is to numerically simulate these rainband clouds and to perform seeding experiments on the computer-generated rainband clouds.

2. CLOUD MODEL

The two-dimensional rainband cloud model is adapted from the numerical work of Orville (1965), Liu and Orville (1969), and Wisner et al. (1972). A set of nonlinear, time-dependent, partial differential equations which includes the first and the third equations of motion, the thermodynamic energy equation, and various water substance conservation equations, is solved simultaneously on a computer. The domain of the model is 20 km in width and 20 km in height with equal grid interval of 200 m in the x- and z- directions. The domain of simulation is assumed to be along a radial 150-250 km from the eye. Several main changes have been made in the mountain cumuli model of Orville to simulate an average hurricane rainband situation. The equation of continuity is used assuming that the local variation of air density is zero. Fickian diffusion is changed to nonlinear eddy diffusion. Eddy coefficients of momentum and of heat, which depend on velocity, vorticity, deformation, and Richardson number, are used in all prognostic equations. Initial thermodynamic conditions appropriate to the hurricane atmosphere are utilized. Radial winds are superimposed on the model simulating the inflow toward the eye in the lower layers and outflow in the upper layers of the hurricane. Boundary layer horizontal convergence and compensating horizontal divergence in the upper layers are also simulated. The mountain and valley surface in the Orville model is omitted and replaced with an ocean surface. The periodic fluctuation in temperature and water vapor, which is the triggering mechanism in the mountain cumuli model, is substituted with random perturbations in temperature and water vapor in the boundary layer.

2.1 The Hydrodynamic Equations

The basic equations are the first and third equations of motion, the equation of state for an air and water vapor mixture, and the definition of potential temperature,

$$\frac{\partial}{\partial t} (\rho_0 u) = - \frac{\partial P}{\partial x} - \rho_0 u \frac{\partial u}{\partial x} - \rho_0 w \frac{\partial u}{\partial z} + F_x \quad (1)$$

$$\frac{\partial}{\partial t} (\rho_0 w) = - \frac{\partial P}{\partial z} - \rho_0 u \frac{\partial w}{\partial x} - \rho_0 w \frac{\partial w}{\partial z} - \rho_0 g - (\ell_c + \ell_R + \ell_I) \rho_0 g + F_z \quad (2)$$

$$P = \rho RT \left(\frac{1 + r/m}{1+r} \right) \quad (3)$$

$$\theta = T \left(\frac{P_0}{P} \right)^\kappa = T\pi^{-1} \quad (4)$$

where $\bar{\pi}$ is defined as

$$\bar{\pi} = \pi_0 - \frac{gZ}{C_p(\theta - \theta_0)} \ln \frac{\theta}{\theta_0}$$

Symbols are given in Appendix 2. With the domain of the model extending to 20 km in height, the air density in the upper parts of the model is one order of magnitude less than the air density in the lower parts. The equation of continuity for a non-divergent, incompressible fluid is not valid. Instead, the local change of air density is assumed to be zero, i.e.,

$$\frac{\partial \rho_0}{\partial t} = 0$$

which leads to the equation of continuity for a local compressible fluid,

$$\nabla \cdot \rho_0 V = 0 \quad (5)$$

where ρ_0 is the initial air density.

A vorticity equation is derived from (1), (2), and (5). Defining the vorticity as,

$$\eta = \frac{\partial \rho_0 w}{\partial x} - \frac{\partial \rho_0 u}{\partial z}$$

the vorticity equation then is,

$$\begin{aligned} \frac{\partial \eta}{\partial t} = & -V \cdot \nabla \eta - 2 \left(\eta + u \frac{\partial \rho_0}{\partial z} \right) \left(\frac{\partial u}{\partial x} + \frac{\partial w}{\partial x} \right) - uw \frac{\partial^2 \rho_0}{\partial z^2} \\ & + \rho_0 g \left(\frac{1}{\theta} \frac{\partial \theta'}{\partial x} + E \frac{\partial r}{\partial x} \right) (1 + \ell_c + \ell_I + \ell_R) \\ & - \rho_0 g \frac{\partial}{\partial x} (\ell_c + \ell_I + \ell_R) + F(K_m) \end{aligned} \quad (6)$$

after depleting terms of smaller magnitudes. The first term at the right is the advection term; the following two terms represent the effect of the local compressibility; the next term represents the effects of horizontal inhomogeneity in density; following is the drag

force exerted by the liquid and ice-phase water; and the last term is due to the effect of eddy diffusion. The stream function is defined as,

$$\nabla^2 \psi = \eta \quad (7)$$

with the velocities computed from

$$u = -\frac{1}{\rho_0} \frac{\partial \psi}{\partial z}, \quad w = \frac{1}{\rho_0} \frac{\partial \psi}{\partial x} \quad (8)$$

The last term in (6), $F(K_m)$, is expressed as,

$$F(K_m) = KMV^2\eta + 2 \frac{\partial K_m}{\partial z} \frac{\partial \eta}{\partial z} + 2 \frac{\partial \rho_0 u}{\partial x} \frac{\partial^2 K_m}{\partial x \partial z} + 2 \frac{\partial \rho_0 w}{\partial z} \frac{\partial^2 K_m}{\partial x \partial z} \\ + \frac{\partial \rho_0 w}{\partial x} \frac{\partial^2 K_m}{\partial x^2} - \frac{\partial \rho_0 u}{\partial z} \frac{\partial^2 K_m}{\partial z^2} + 2 \frac{\partial K_m}{\partial x} \frac{\partial \eta}{\partial x}$$

This results from introducing nonlinear eddy coefficients into the basic equations, (1) and (2). The values of the eddy coefficients, which depend on velocity, vorticity, deformation, and Richardson number, are calculated from the work of Drake (1969). The calculation for eddy coefficients of momentum is as follows:

$$K_m = \begin{cases} K_1 & , \quad \text{if } K < K_1 \\ K & , \quad \text{if } K_1 \leq K \leq K_2 \\ K_2 & , \quad \text{if } K > K_2 \end{cases}$$

where

$$K = \lambda^2 |\text{DEF}| (1 - Ri)^{0.75} \quad (9)$$

The squared deformation tensor $|\text{DEF}|^2$ is defined by

$$|\text{DEF}|^2 = \left(\frac{\partial u}{\partial x} - \frac{\partial w}{\partial z} \right)^2 + \left(\frac{\partial u}{\partial z} + \frac{\partial w}{\partial x} \right)^2 \quad (10)$$

and the Richardson number Ri is computed as

$$Ri = \frac{g \frac{\partial \theta}{\partial z}}{\theta |DEF|^2} \quad (11)$$

The mixing length λ is calculated by

$$\lambda^2 = 0.16 \frac{\eta^2 + |\rho_0 \mathbf{v} \cdot \nabla^2 \rho_0 \mathbf{v}|}{|\nabla \eta|^2 + |\eta \nabla^2 \eta|} \quad (12)$$

For the eddy coefficient of heat, which is used for the diffusion of thermal quantities, the calculation is carried out as:

$$K_h = \begin{cases} K_m f(Ri) & , \quad \text{if } K \geq K_m \\ K_m & , \quad \text{if } K < K_m \end{cases} \quad (13)$$

where Ri is the Richardson number used previously. Then the eddy coefficient of heat is determined by supplying the value of $f(Ri)$ as

$$f(Ri) = \begin{cases} f(K_3) & , \quad \text{if } Ri < K_3 \\ \frac{3 - 3Ri + (Ri)^2}{1 + (1-Ri)} & , \quad \text{if } K_3 \leq Ri \leq 1 \\ f(1) & , \quad \text{if } Ri > 1 \end{cases}$$

K_1 , K_2 , and K_3 are assigned $8 \text{ m}^2\text{sec}^{-1}$, $800 \text{ m}^2\text{sec}^{-1}$, and -100 to assure stable integrations. After the coefficients are calculated for all grid points, a smoothing over nine nearby points is carried out according to the matrix expression

$$\begin{pmatrix} \frac{1}{4} \\ \frac{1}{2} \\ \frac{1}{4} \end{pmatrix} \left(\frac{1}{4} \quad \frac{1}{2} \quad \frac{1}{4} \right)$$

More reality and more calculation are brought into the model by using the nonlinear eddy coefficients. No downward diffusion of the upper stable layer is present as is present in the earlier results of the mountain cumuli model (Orville and Sloan, 1970).

The kinetic energy per unit volume in the model is defined as

$$KE = \sum_i \frac{1}{2} (\rho_0 u_i^2 + \rho_0 w_i^2) \Delta x \Delta z$$

where the summation is over the entire domain.

2.2 Cloud Physics Equations

The cloud physics processes are governed by the equations in the one-dimensional cloud model of Wisner *et al.* (1972) and the parameterized technique of Liu and Orville (1969) and Kessler (1969). Five classifications of water substance are considered: water vapor, cloud water, cloud ice, rain, and precipitating ice. The cloud water and the cloud ice particles are assumed to be small enough that their terminal velocities can be neglected compared with the velocity of the air. The rain and the precipitating ice consist of liquid drops and ice particles with appreciable terminal velocities. The interaction of these water substances is demonstrated in Fig. 1.

A Marshall-Palmer distribution is hypothesized for the precipitable water substances; that is, the rain and the precipitating ice. Their terminal velocities are then computed as the mass-weighted mean velocities (Srivastava, 1967):

$$v_t = \frac{a \Gamma(4+b)}{6 \lambda_R^b} \quad U_t = \frac{\Gamma(4.5)}{6 \lambda_I^{0.5}} \left(\frac{4g\rho_I}{3 C_D \rho} \right)^{0.5} \quad (14)$$

where the constants a and b are 2115 cm sec^{-1} and 0.8 respectively (Liu and Orville, 1969), Γ is the gamma function, and λ_R and λ_I are defined as:

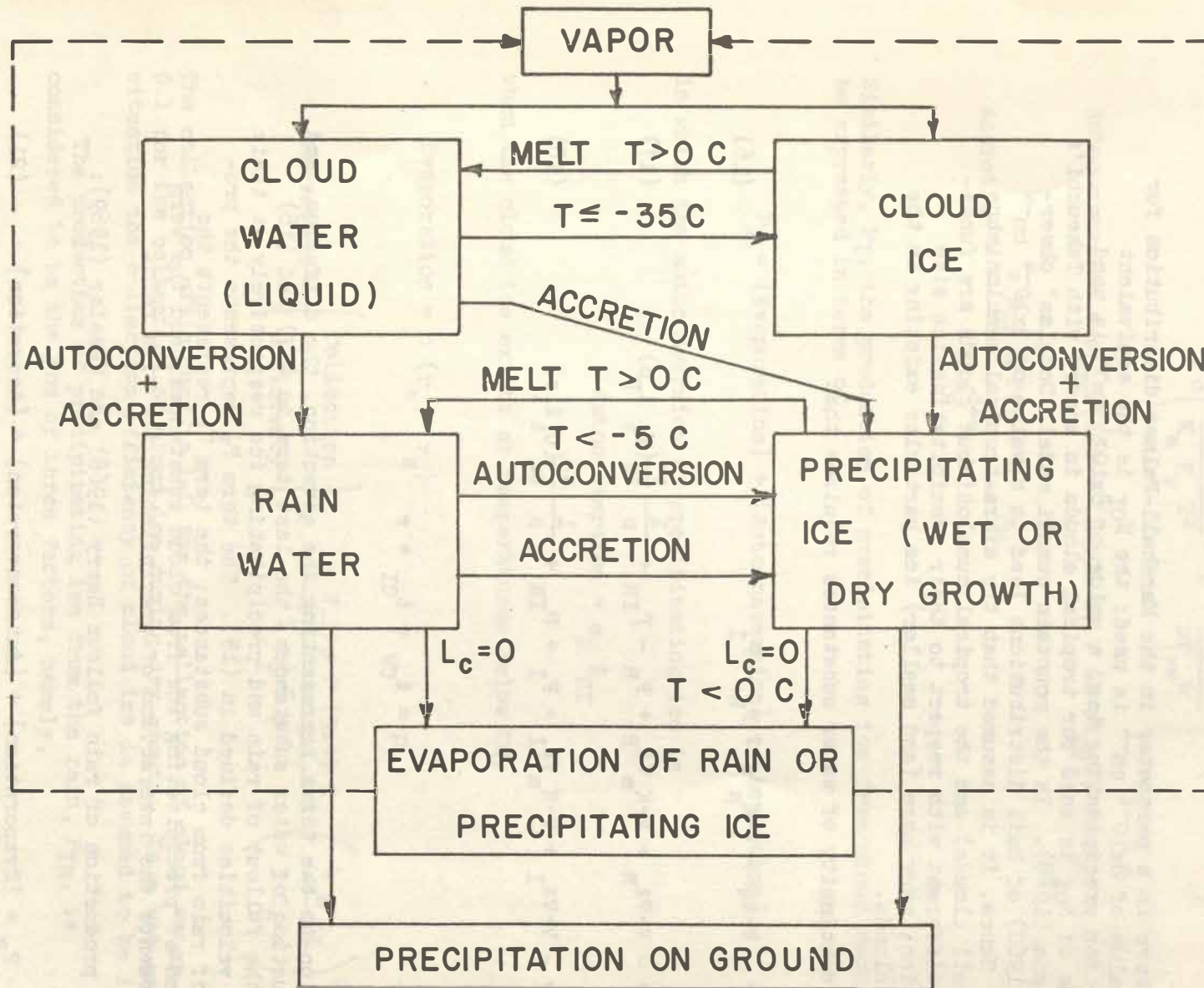


Fig. 1. Cloud physics processes simulated in the model.

$$\lambda_R = \left(\frac{\pi \rho_w N_{OR}}{\rho \ell_R} \right)^{0.25} \quad \lambda_I = \left(\frac{\pi \rho_I N_{OI}}{\rho \ell_I} \right)^{0.25} \quad (15)$$

The N_{OR} above is a parameter in the Marshall-Palmer distribution for rain, a value of $8 \times 10^{-2} \text{ cm}^{-4}$ is used; the N_{OI} is the equivalent parameter for precipitating ice, a value of $8 \times 10^{-1} \text{ cm}^{-4}$ is used. This value of N_{OI} is used for tropical clouds in accord with Takeuchi's observations (1968). In the mountain cumuli model, Douglas' observations (1960) of hail distributions lead to a value of $3 \times 10^{-4} \text{ cm}^{-4}$ for N_{OI} . Hence, it is assumed that the extra-tropical cumulonimbus clouds (hail clouds) and the tropical cumulonimbus clouds are fundamentally different with respect to their precipitating-ice size distribution, many more (and smaller) ice particles existing in the tropical clouds.

The continuity of water substances requires that

$$\frac{\partial q}{\partial t} = -V \cdot \nabla q + \nabla \cdot K_h \nabla q - P_R - P_I \quad (16)$$

$$\frac{\partial \ell_R}{\partial t} = -V \cdot \nabla \ell_R + \nabla \cdot K_m \nabla \ell_R + P_R - P_{IR} + \frac{1}{\rho} \frac{\partial}{\partial z} (v_t \ell_R \rho) \quad (17)$$

$$\frac{\partial \ell_I}{\partial t} = -V \cdot \nabla \ell_I + \nabla \cdot K_m \nabla \ell_I + P_I + P_{IR} + \frac{1}{\rho} \frac{\partial}{\partial z} (u_t \ell_I \rho) \quad (18)$$

where

$$q = \ell_{CW} + \ell_{CI} + r$$

In addition to the terms representing the advection, the diffusion, and the production of water substances, the last term in (17) and (18) denotes the fallout of rain and precipitating ice respectively at their terminal velocities defined in (15). The term P_R represents the production of rain from cloud substances; the term P_I represents the production of precipitating ice from cloud substances, and the term P_{IR} represents the interaction of precipitating ice with rain.

The production of rain follows Berry (1968) and Kessler (1969):

$$P_R = [\text{Evaporation}] + [\text{Autoconversion}] + [\text{Accretion}] \quad (21)$$

The terms at the right are computed from the following equations,

$$\text{Evaporation} = \frac{2\pi(S-1) N_{OR} [\Lambda^{-2} + 0.22\Gamma(\frac{b+5}{2}) a^{0.5} v^{-0.5} \Lambda^{-\frac{b+5}{2}}]}{\rho \left(\frac{L_v^2}{K_a R_v T^2} + \frac{1}{\rho r_{sw} \psi} \right)}$$

$$\text{Autoconversion} = \rho \ell_{CW}^2 / [120 + (1.596 N_1 / (D \cdot \rho \ell_{CW}))] \text{ if } \ell_{CW} > 1 \text{ g/kg}$$

$$\text{Accretion} = \frac{\pi N_{OR} a \Gamma(3+b) \ell_{CW}}{4 \lambda_R^{3+b}}$$

Similarly, P_I , the production of precipitating ice from cloud water can be expressed in terms of

$$P_I = [\text{Evaporation}] + [\text{Autoconversion}] + [\text{Accretion}]$$

in which the autoconversion of precipitating ice is

$$\text{Autoconversion} = \alpha_I \ell_{CI}$$

when the cloud ice exists at temperatures below 0C.

$$\text{Evaporation} = \beta (r_e - r_s)$$

$$\text{Accretion} = \left(\begin{array}{c} \text{Collection} \\ \text{Efficiency} \end{array} \right) \times \frac{\pi N_{OI} \rho \Gamma(3.5) \ell_c}{4 \lambda_I^{3.5} \rho} \left(\frac{4 g \rho_I}{3 C_D \rho} \right)^{0.5}$$

The collection efficiency is 1.0 for the collection of cloud water and 0.1 for the collection of cloud ice during dry growth. In a wet growth situation the collection efficiency of cloud ice is assumed to be 1.0.

The production of precipitating ice from the rain, P_{IR} , is considered to be the sum of three factors, namely,

$$P_{IR} = [\text{Freezing}] + [\text{Accretion}] + [\text{Melting}]$$

The freezing of rain is calculated from an equation due to Bigg (1953):

$$\text{Freezing} = 20 \pi^2 B' N_{OR} \rho_w [\exp \{A' (-T_c)\} - 1] \lambda_R^{-7}$$

The accretion term includes either dry growth or wet growth (the smaller of the two is used):

$$\text{Dry Growth} = \pi^2 \frac{\rho_w}{\rho} E_w N_{OR} N_{OI} |U_t - V| \left[\frac{5}{\lambda_R^6 \lambda_I} + \frac{2}{\lambda_R^5 \lambda_I^2} + \frac{0.5}{\lambda_R^4 \lambda_I^3} \right]$$

$$\text{Wet Growth} = \frac{2 N_{OI} A_1 [\rho L_f D_f \Delta r_s - K_a T_c]}{\rho (L_f + C_w T_c) \lambda_I^2}$$

$$+ \frac{\pi N_{OI} \rho \ell_{CI} \Gamma(3.5)}{4 \lambda_I^{3.5}} \left(\frac{4 g \rho_I}{3 C_D \rho} \right)^{0.5} \left(1 - \frac{C_I T_c}{L_f + C_w T_c} \right)$$

Wet growth provides a special situation for the production terms P_{IR} and P_I since portions of these production processes are due to the accretion of cloud liquid and cloud ice and part is due to the accretion of rain. Since the amount of accreted cloud ice is known the remainder of the wet growth mass must be due to the collection of cloud liquid and rain. Portions of this mass are assigned to the rain and cloud liquid consistent with their fraction of the total liquid mass. Hence if rainwater constitutes 75 percent of the total liquid mass then 75 percent of the remainder of the wet growth mass is considered to be accreted rain. The melting of precipitating ice is

$$\text{Melting} = - \frac{2\pi}{\rho L_f} [K_a T_c + L_f \psi \rho \Delta r_s] N_{OI}$$

$$\left(1.6 \lambda_I^{-2} + 0.3 \Gamma(2.75) \lambda_I^{-2.75} v^{-0.5} \left(\frac{4 g \rho_I}{3 C_D \rho} \right)^{0.25} \right)$$

$$- \frac{C_w}{L_f} T_c \left[\ell_{CW} N_{OI} \frac{\pi}{4} \Gamma(3.5) \lambda_I^{-3.5} \left(\frac{4 g \rho_I}{3 C_D \rho} \right)^{0.5} \right]$$

$$+ \text{Dry Growth} \Bigg)$$

2.3 Thermodynamic Energy Equations.

The thermodynamic energy equation follows Orville (1965) and Wisner (1970) with several added heat sources:

$$\begin{aligned}
 \frac{\partial \phi'}{\partial t} = & -\mathbf{v} \cdot \nabla \phi' + \nabla \cdot \mathbf{K}_h \nabla \phi' \\
 & + \frac{L_f}{C_p T_{oo}} (P_I + P_{IR}) + \frac{C_w T_c}{C_p T_{oo}} (P_{IR}) \Big|_{T_c > 0C} \\
 & - \frac{\partial T}{\partial z} \left[\frac{(C_w \text{ or } C_I)}{C_p T_{oo}} \ell_c w + (w - v_t) \ell_R \frac{C_w}{C_p T_{oo}} + (W - U_t) \frac{\ell_I C_I}{C_p T_{oo}} \Big|_{T_c < 0C} \right] \\
 & - \frac{\partial T}{\partial x} \left[u \left(\frac{C_w \text{ or } C_I}{C_p T_{oo}} \ell_c + \ell_R \frac{C_w}{C_p T_{oo}} + \ell_I \frac{C_I}{C_p T_{oo}} \Big|_{T_c < 0C} \right) \right] \\
 & + \frac{L}{C_p T_{oo}} P_R \Big|_{\ell_c = 0} + \frac{L_S}{C_p T_{oo}} P_I \Big|_{\ell_c = 0} \tag{25}
 \end{aligned}$$

with

$$\phi' = \frac{\theta'}{\theta} + \frac{Lr}{C_p T_{oo}} \text{ (Unsaturated)} \tag{26a}$$

$$\phi' = \frac{\theta'}{\theta} + \frac{Lr_s}{C_p T_{oo}} \text{ (Saturated)} \tag{26b}$$

The P_I in the latent heat of fusion term in (25) excludes the accretion of cloud ice by precipitating ice. The saturation mixing ratio, r_s , is given by

$$r_s = \frac{\epsilon e_s}{P - e_s} \tag{27}$$

The equilibrium vapor pressure over water or over ice, e_s , is approximated by the empirical formula suggested by Wisner (1970):

$$e_{sw} = \exp \left(\frac{19.079T - 4782.9}{T - 35.9} \right) \tag{28}$$

$$e_{si} = 6.02 \exp \left(22.5309 - \frac{6154.55}{T} \right) \tag{29}$$

Ogura's (1963) technique to decide saturation is then modified to solve (27), (28), and (29) with the thermodynamic energy equation (25) by the Newton-Raphson method. This modification has proven to be more satisfactory, since (28) and (29) give good approximation to equilibrium vapor pressures and the Newton-Raphson method converges within a few iterations. Saunder's (1957) equation is used to give the heating due to isobaric freezing of cloud water into cloud ice instantaneously

$$\Delta T = \frac{\Delta \ell \frac{L_f}{c} + (e_{sw} - e_{si}) \frac{\epsilon L_s}{P}}{C_p + r C'_p + \frac{\epsilon L_s^2 e_{si}}{R_v T^2}} \quad (30)$$

The heating is then added to the entropy by

$$\theta'_I = T \bar{\pi}^{-1}$$

and

$$\phi' = \frac{\theta'_I}{\theta} + \frac{L_s r_{si}}{C_p T_{\infty}} \quad (31)$$

This freezing of cloud water happens at -35°C in all natural cases and at -5°C or -10°C in the seeded cases.

2.4 The Boundary Conditions

The lower boundary of the model is assumed to be 10 m above the ocean surface. The water vapor from the ocean surface is diffused into the lowest grid points via the aerodynamic method (Lavoie, 1968),

$$\frac{\partial r}{\partial t} = C_D |V| \frac{\partial r}{\partial h} \quad (32)$$

where $|V|$ is horizontal wind speed and the gradient is normal to the ocean surface. No sensible heat is transferred at the ocean surface; the temperature remains constant there. A value of 3×10^{-3} is used for C_D . The average vapor flux from the ocean surface into the model is approximately $3 \times 10^{-5} \text{ g kg}^{-1} \text{ sec}^{-1}$.

The vorticity is constant and the stream function vanishes at the lower boundary. The stream function and vorticity are kept constant at the upper and side boundaries. Tangential winds are allowed at all boundaries while normal winds vanish at the upper and lower boundaries, i.e.,

$\psi = 0$	at $z = 0$
$\psi = \text{constant}$	at $z = 20 \text{ km}$ and $x = 0, 20 \text{ km}$
$\eta = \text{constant}$	at $z = 0, 20 \text{ km}$ and $x = 0, 20 \text{ km}$
$w = 0$	at $z = 0, 20 \text{ km}$

The non-vanishing velocities are calculated by non-centered differences from the stream function by (8).

2.5 Initial Conditions

The initial thermodynamic conditions appropriate to a hurricane atmosphere are based on the statistics of Sheets (1969). Figure 2 shows the initial thermodynamic conditions used in the model.

Radial winds are superimposed on the model with inflow toward the eye in the lower layers and outflow in the upper layers. In some earlier cases, the maximum inflow was -5 m sec^{-1} near the surface, decreasing linearly with height, changing to outflow above 8.5 km and reaching the maximum outflow of 5 m sec^{-1} above 17 km , the tropopause. However, this radial wind profile was found to be inappropriate in that it provided an insufficient supply of water vapor to form a sizable tropical storm. In the later cases of this report the radial wind profile is changed so that the inflow at the ocean surface is -5 m sec^{-1} , increasing sinusoidally to -10 m sec^{-1} at 0.5 km , and then decreasing linearly and vanishing at 2 km . The outflow starts at 10 km , increasing linearly to 10 m sec at and above the tropopause. This radial wind profile with a strong jet at low altitudes is used in the hope that it might initiate a long-lasting cloud (Takeda, 1971). Figure 3 shows these two different wind profiles.

Boundary layer horizontal convergence with a magnitude of $5 \times 10^{-5} \text{ kg m}^{-3} \text{ sec}^{-1}$ is simulated, which gives 5 cm sec^{-1} updraft at 1 km , the top of the boundary layer. Compensating horizontal divergence is also simulated in the upper layers starting at 5 km which reduces the large scale vertical motion to zero at the tropopause and which provides no net mass convergence into the model throughout the integration. The mathematical technique generating the initial stream function is given in Appendix 1.

This initial slow upward flow causes a general cooling with a maximum rate of 0.3C hr^{-1} in the model. This cooling would result in a contraction of the atmosphere and an increase of mass within the domain of integration which, however, is not taken into account.

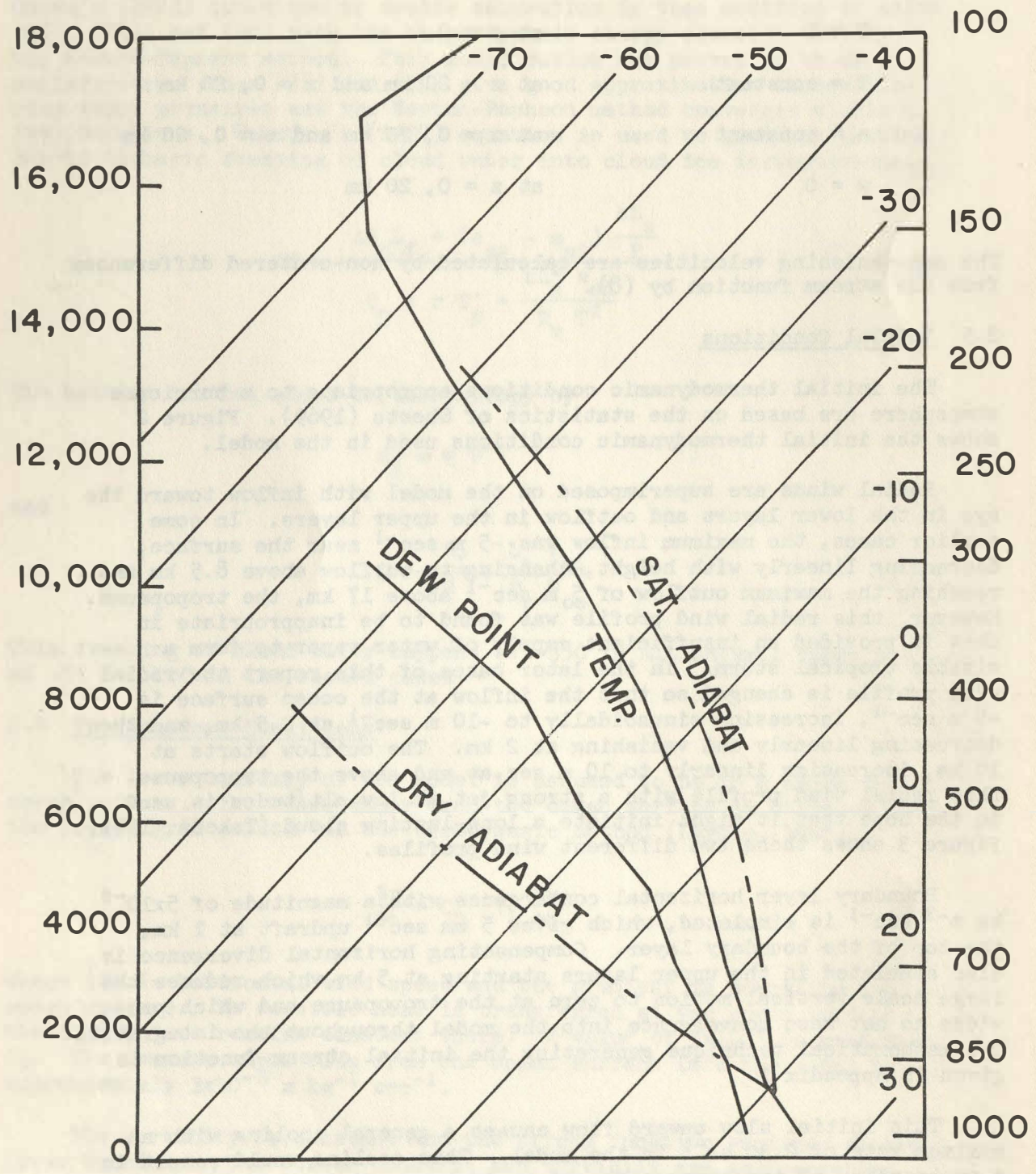


Fig. 2. Portions of the Skew-T log P chart showing the initial thermodynamic conditions.

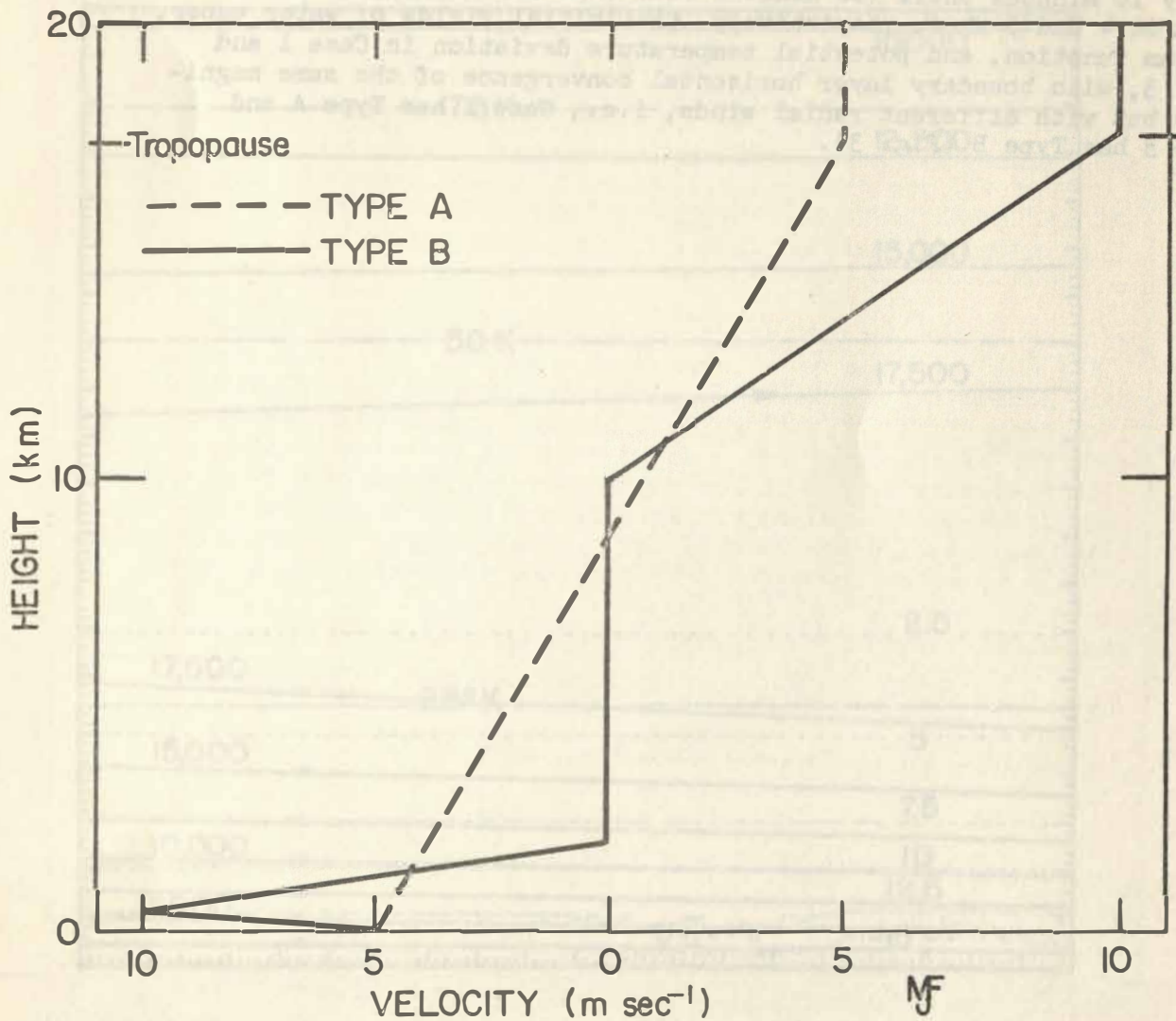


Fig. 3. The superimposed radial wind velocity. Solid line for Case 3, dash line for Cases 1 and 2.

The clouds are triggered by random perturbations in temperature and water vapor in the right half of the boundary layer. In Cases 1 and 2 random perturbations with possible maximum amplitudes of 2C and 2.5 g kg^{-1} respectively are applied every 20 minutes over a depth of 600 m starting at 600 m above the surface. In Case 3 these random perturbations are applied at random times with an average of once every 10 minutes until 100 minutes real time and then are turned off. Figures 4 and 5 show, respectively, the initial fields of water vapor, stream function, and potential temperature deviation in Case 1 and Case 3, with boundary layer horizontal convergence of the same magnitude but with different radial winds, i.e., Case 1 has Type A and Case 3 has Type B (Fig. 3).

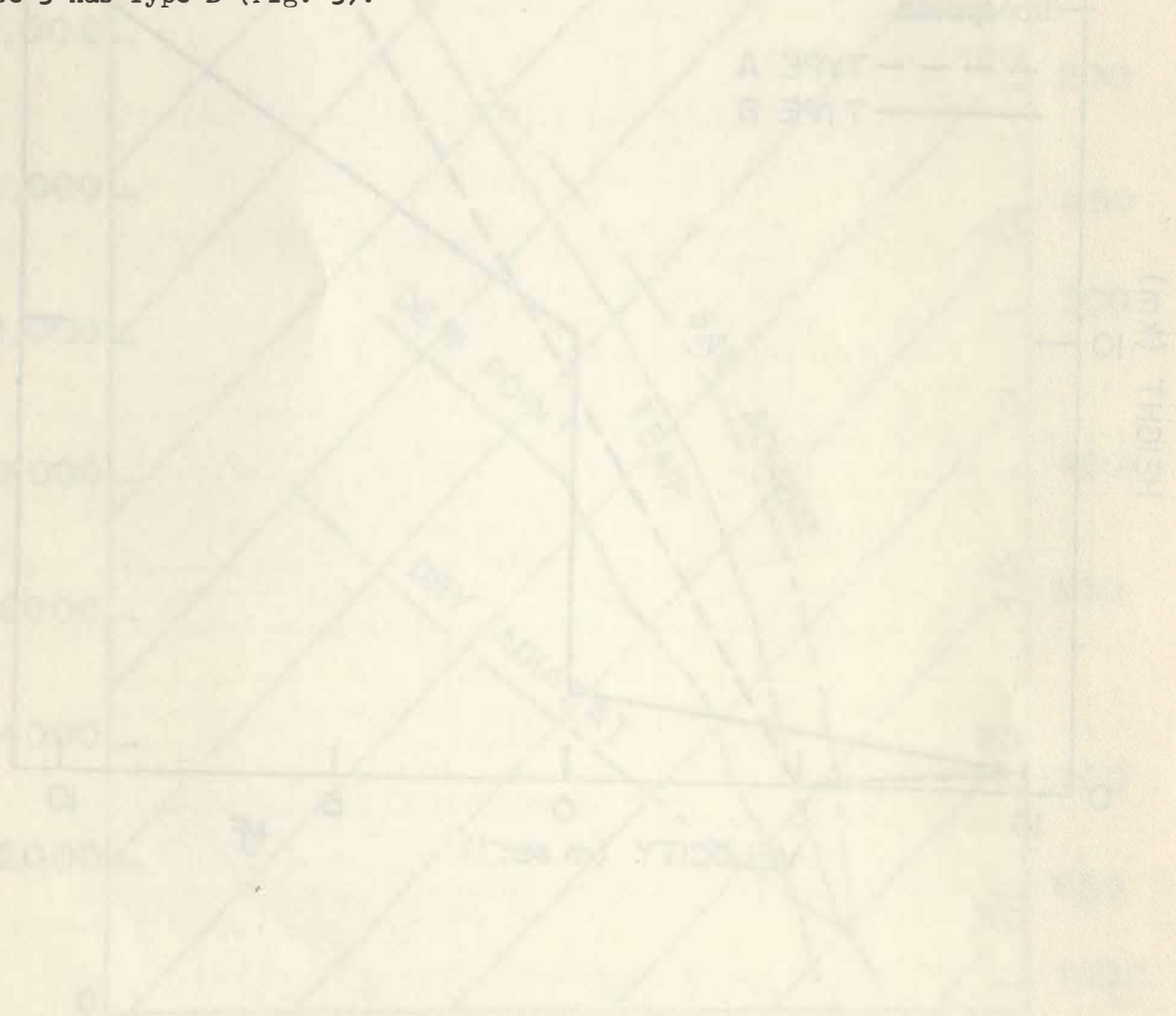


Fig. 3. The upper atmosphere initial field velocity. Case 1 has Type A and Case 3 has Type B (Fig. 3).

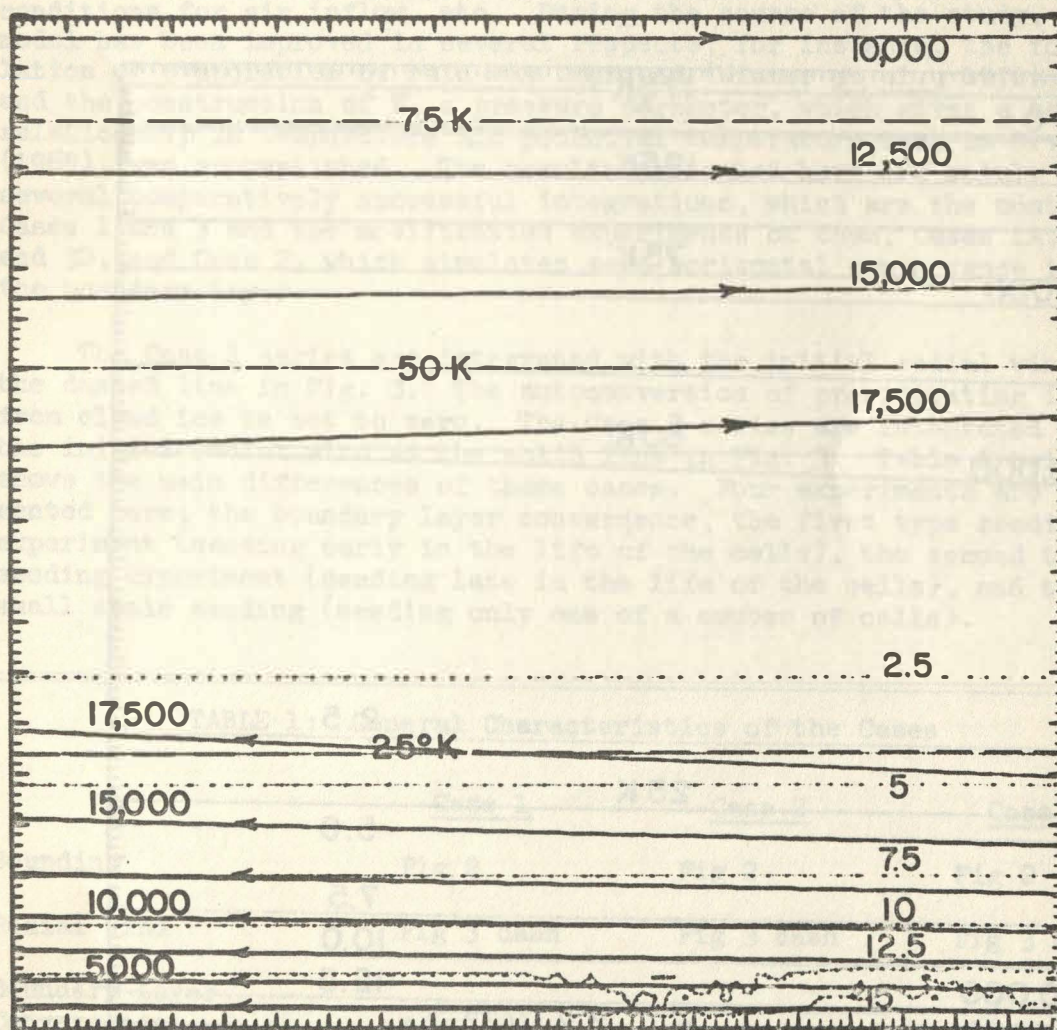


Fig. 4. The initial stream function (dark lines, $\text{kg m}^{-1} \text{sec}^{-1}$), potential temperature deviation (dash lines, K), and water vapor (dot lines, g kg^{-1}) fields of Case 1. Water vapor perturbation is shown at lower right half of boundary layer, the distance between major tick marks in 1 km.

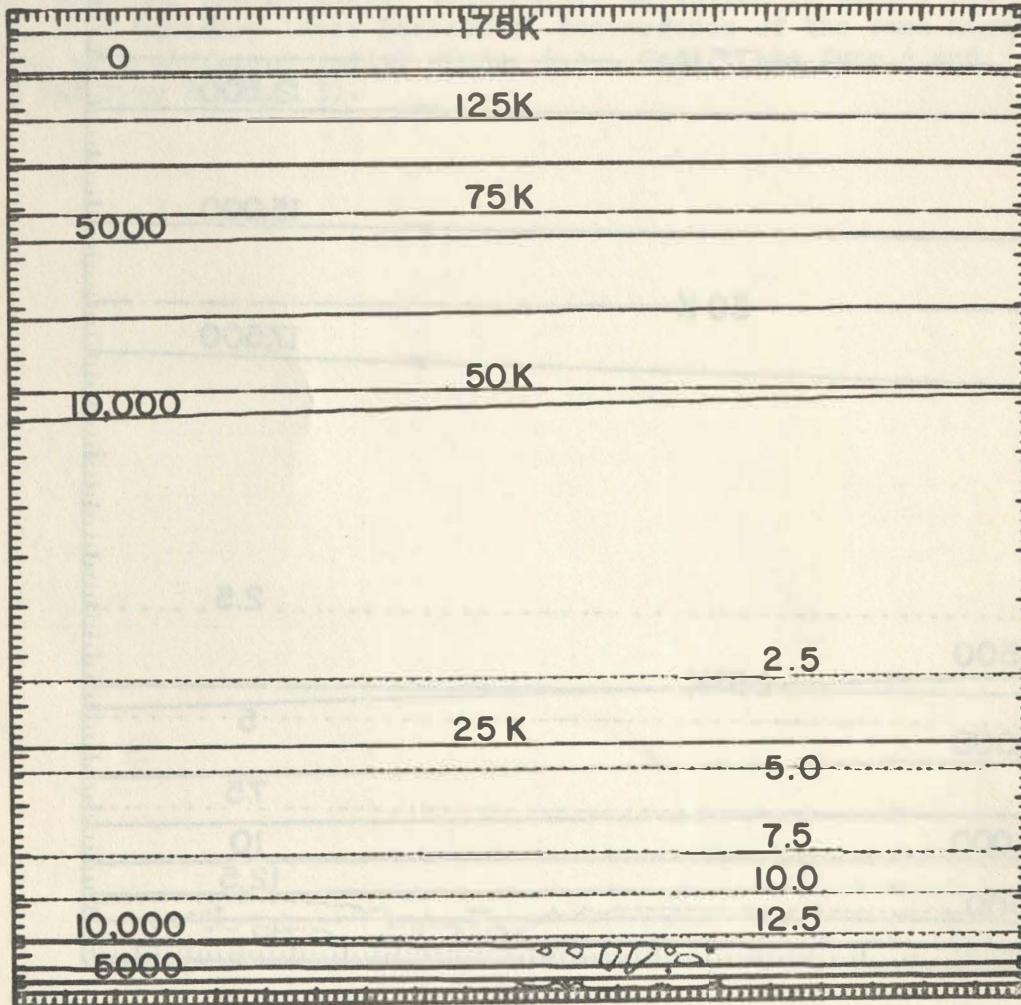


Fig. 5. The initial fields for Case 3.

3. RESULTS

Thirteen attempts have been made to initiate the rainband clouds. Efforts have been expended seeking appropriate initial radial wind profile, suitable limits for eddy coefficients, reasonable boundary conditions for air inflow, etc. During the course of the study, the model has been improved in several respects; for instance, the formulation of evaporation of rain was improved (Wisner *et al.*, 1972), and the construction of $\bar{\pi}$, a pressure parameter, which gives a better relationship in temperature and potential temperature than in Orville (1965), was accomplished. The results presented here are mainly from several comparatively successful integrations, which are the control Cases 1 and 3 and the modification experiments on them, Cases 1A, 3A, and 3B, and Case 2, which simulates zero horizontal convergence in the boundary layer.

The Case 1 series are integrated with the initial radial wind as the dashed line in Fig. 3. The autoconversion of precipitating ice from cloud ice is set to zero. The Case 3 series are integrated with the initial radial wind as the solid line in Fig. 3. Table 1 below shows the main differences of these cases. Four experiments are presented here; the boundary layer convergence, the first type seeding experiment (seeding early in the life of the cells), the second type seeding experiment (seeding late in the life of the cells), and the small scale seeding (seeding only one of a number of cells).

TABLE 1: General Characteristics of the Cases

	<u>Case 1</u>	<u>Case 2</u>	<u>Case 3</u>
Sounding	Fig 2	Fig 2	Fig 2
Radial Wind	Fig 3 dash	Fig 3 dash	Fig 3 solid
Boundary Layer Convergence	Yes	No	Yes
Autoconversion to Precipitating Ice	No	No	Yes
Freezing Level in Seeded Case	-10 C	-10 C	-5 C
Time to Supply Perturbations	Every 20 min	Every 20 min	Randomly - average 10 min

3.1 Effects of Boundary Layer Convergence

The influence of the boundary layer horizontal convergence on the development of the rainband clouds is investigated. The importance of this large scale convergence should not be underestimated since some consider that the large clouds in the tropics, if not all large cloud developments in the tropics, require some large scale convergence to initiate the cloud growth. This is because a rather uniform surface exists under the clouds so that inhomogeneities in the lower surface cannot be counted on to supply the initial perturbation for cloud growth as in continental regions, except in the area of islands. Case 1 is integrated with superimposed boundary layer horizontal convergence as described in the Sec. 2.5, while Case 2 is integrated with the same initial thermodynamic conditions, boundary conditions and governing equations except that no boundary layer horizontal convergence is superimposed. The initial radial wind profile is the Type A (Fig. 3) in both cases. There is no general upward motion in this latter case. Figure 6 shows the initial fields of stream function, water vapor and potential temperature deviation of Case 2. The same fields for Case 1 are shown in Fig. 3. Figure 7 shows the initial large scale upward motion and the distribution of horizontal divergence for Case 1.

In both cases, rainband clouds are initiated by perturbations after a few time steps, but no convective cloud associated with appreciable updrafts appears until after 50 min.

In Case 1, cloud tops ascend at 100 m min^{-1} after 50 min to attain a height of 8 km at 108 min. Figure 8 illustrates the cloud outlines and the rain and precipitating ice distributions at 108 min. The clouds at the 7 km level beside the main cell are caused by the general upward motion initiated by the boundary layer convergence. The clouds evident below 3 km are produced by successive perturbations and are possible embryos of larger cells.

Figure 9 demonstrates the same situation for Case 2 as Fig. 8 for Case 1. Small, inactive cells exist. The convective cells found at the right have grown to 2.5 km which is 5.5 km lower than the main cell in Case 1 at the same time. The maximum updraft in Case 1 reaches 8 m sec^{-1} , while in Case 2 is only 3 m sec^{-1} . Active cloud growths in Case 1 have diameters of at least 2 km whereas the clouds in Case 2 are normally about 1 km in width. Hence, the simulated boundary layer convergence leads to broader, more active cloud cells.

The physical reason for this more active convection seems obvious. The superimposed upward motion in the boundary layer causes cooling and moistening of the atmosphere. The cooling rate is small, 0.3 C hr^{-1} , which is much less than the heating rate due to phase change. The large scale upward flow creates an average moistening rate of $1.8 \times 10^{-4} \text{ gm kg}^{-1} \text{ sec}^{-1}$ which in 100 minutes would advect an additional 1 gm kg^{-1} of water vapor to the 1 km level. The random numbers generated are

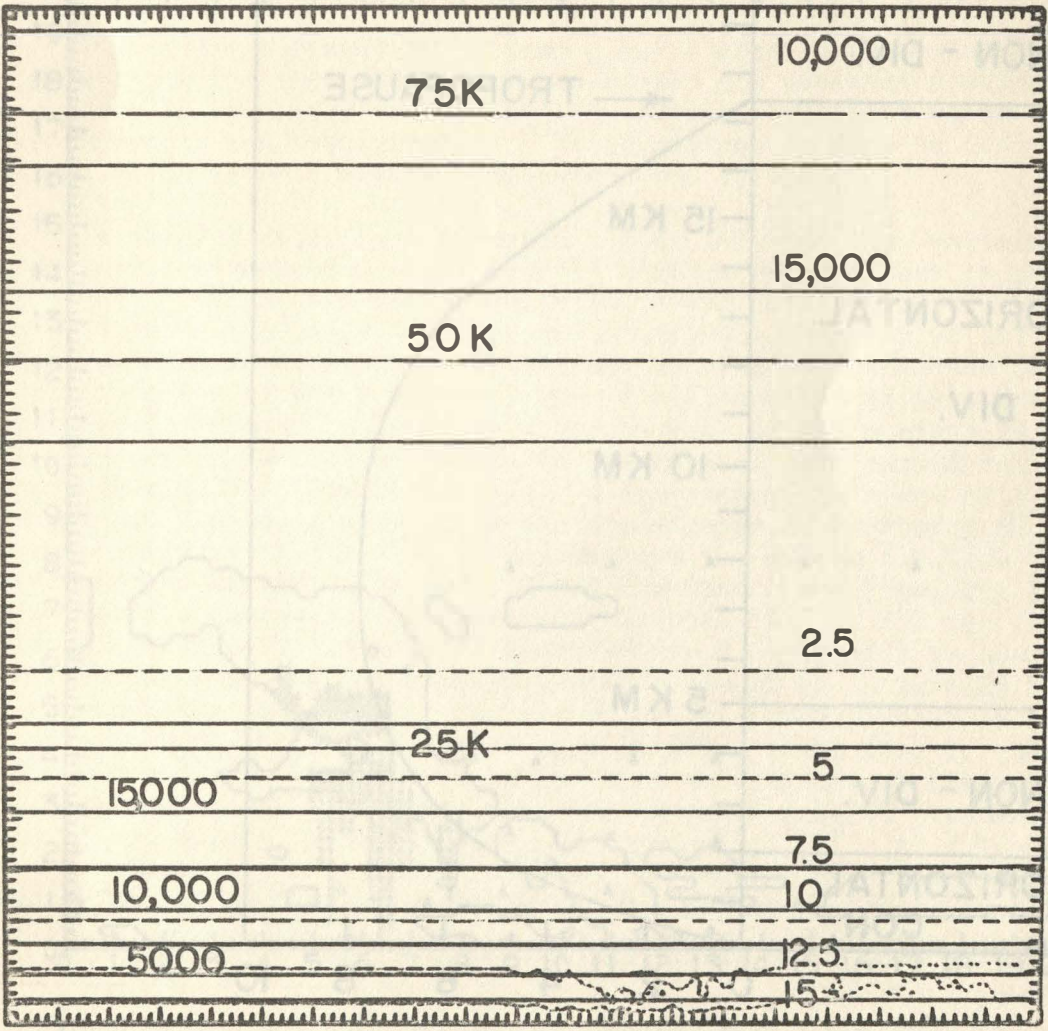


Fig. 6. The initial fields for Case 2, a case without boundary layer horizontal convergence.

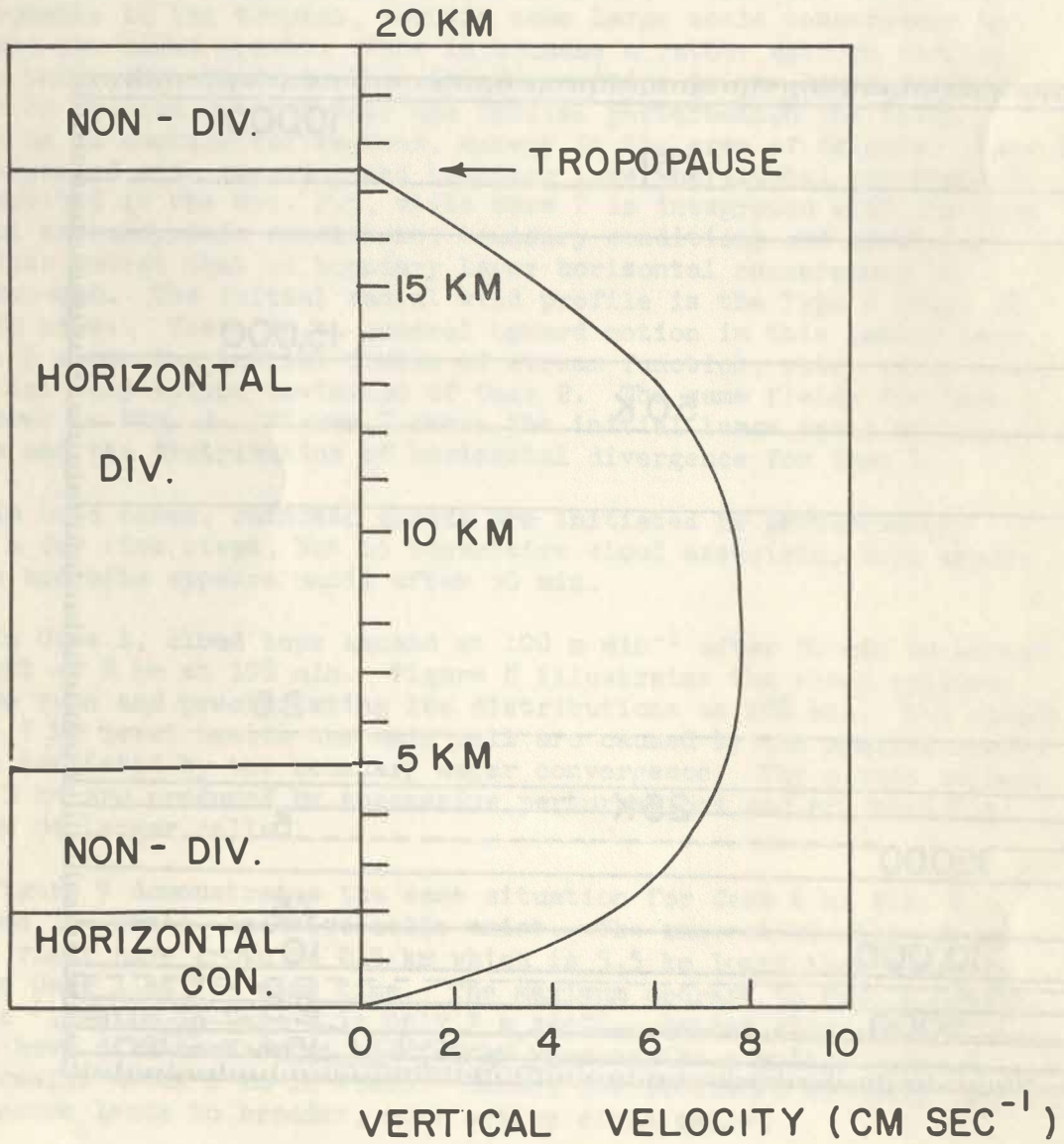


Fig. 7. Initial large scale vertical velocity and horizontal divergence distribution in Cases 1 and 3.

exactly the same for the two cases but will operate on slightly different fields (10% greater water content in regions of strongest upward motion in Case 1). Thus the clouds are formed by slightly different hydrothermal perturbations but still, we think, owe the major part of their additional growth to the modified stability of the environment.

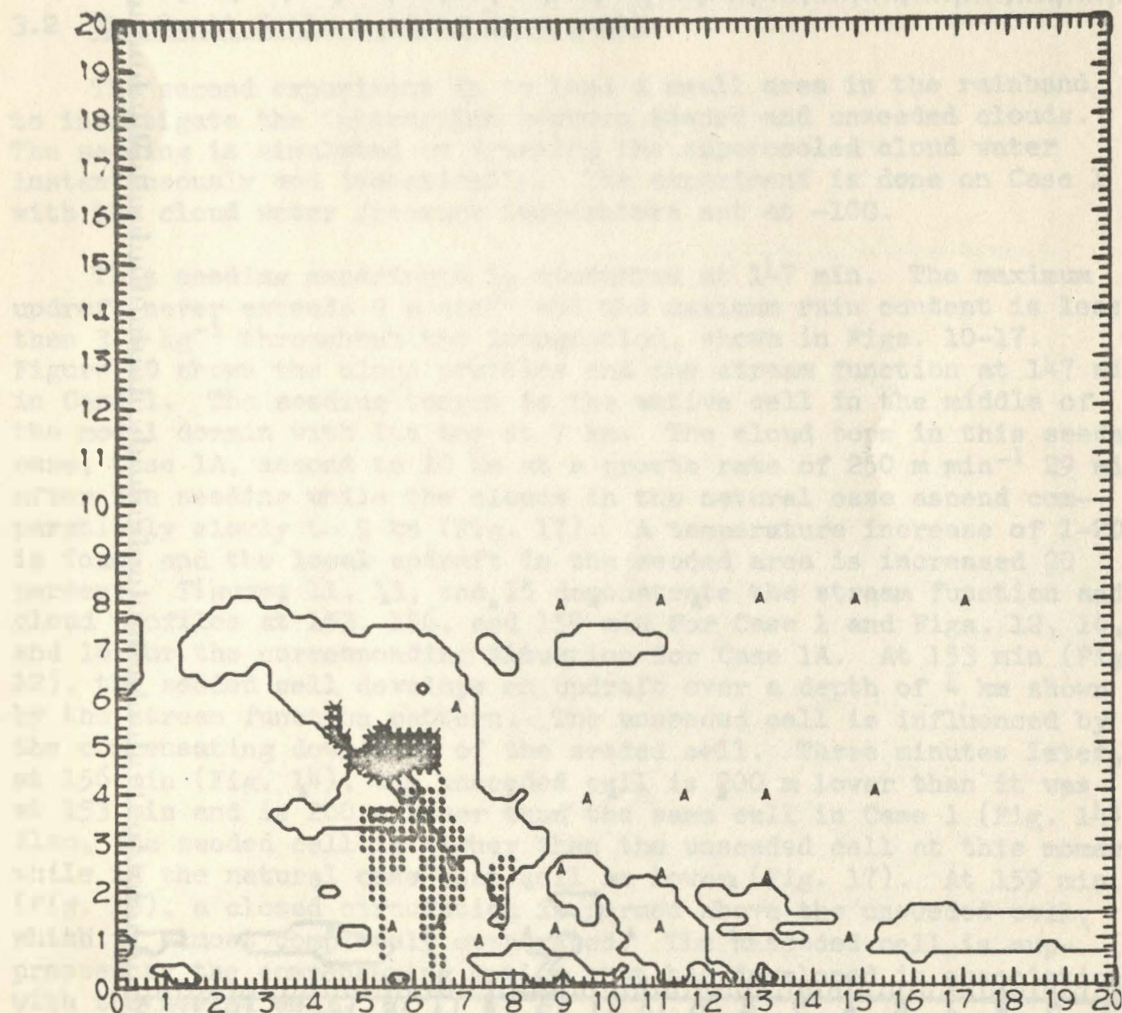


Fig. 8. Cloud outlines (defined as 100% humidity) and precipitation at 108 min for Case 1 with horizontal convergence in lower 1 km and divergence from 5 to 17.5 km. A dot \cdot denotes rain with water content over 1 g kg^{-1} . A star $*$ denotes graupel with water content over 1 g kg^{-1} .

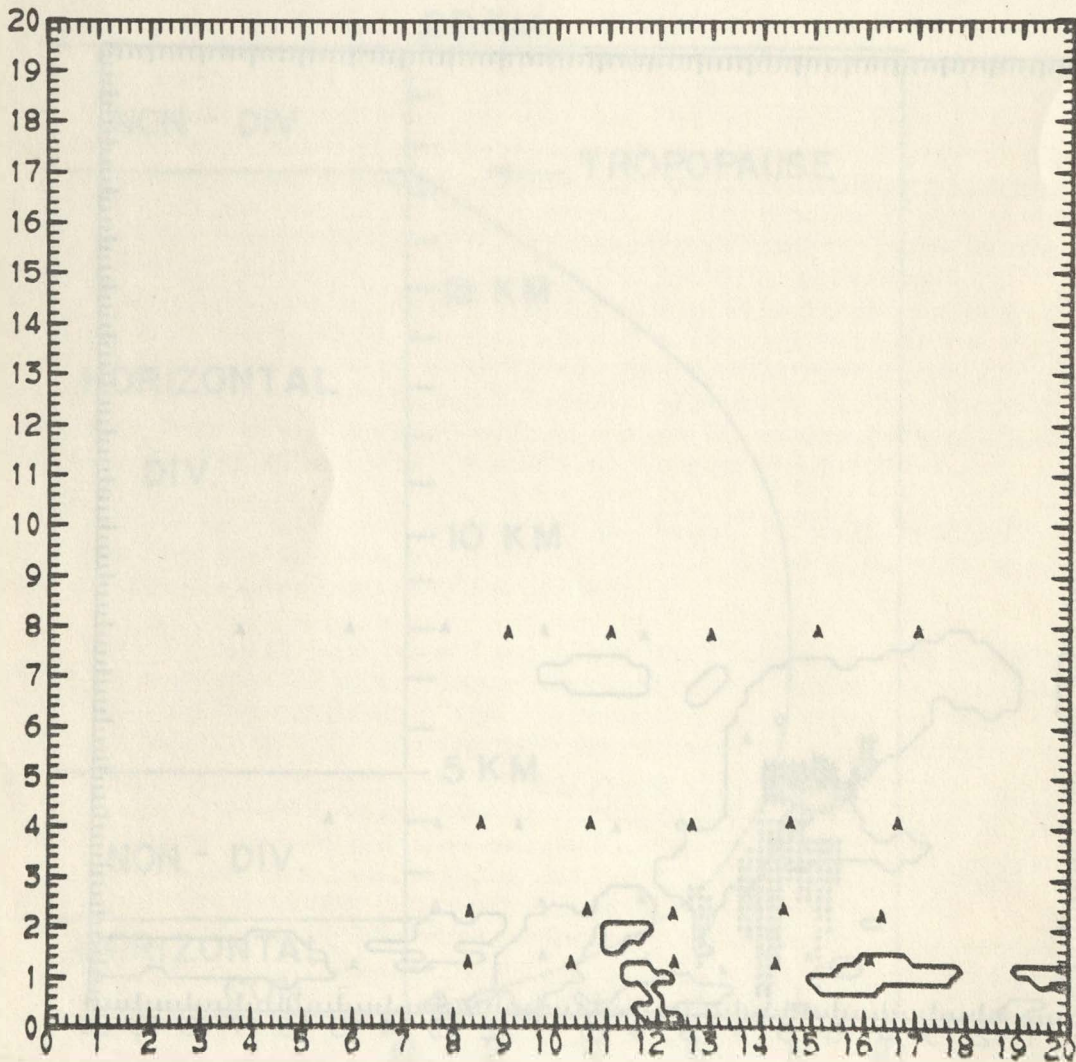


Fig. 9. Case 2 at 108 min.

exactly the same for the two cases but will operate on slightly different fields (10% greater water content in regions of strongest upward motion in Case 1). Thus the clouds are formed by slightly different hydrothermal perturbations but still, we think, must owe the major part of their additional growth to the modified stability of the environment.

3.2 The Small Scale Seeding Experiment

The second experiment is to seed a small area in the rainband to investigate the interaction between seeded and unseeded clouds. The seeding is simulated by freezing the supercooled cloud water instantaneously and isobarically. The experiment is done on Case 1 with the cloud water freezing temperature set at -10°C .

This seeding experiment is conducted at 147 min. The maximum updraft never exceeds 9 m sec^{-1} and the maximum rain content is less than 3 g kg^{-1} throughout the integration, shown in Figs. 10-17. Figure 10 shows the cloud profiles and the stream function at 147 min in Case 1. The seeding target is the active cell in the middle of the model domain with its top at 7 km. The cloud tops in this seeded case, Case 1A, ascend to 10 km at a growth rate of 250 m min^{-1} 29 min after the seeding while the clouds in the natural case ascend comparatively slowly to 9 km (Fig. 17). A temperature increase of $1-2^{\circ}\text{C}$ is found and the local updraft in the seeded area is increased 20 percent. Figures 11, 13, and 15 demonstrate the stream function and cloud profiles at 153, 156, and 159 min for Case 1 and Figs. 12, 14, and 16 for the corresponding situation for Case 1A. At 153 min (Fig. 12), the seeded cell develops an updraft over a depth of 4 km shown by the stream function pattern. The unseeded cell is influenced by the compensating downdraft of the seeded cell. Three minutes later, at 156 min (Fig. 14), the unseeded cell is 200 m lower than it was at 153 min and is 200 m lower than the same cell in Case 1 (Fig. 14). Also, the seeded cell is higher than the unseeded cell at this moment, while in the natural case that cell is lower (Fig. 17). At 159 min (Fig. 16), a closed circulation is formed above the unseeded cell, which is almost completely evaporated. The unseeded cell is suppressed by the compensating motion that has developed in association with the seeded cell.

There is scarcely any difference between Case 1 and Case 1A in the precipitation accumulated up to 189 min. The cell at the left has passed its mature stage when the seeding is conducted, little precipitation is produced after the seeding in both cases. The seeded cell increases its updraft by 20 percent, which suspends the slowly falling precipitating ice.

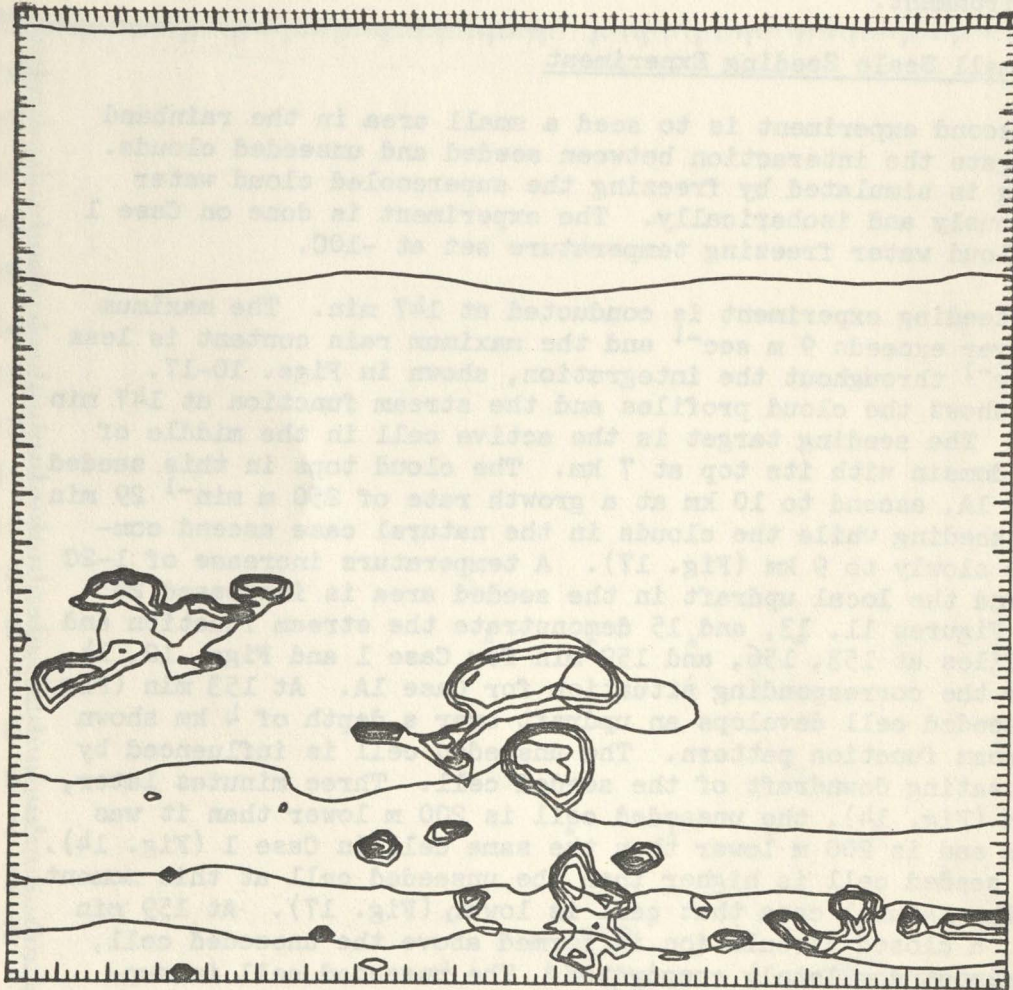


Fig. 10. Cloud outline (contours of cloud water content every 0.25 g kg^{-1}) and stream function at 147 min when small scale seeding is conducted.

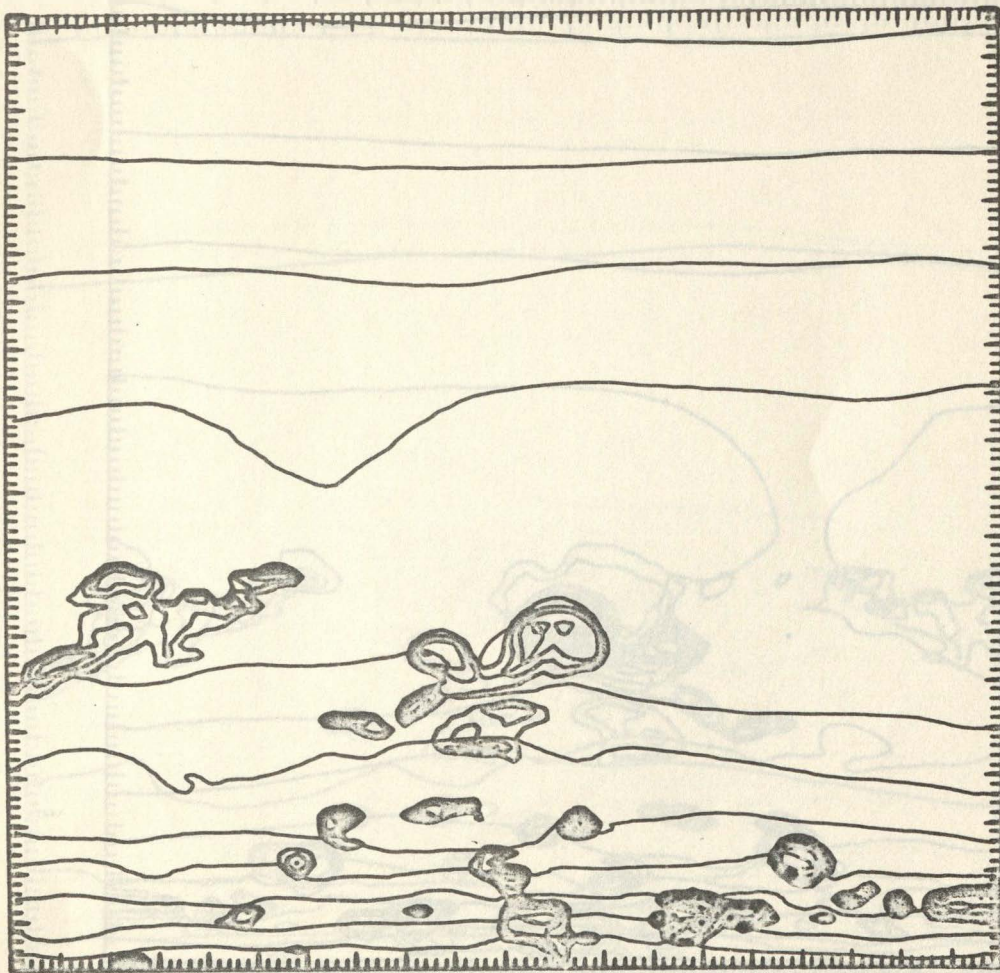


Fig. 11. Case 1 at 153 min.

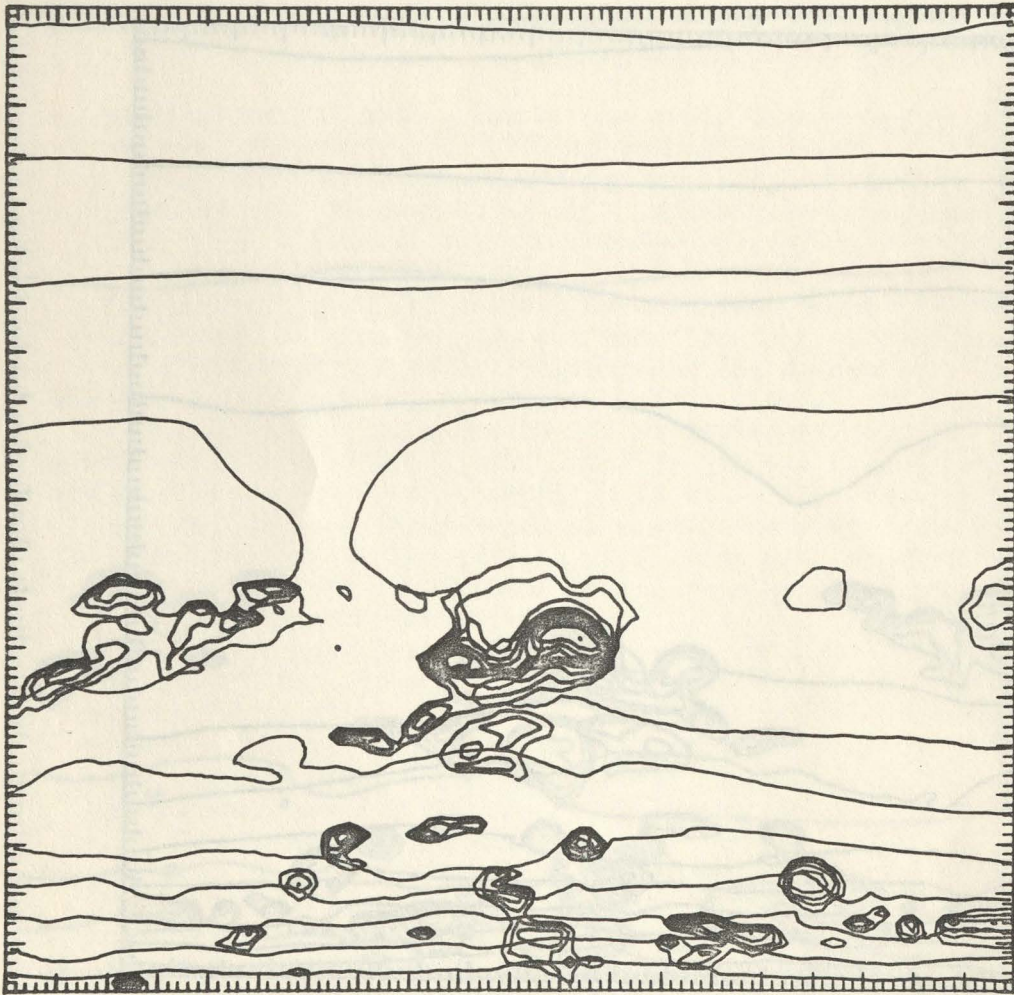


Fig. 12. Case 1A at 153 min.

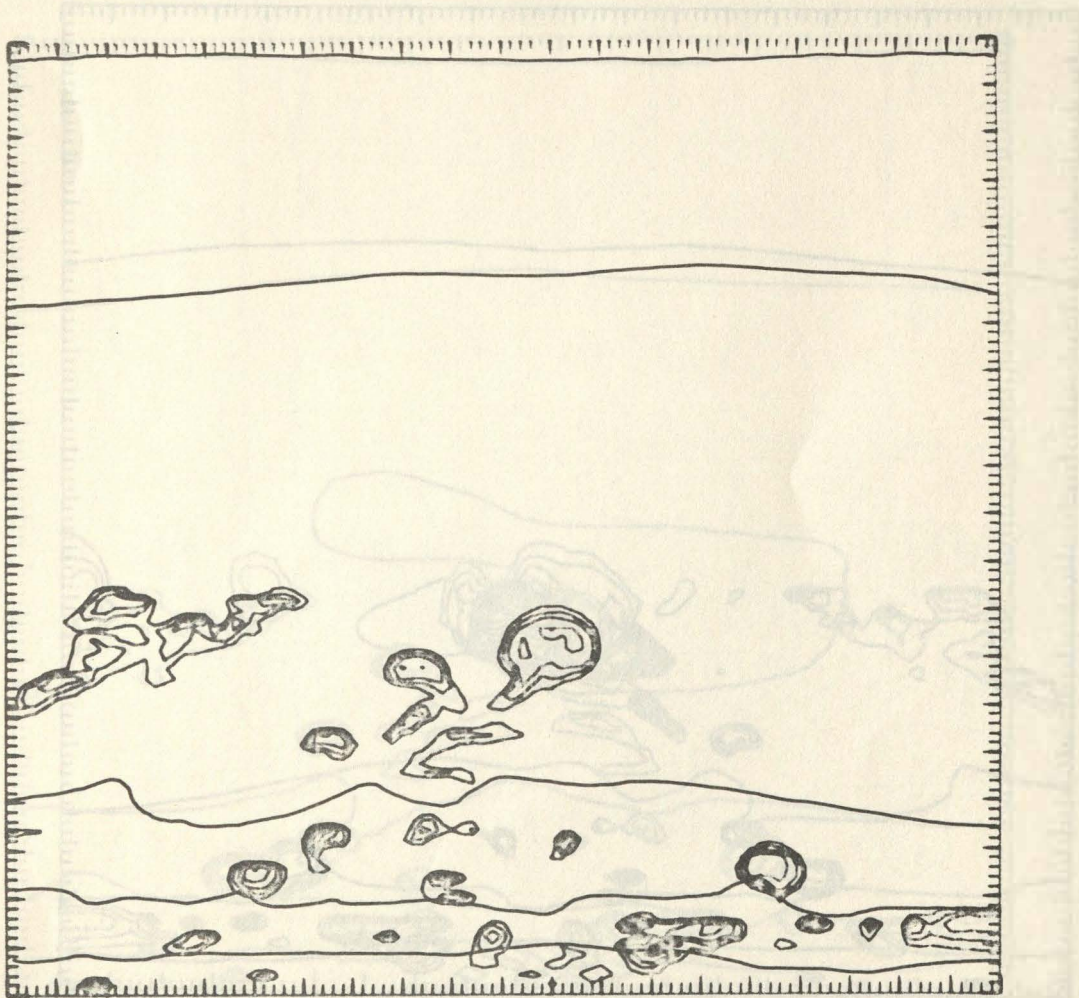


Fig. 13. Case 1 at 156 min.

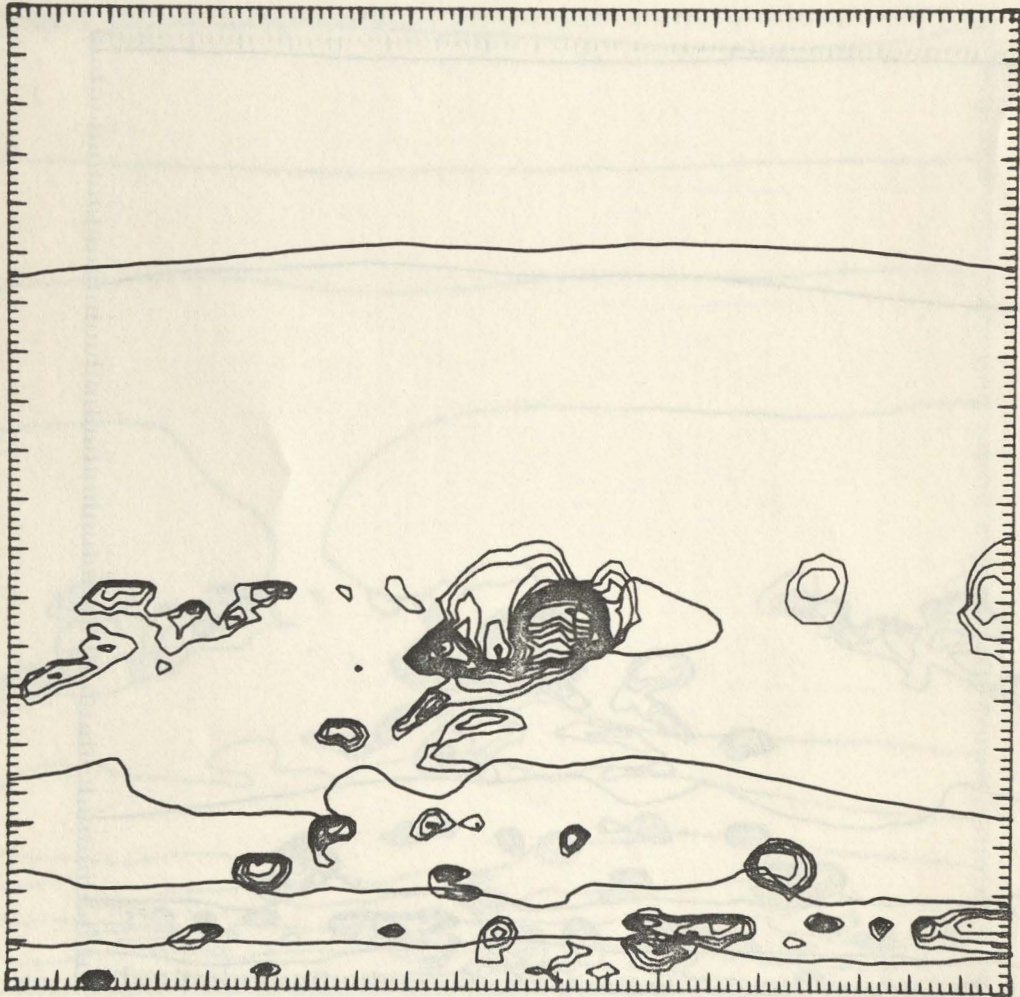


Fig. 14. Case 1A at 156 min.

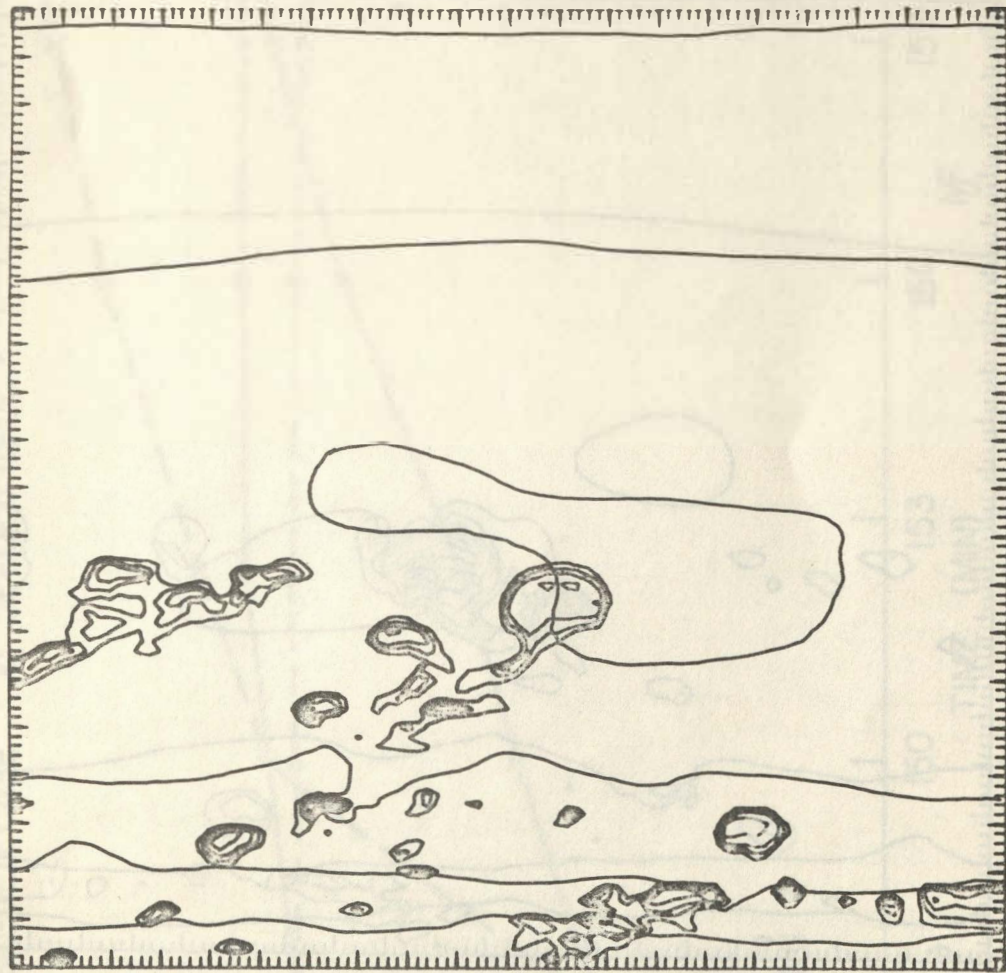


Fig. 15. Case 1 at 159 min.

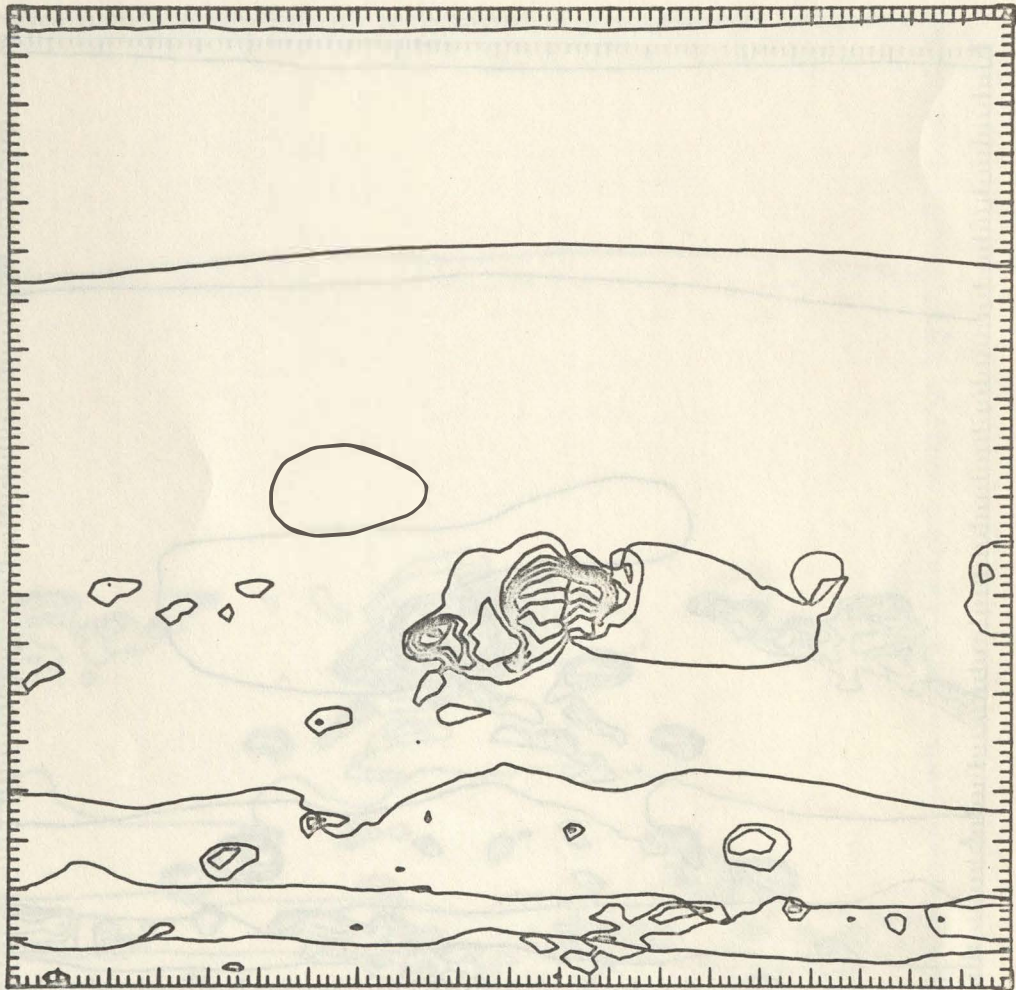


Fig. 16. Case 1A at 159 min.

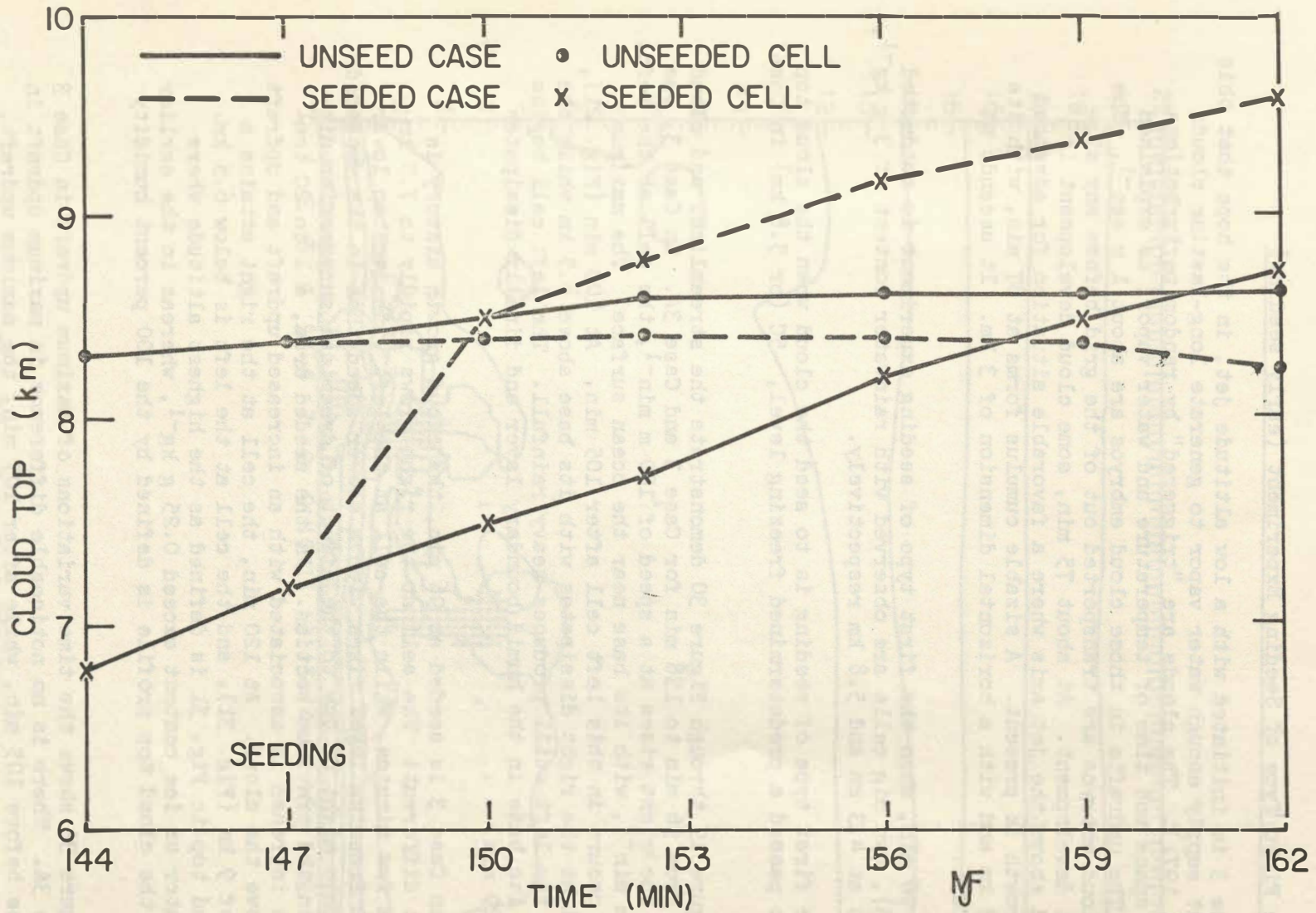


Fig. 17. Time variations of seeded and unseeded cloud tops in Case 1 and Case 1A. Cloud tops defined as the maximum height of the 0.25 g kg^{-1} CWC (cloud water content) isoline.

3.3 The First Type of Seeding Experiment (early seeding)

Case 3 is initiated with a low altitude jet, in the hope that this jet might supply enough water vapor to generate long-lasting clouds (Takeda, 1971). The clouds are "triggered" by random perturbations in both space and time of temperature and water vapor, as explained above. The updrafts in those cloud embryos are about 1 m sec^{-1} . The early cloud embryos are transported out of the grid before any significant development. At about 75 min, some cloud development is observed above the jet axis where a favorable situation for advanced cloud growth is present. A sizable cumulus forms at 87 min, with its top at 3 km and with a horizontal dimension of 3 km. It ascends at 100 m min^{-1} .

At 96 min, when the first type of seeding experiment is conducted (Fig. 18), two big cells are observed with rainwater content of 3 g kg^{-1} , and tops at 4.3 km and 5.8 km respectively.

The first type of seeding is to seed the cloud when the cloud top has just passed a predetermined freezing level, -5C (or 5.8 km) in Case 3A.

Figure 19 through Figure 30 demonstrate the streamlines and cloud profile from 96 min to 138 min for Case 3 and Case 3A. In Case 3, the cell at the right rises at a speed of 100 m min^{-1} , the cell at the left, at 150 m min^{-1} , with its base near the ocean surface. The maximum updraft occurs in this left cell after 105 min. At 108 min (Fig. 21), the cell at the right dissipates with its base above 4.5 km while the cell at the left still produces heavy rainfall. The left cell begins to lose its base in the humid boundary layer and finally dissipates after 129 min.

When Case 3 is seeded at 96 min, the cloud growth history is somewhat different. The cell at the right grows rapidly to 7.5 km within a few minutes, while the cell at the left with its top lower than the freezing level rises with a slower speed than in the unseeded case. This might be due to the effect of dynamical suppression discussed in the previous section. In the seeded area, a 1 to 2C temperature increase is associated with an increased updraft and updraft area above the cloud. At 120 min, the cell at the right attains a height of 9 km (Fig. 31), and the cell at the left is below 6.5 km. The cloud top in Fig. 31 is defined as the highest altitude where cloud water or ice content exceed 0.25 g kg^{-1} , whereas in the earlier figures the cloud top profile is defined by the 100 percent humidity line.

Figure 32 shows the time variations of maximum updraft in Case 3 and Case 3A. There is no noticeable difference in maximum updraft in two cases before 105 min, while after 105 min, the maximum updraft, which occurs in the cell at left in Case 3A, is stronger than in

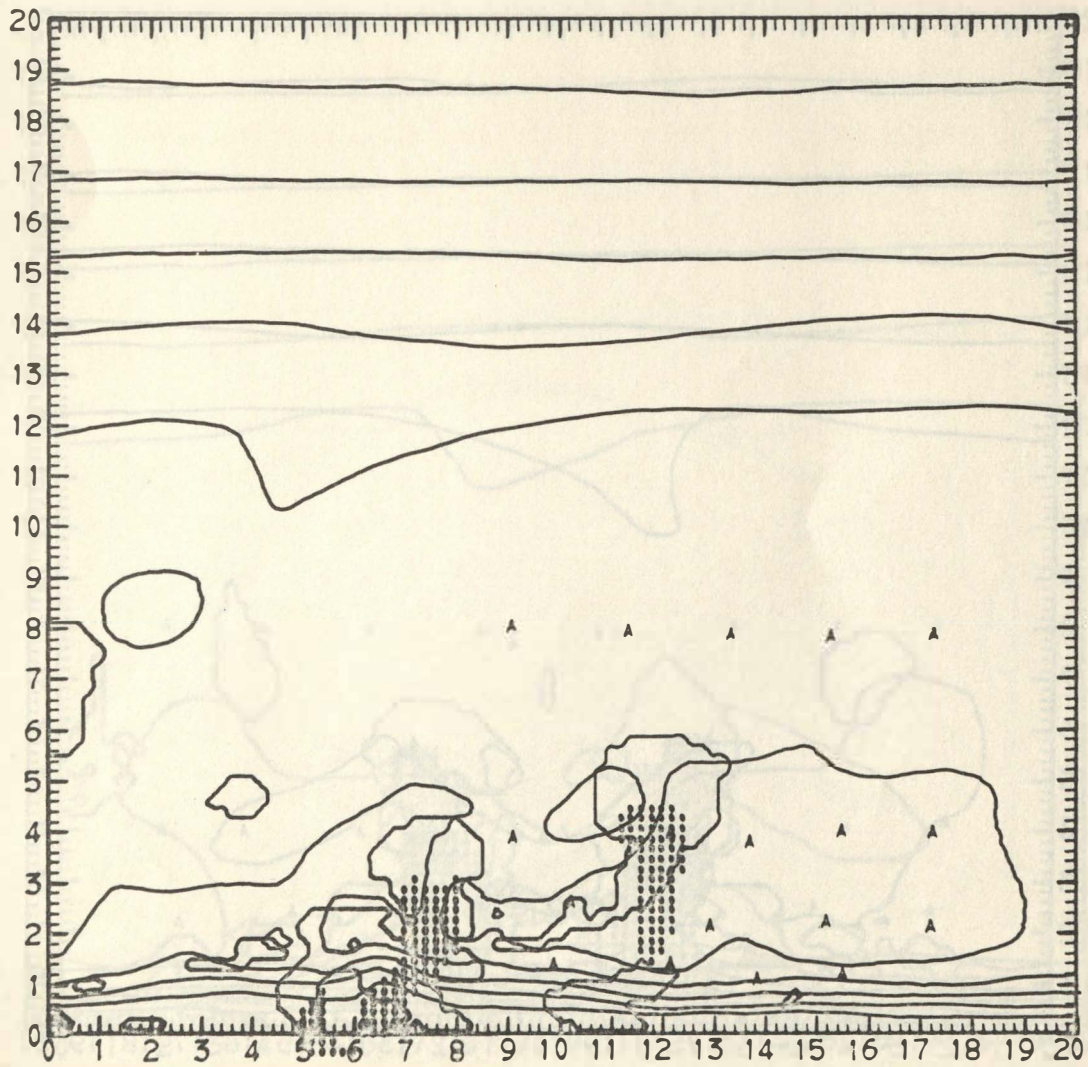


Fig. 18. Case 3 at 96 min.

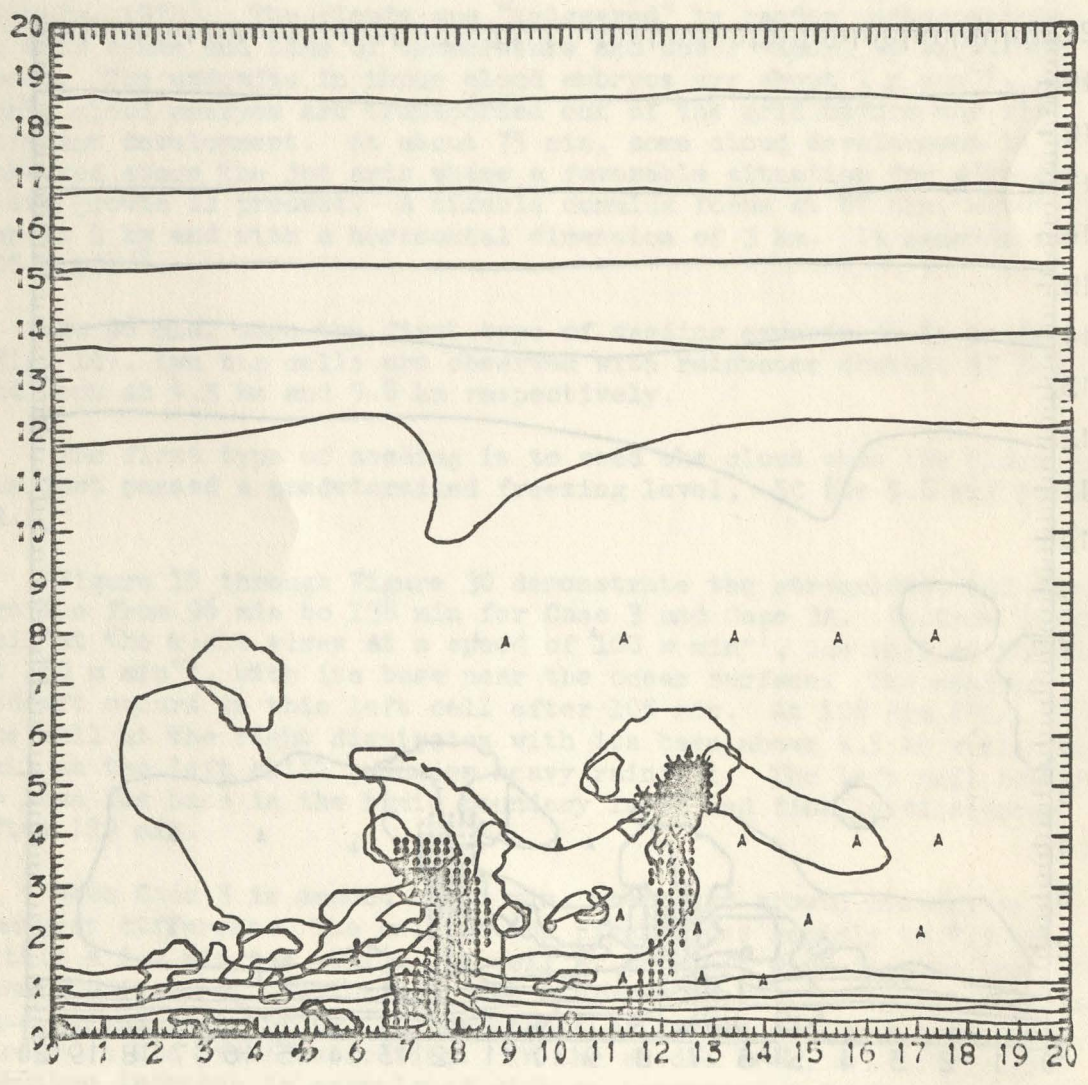


Fig. 19. Case 3 at 102 min.

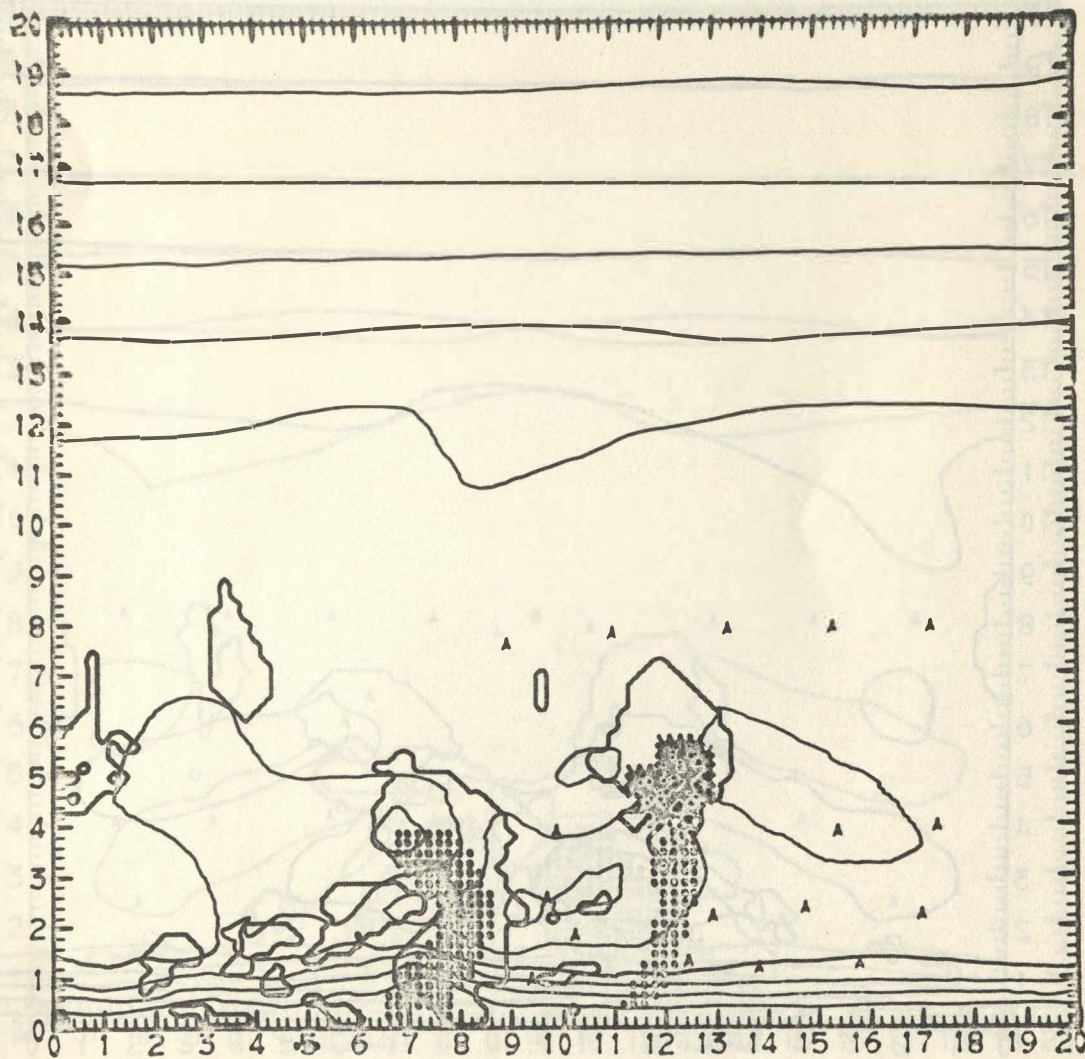


Fig. 20. Case 3A at 102 min.

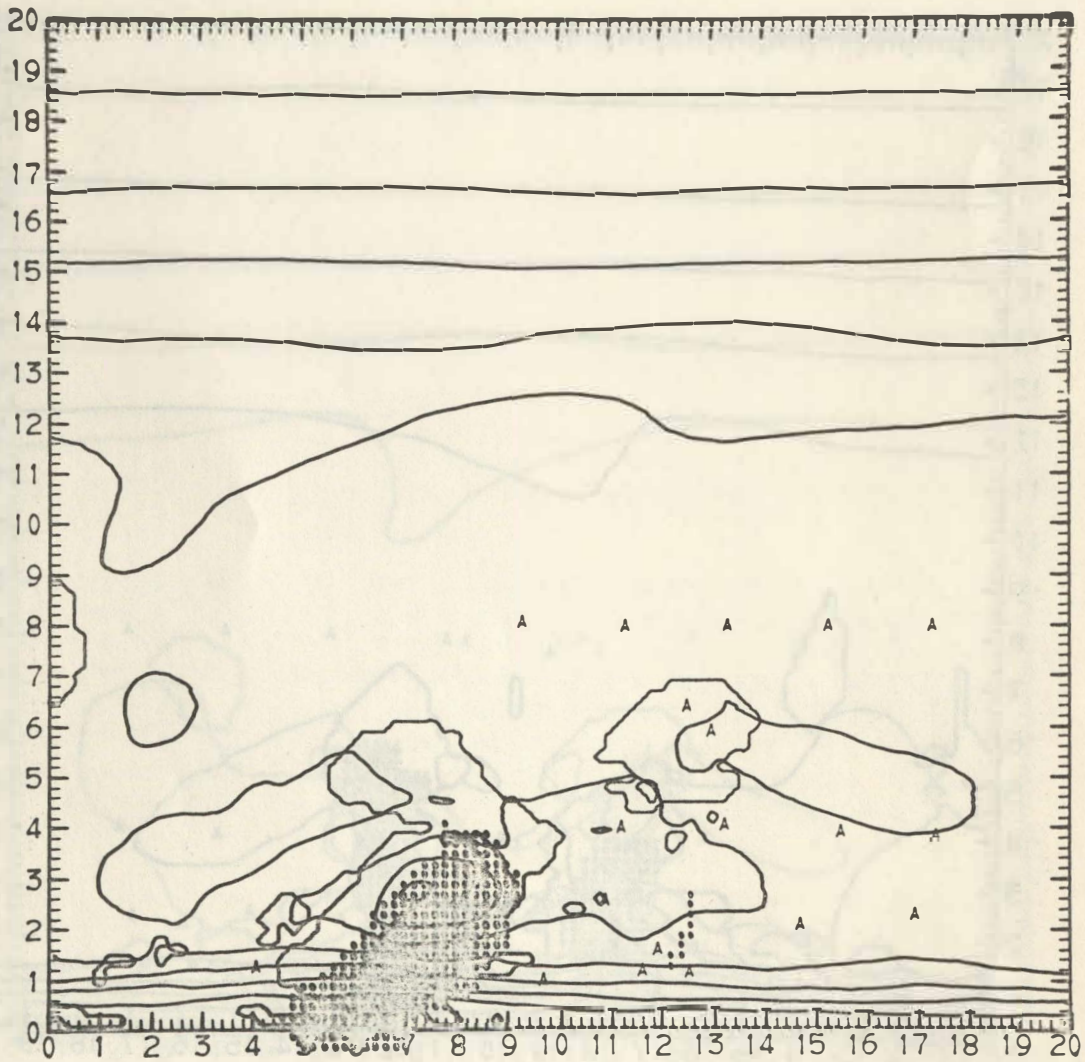


Fig. 21. Case 3 at 108 min.

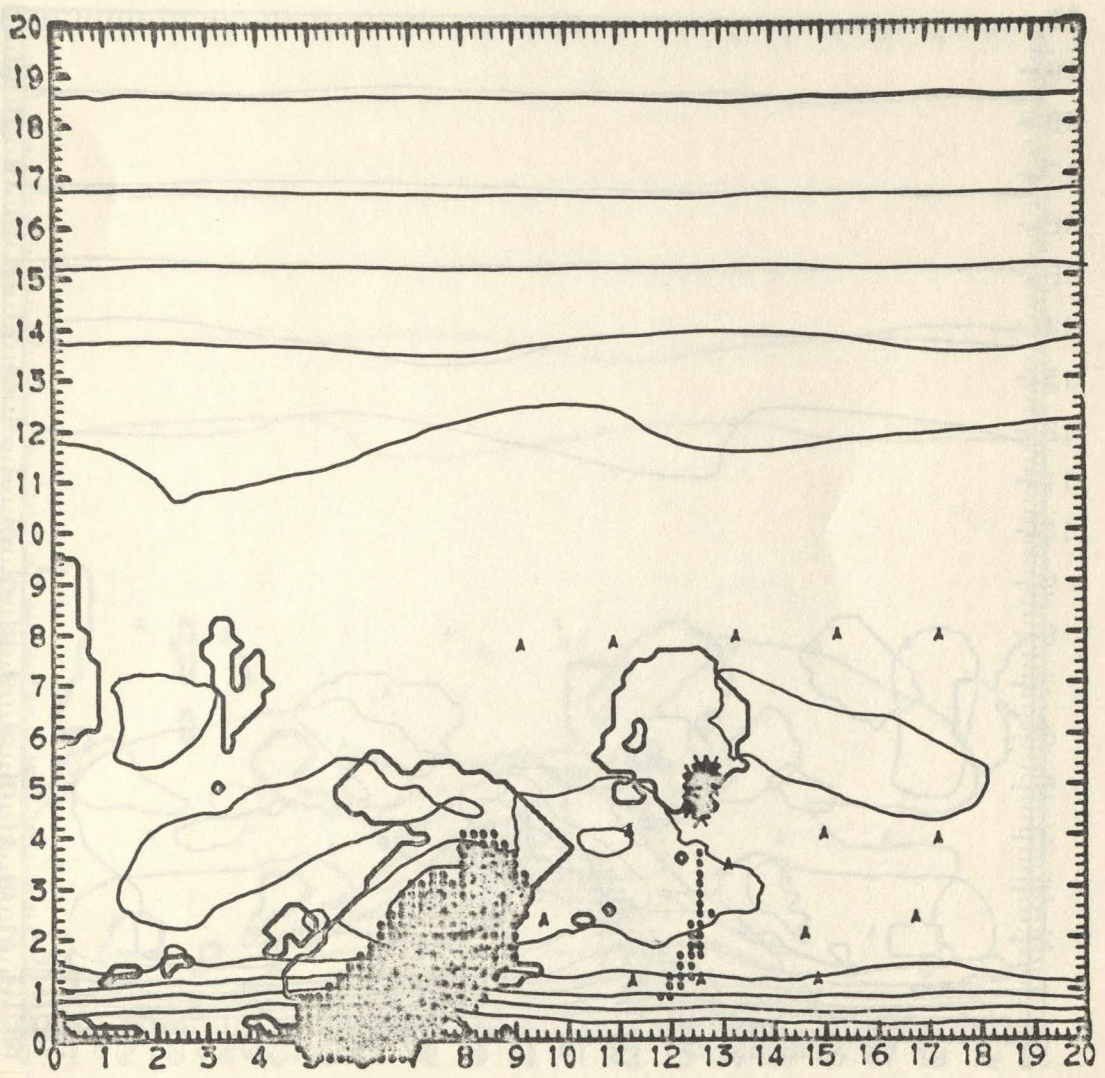


Fig. 22. Case 3A at 108 min.

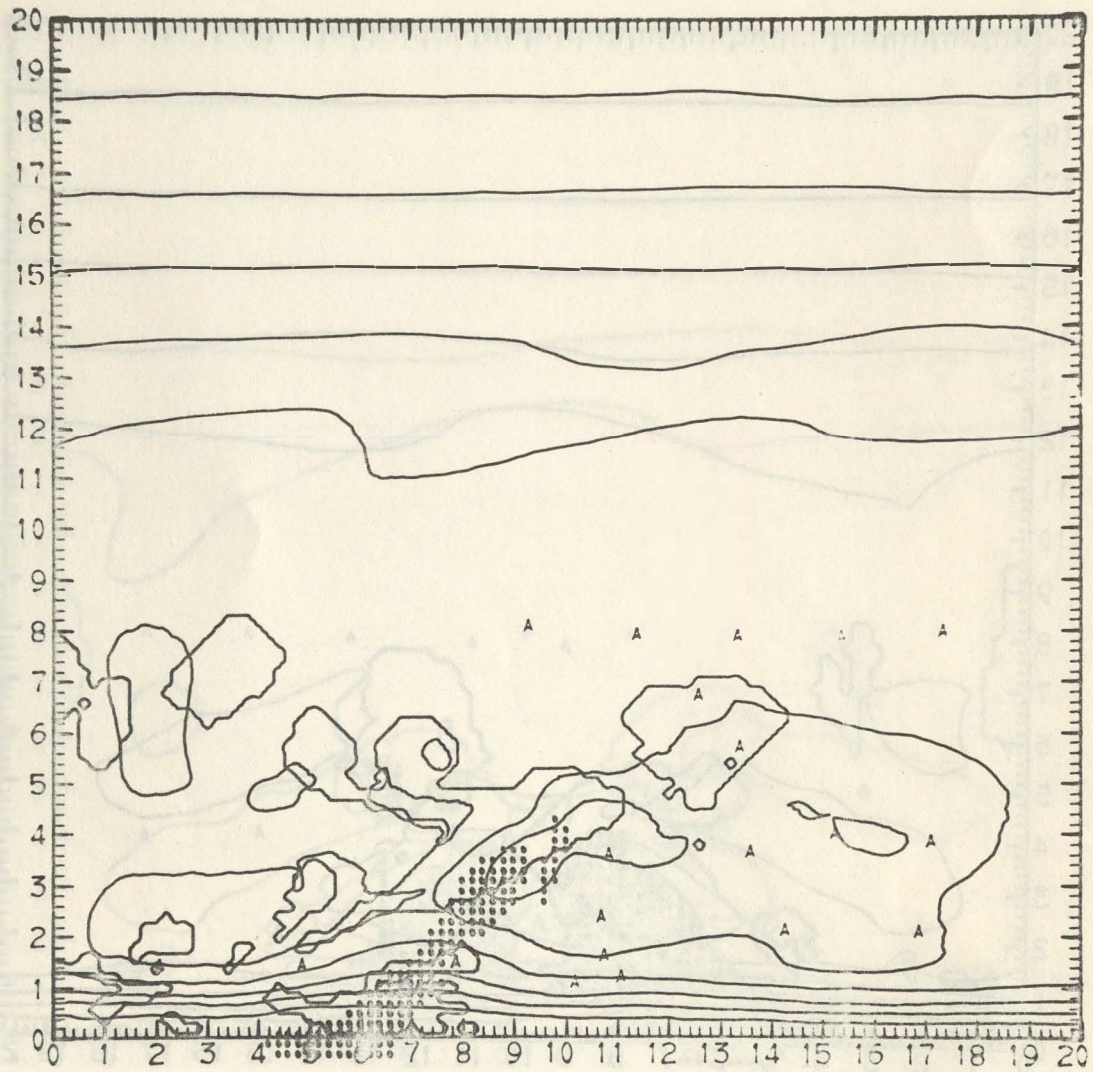


Fig. 23. Case 3 at 114 min.

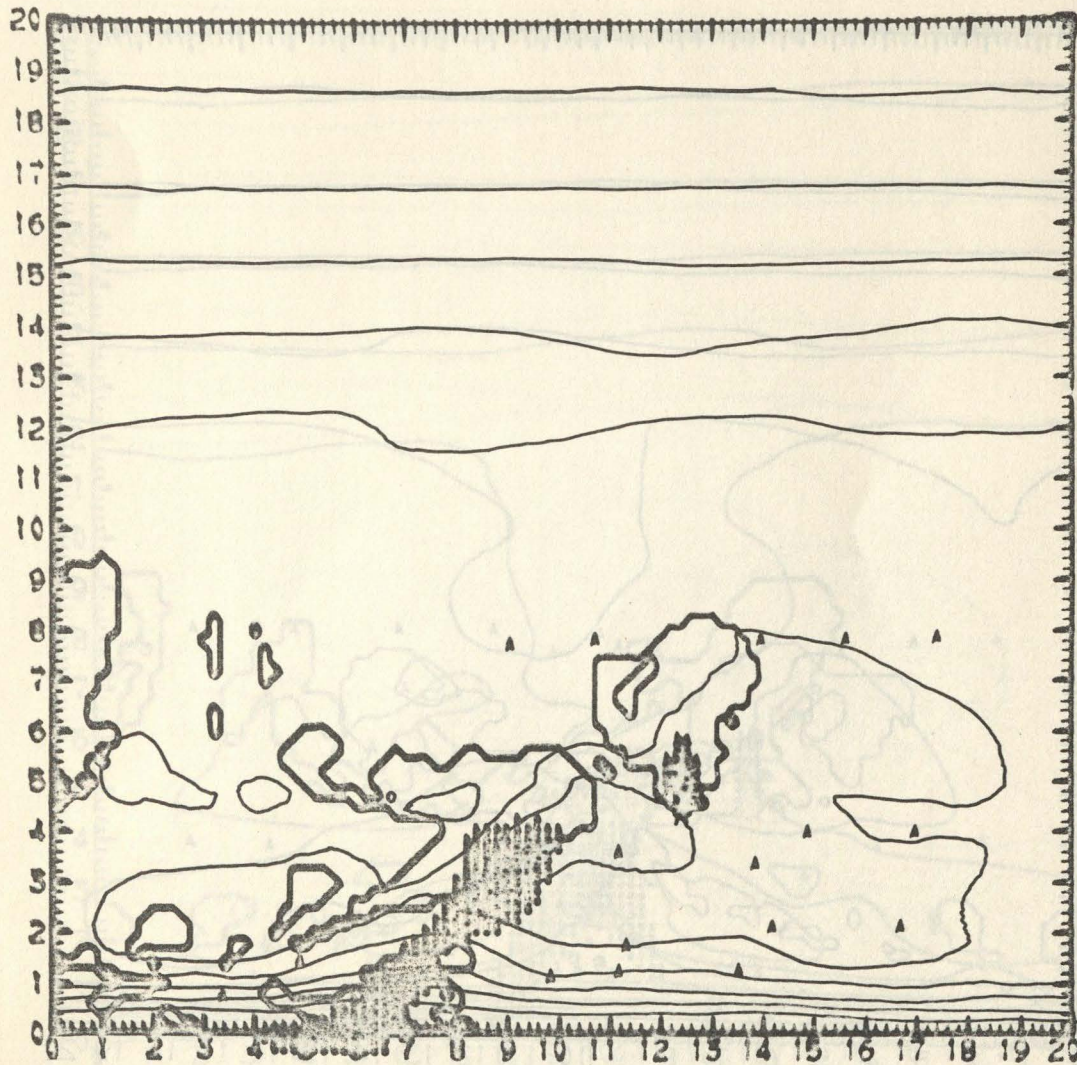


Fig. 24. Case 3A at 114 min.

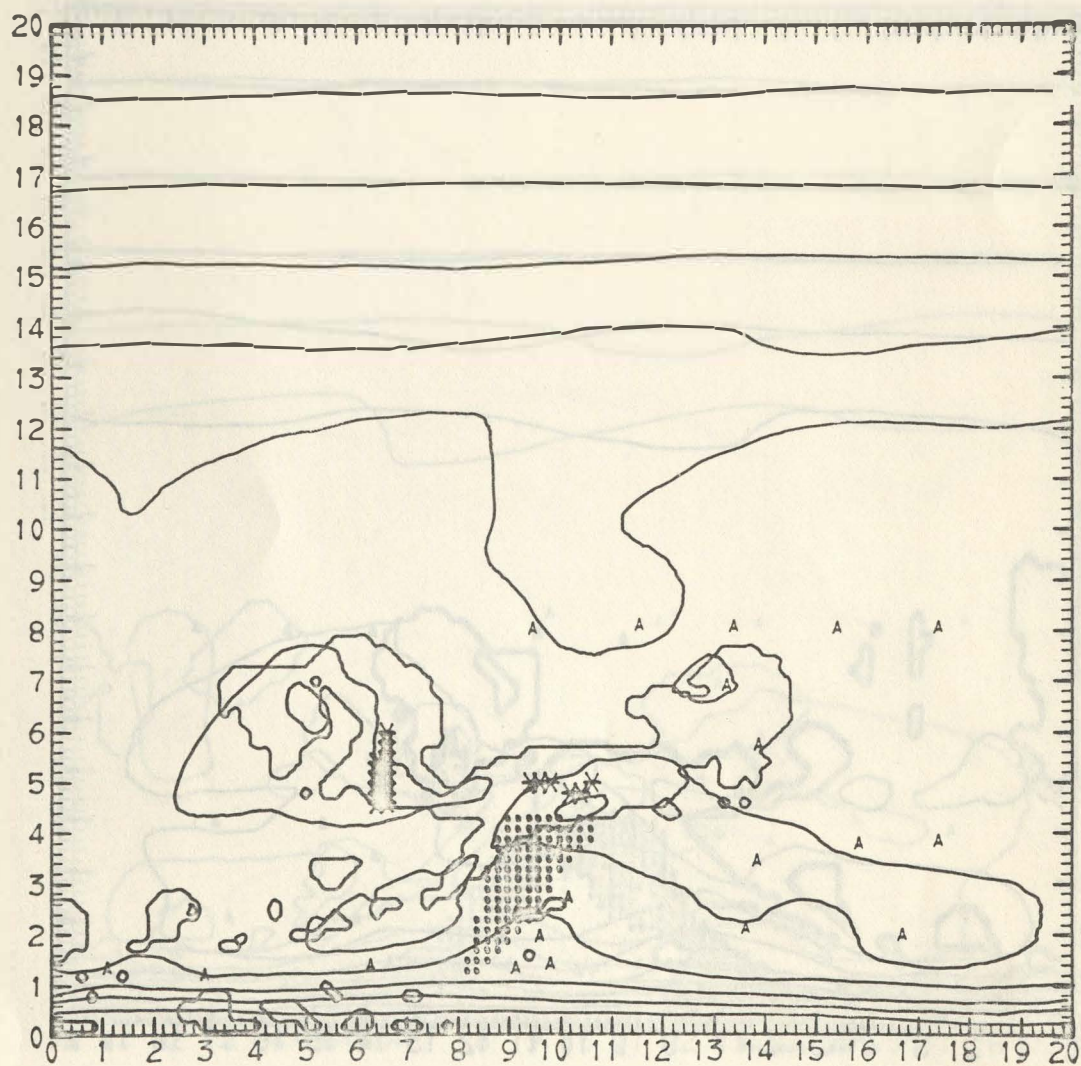


Fig. 25. Case 3 at 120 min.

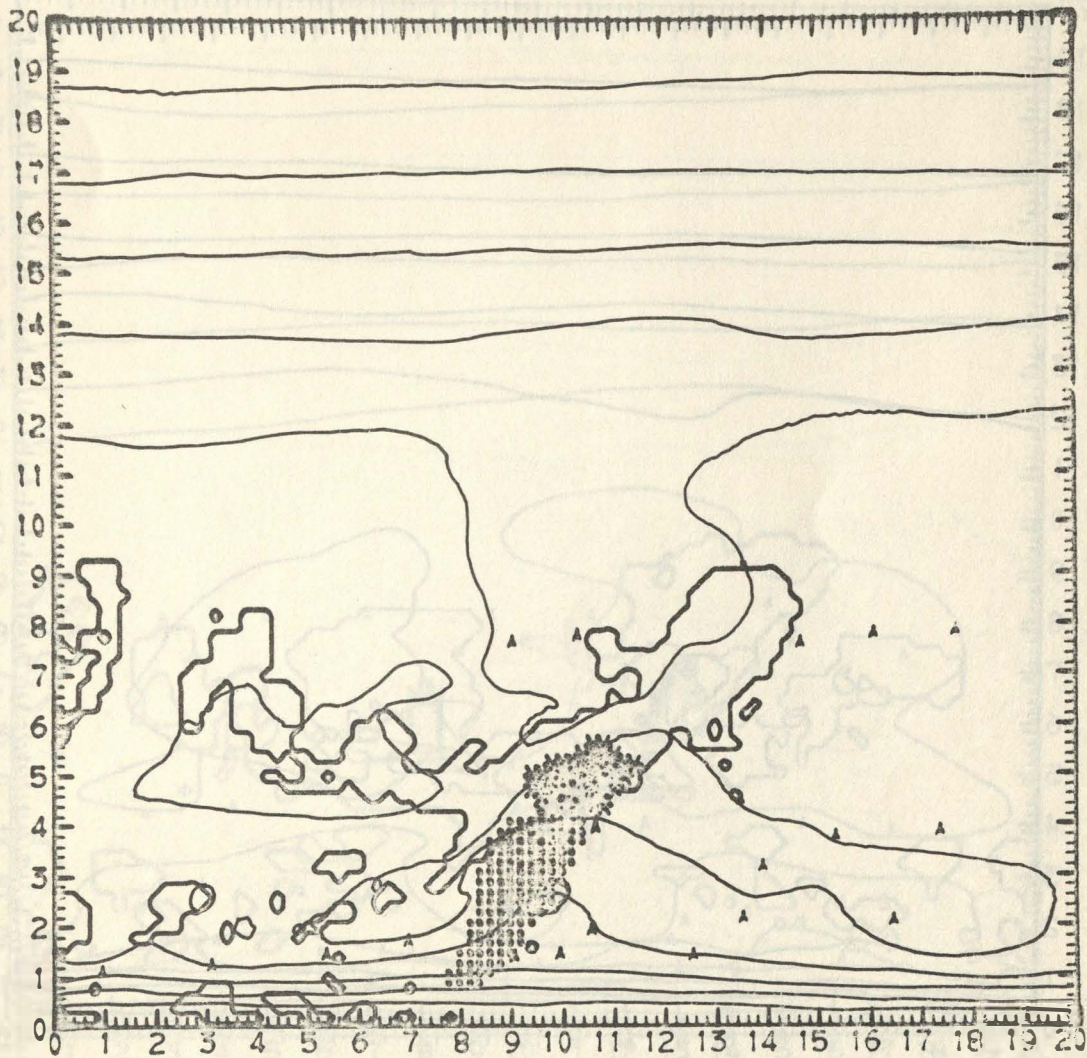


Fig. 26. Case 3A at 120 min.

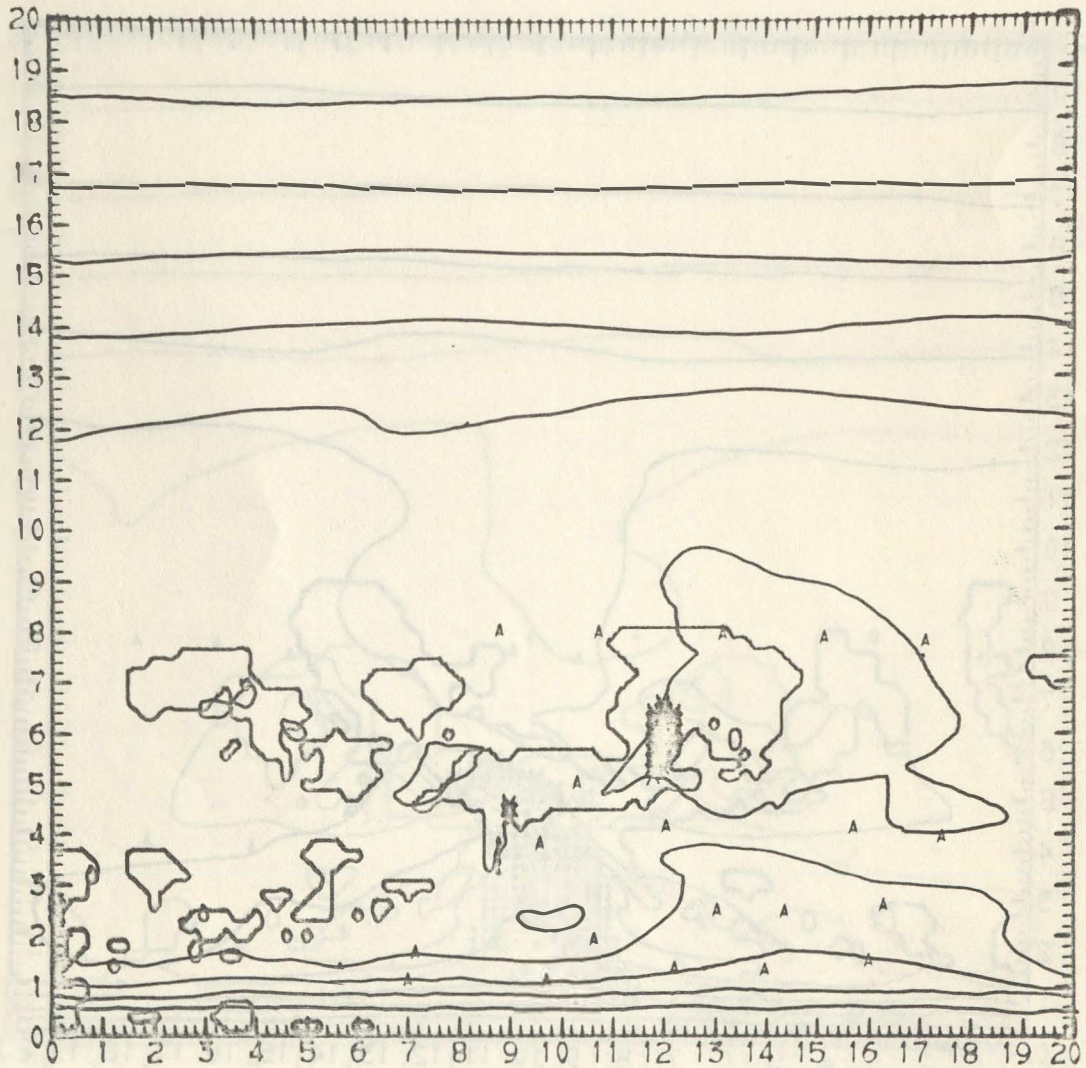


Fig. 27. Case 3 at 129 min.

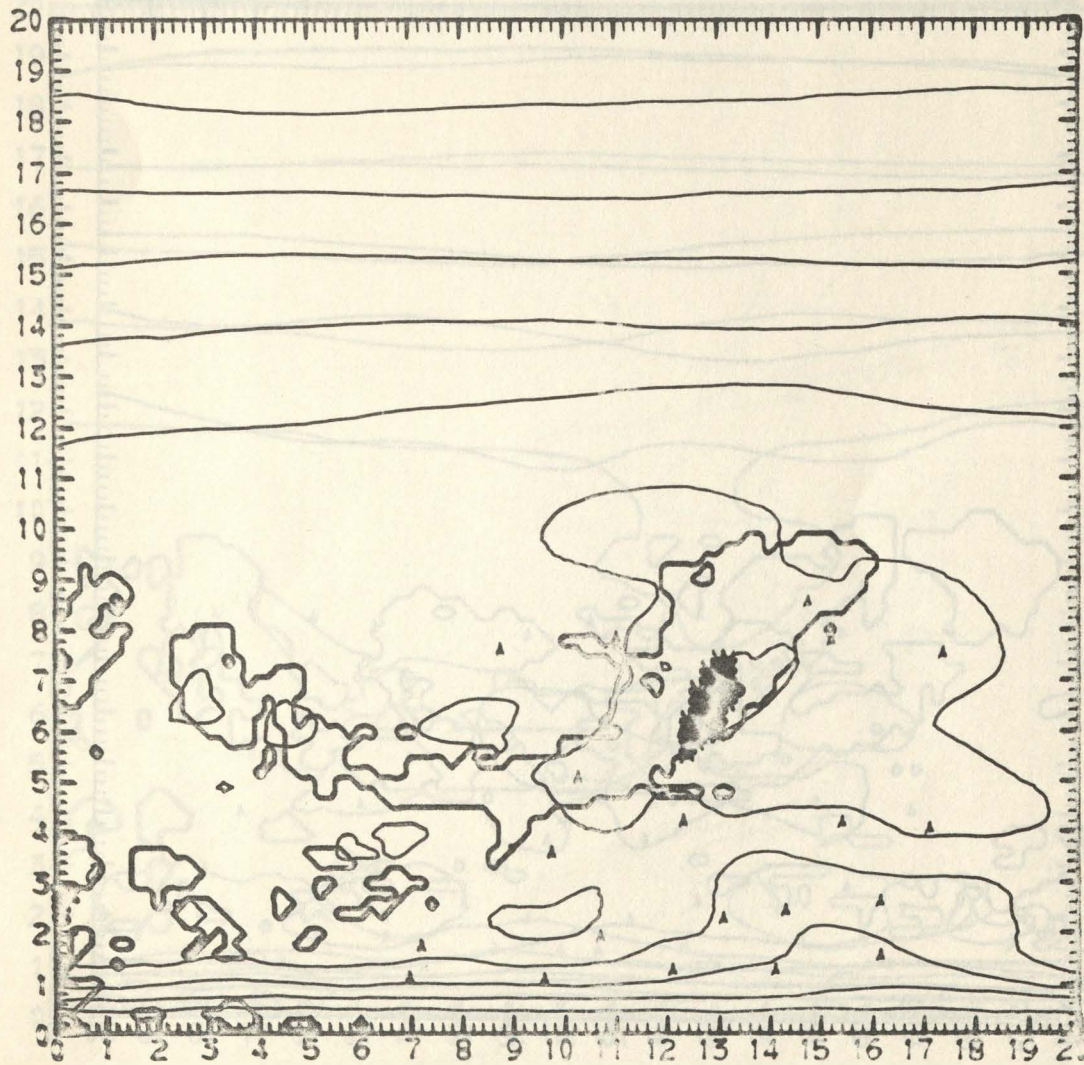


Fig. 28. Case 3A at 129 min.

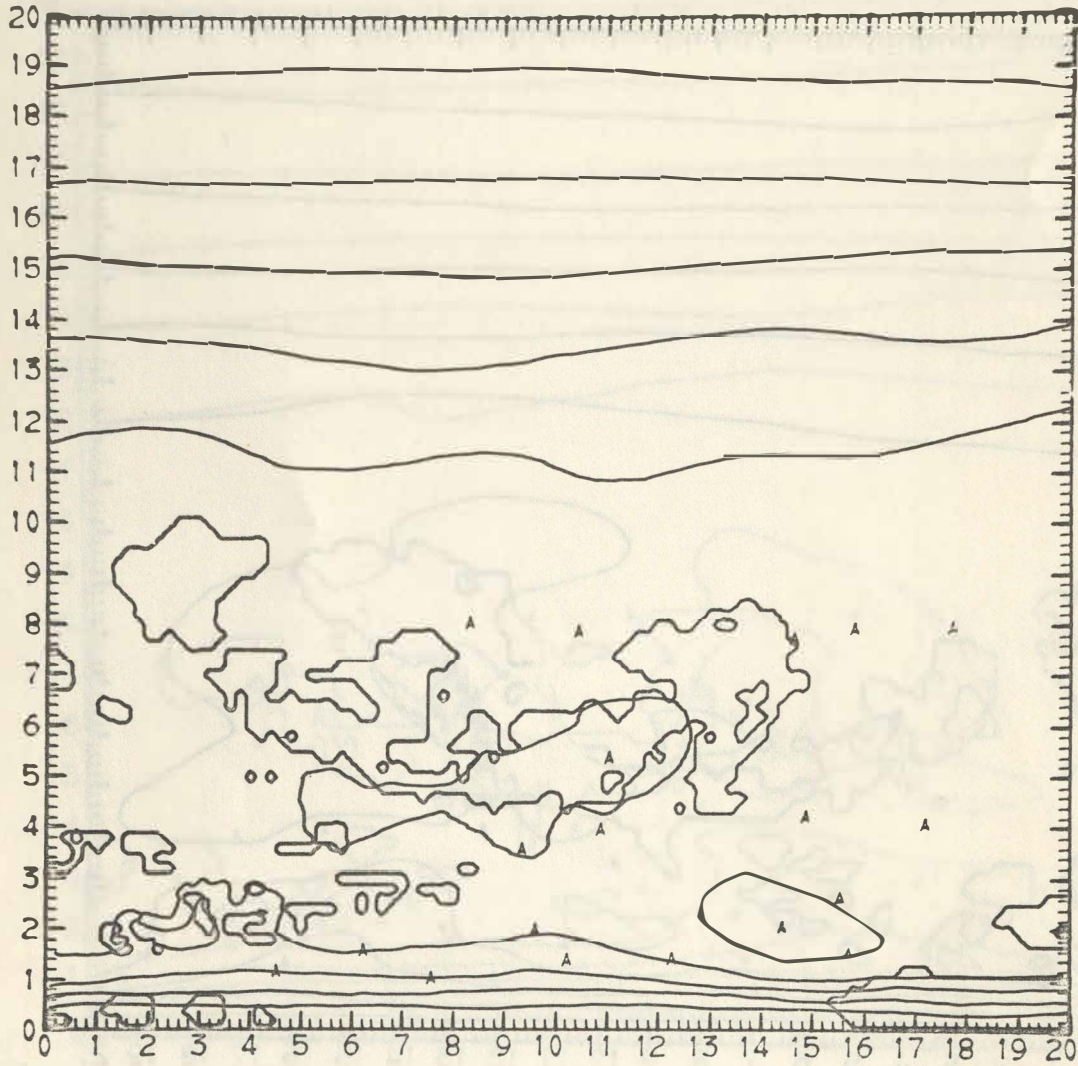


Fig. 29. Case 3 at 138 min.

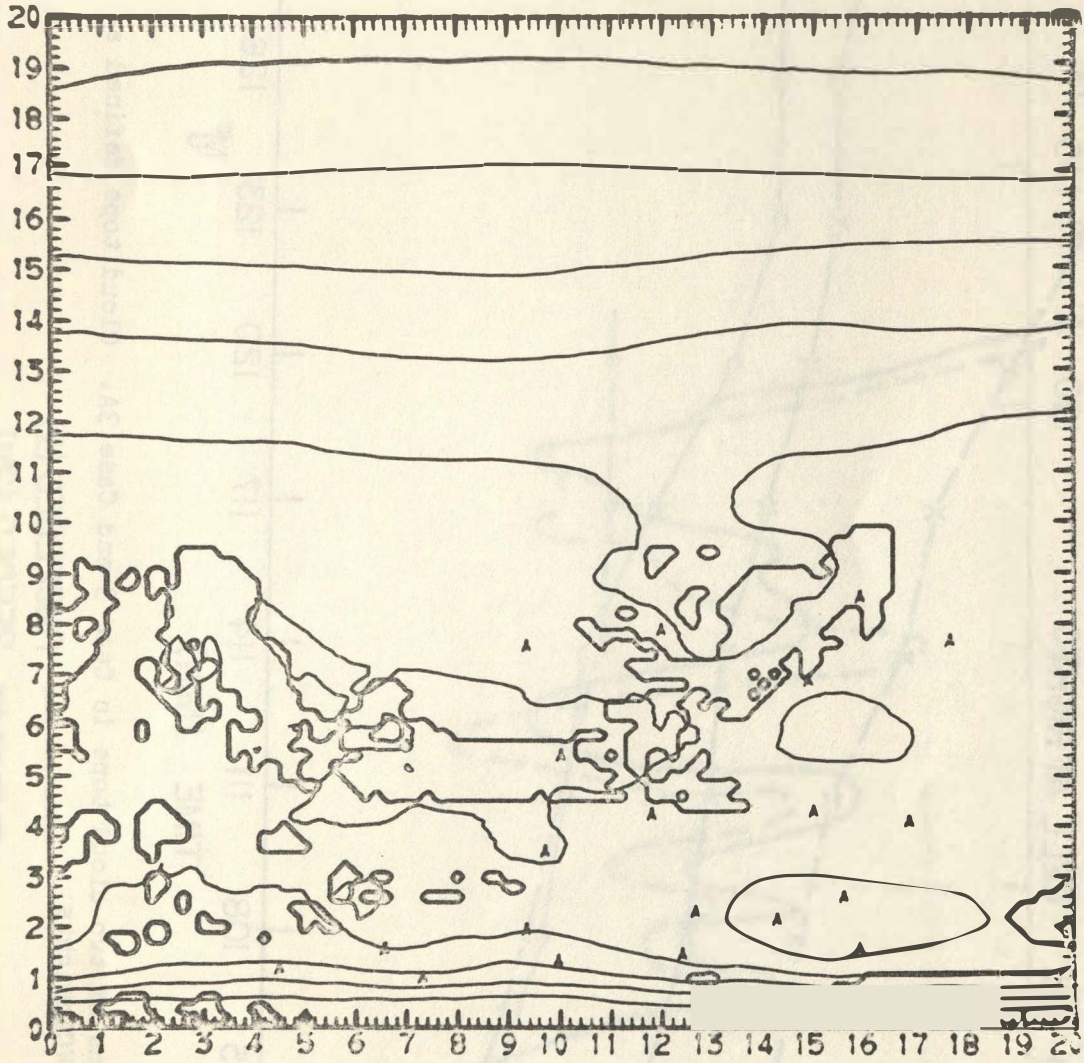


Fig. 30. Case 3A at 138 min.

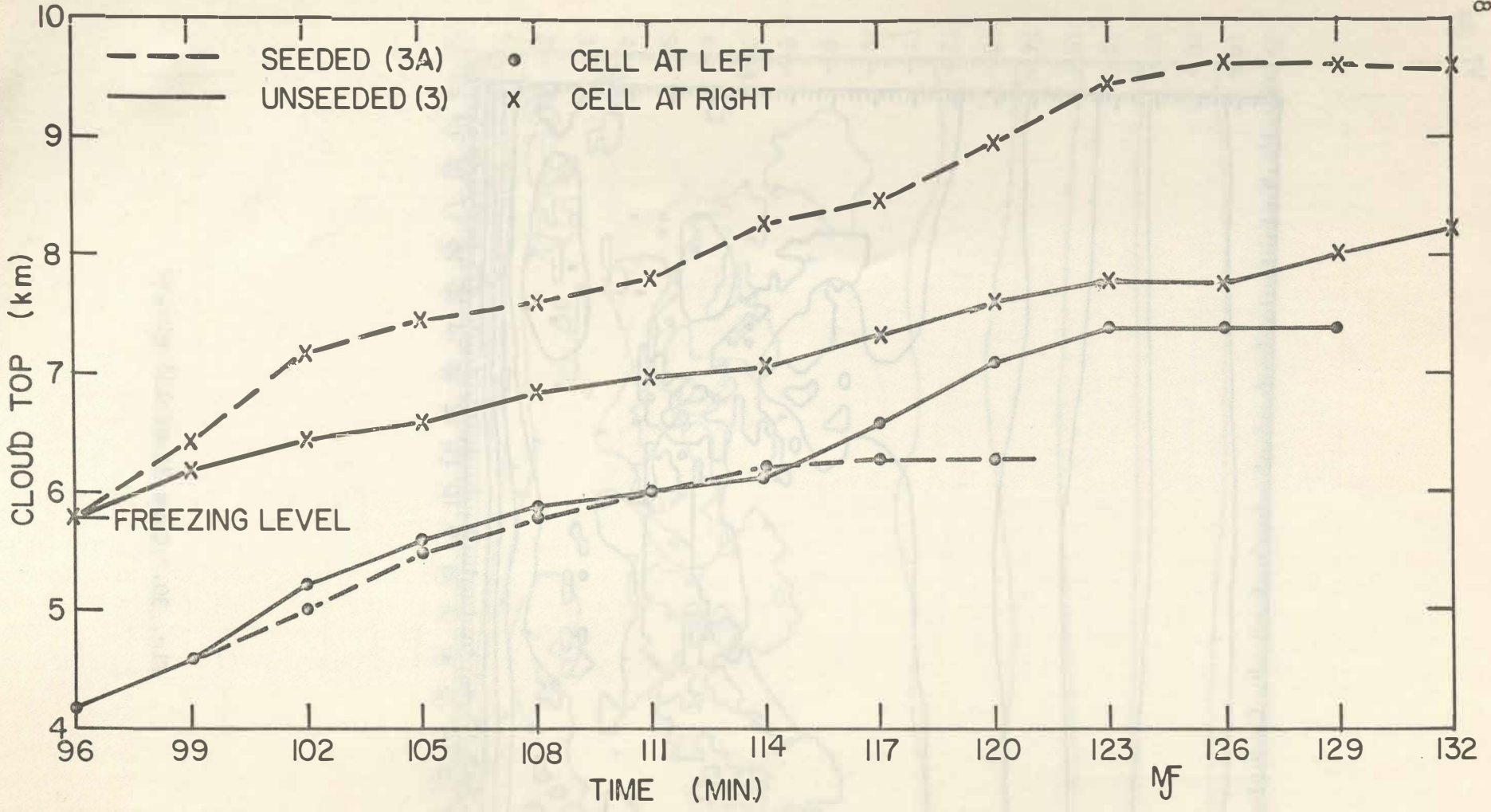


Fig. 31. Time variations of two cloud tops in Case 3 and Case 3A. Cloud tops defined as 0.25 g kg^{-1} CWC heights.

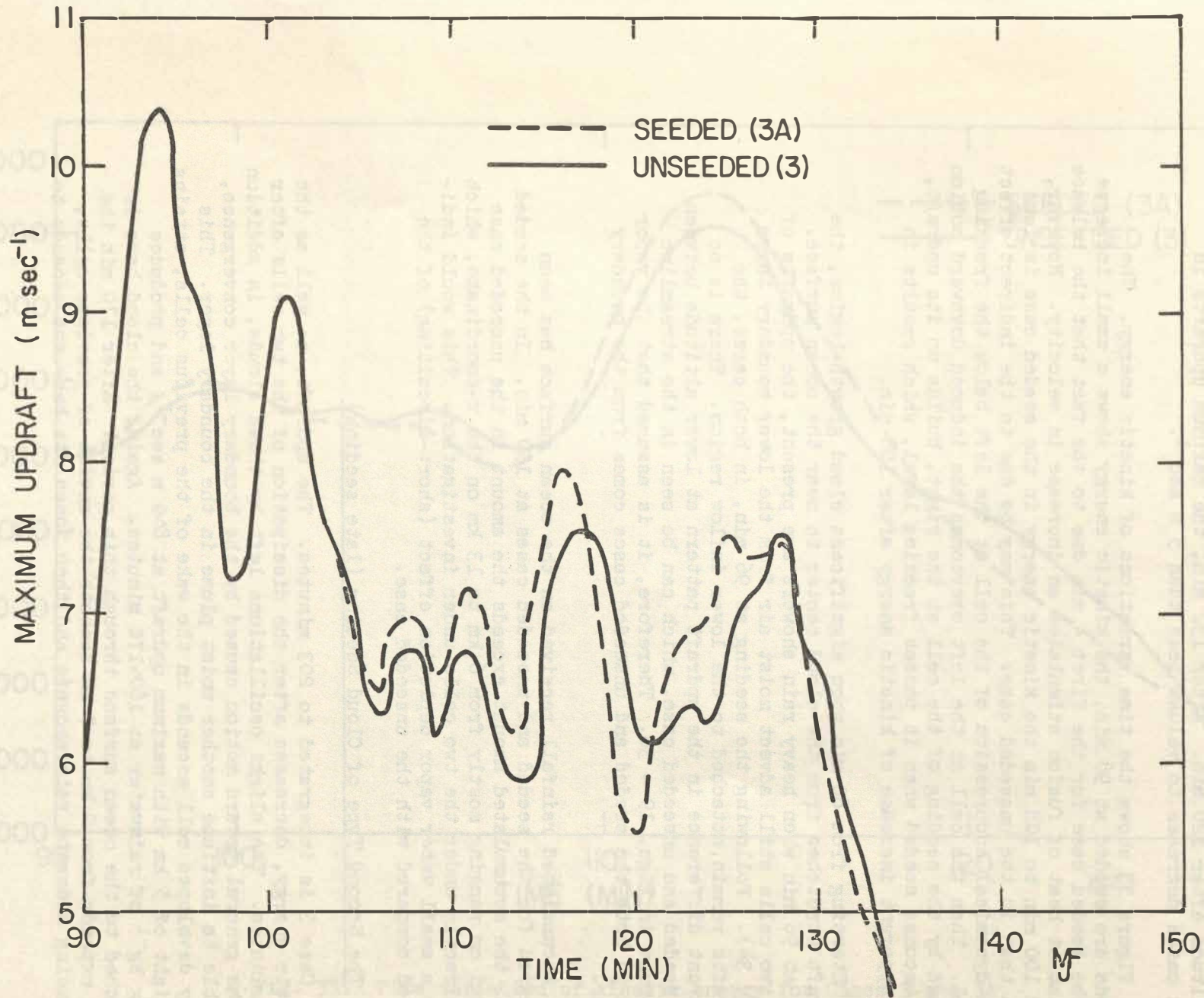


Fig. 32. Time variation of maximum updrafts for Cases 3 and 3A.

Case 3 by 0.5 m sec^{-1} to 1 m sec^{-1} . It oscillates with a larger amplitude after 120 min. After 132 min, the maximum updrafts in both cases decrease to values less than 5 m sec^{-1} .

Figure 33 shows the time variations of kinetic energy. The clouds are seeded at 96 min, the kinetic energy shows a small increase in the seeded case for the first 4 min due to the fact that the release of latent heat of fusion stimulates an increase in velocity. However, from 100 min to 108 min the kinetic energy in the seeded case is less than that in the unseeded case. This may be due to the indirect effect of a dynamical suppression of the cell at the left below the freezing level. Then the cell at the left overcomes the induced downward motion caused by the seeding of the cell at the right, builds up its updraft, and becomes seeded when it passes freezing level, which results in the apparent increase of kinetic energy after 108 min.

Starting from 80 min when significant cloud growth begins, the updraft stretches from the cloud center to near the ocean surface. Even at 96 min when heavy rain showers are present, the updrafts of the two cells still advect moist air from the lower boundary layer (Fig. 34). Following the seeding at 96 min, in both cases, the updrafts remain attached to the lower inflow region. There is no apparent difference in the updraft pattern at lower altitude between the seeded and unseeded case, which can be seen in the streamline patterns in Figs. 19 - 30. Therefore, it is assumed that the vapor flux in both the seeded and unseeded cases comes from the boundary layer.

Accumulated rainfall received on the ocean surface has been compared for the seeded and unseeded cases at 150 min. In the seeded case, the accumulated amount exceeds the amount in the unseeded case by 0.1 cm ranging mostly from 6 km to 13 km on the x-coordinate, which is directly under the two cells under investigation. This would indicate a small water vapor depletion effect (short-circuiting) of the seeded compared with the unseeded case.

3.4 The Second Type of Cloud Seeding (late seeding)

Case 3 is integrated to 203 minutes. The updraft, as well as the kinetic energy, decreases after the dissipation of the two cells after 135 minutes. The slight oscillations left by these clouds, in addition to the general upward motion caused by the boundary layer convergence, is able to initiate another moist plume in the boundary layer. This newly developed cell ascends in the wake of the previous cells, attains a height of 5 km with maximum updraft at 8.9 m sec^{-1} , and produces 4.5 g kg^{-1} of rainwater at 160-170 minutes. Again, the cloud base is attached to the ocean surface through this period. After 170 min the cell extends from 2 km to 7 km beneath the anvils of previous cells, producing moderate rain showers and then loses its base and ascends to

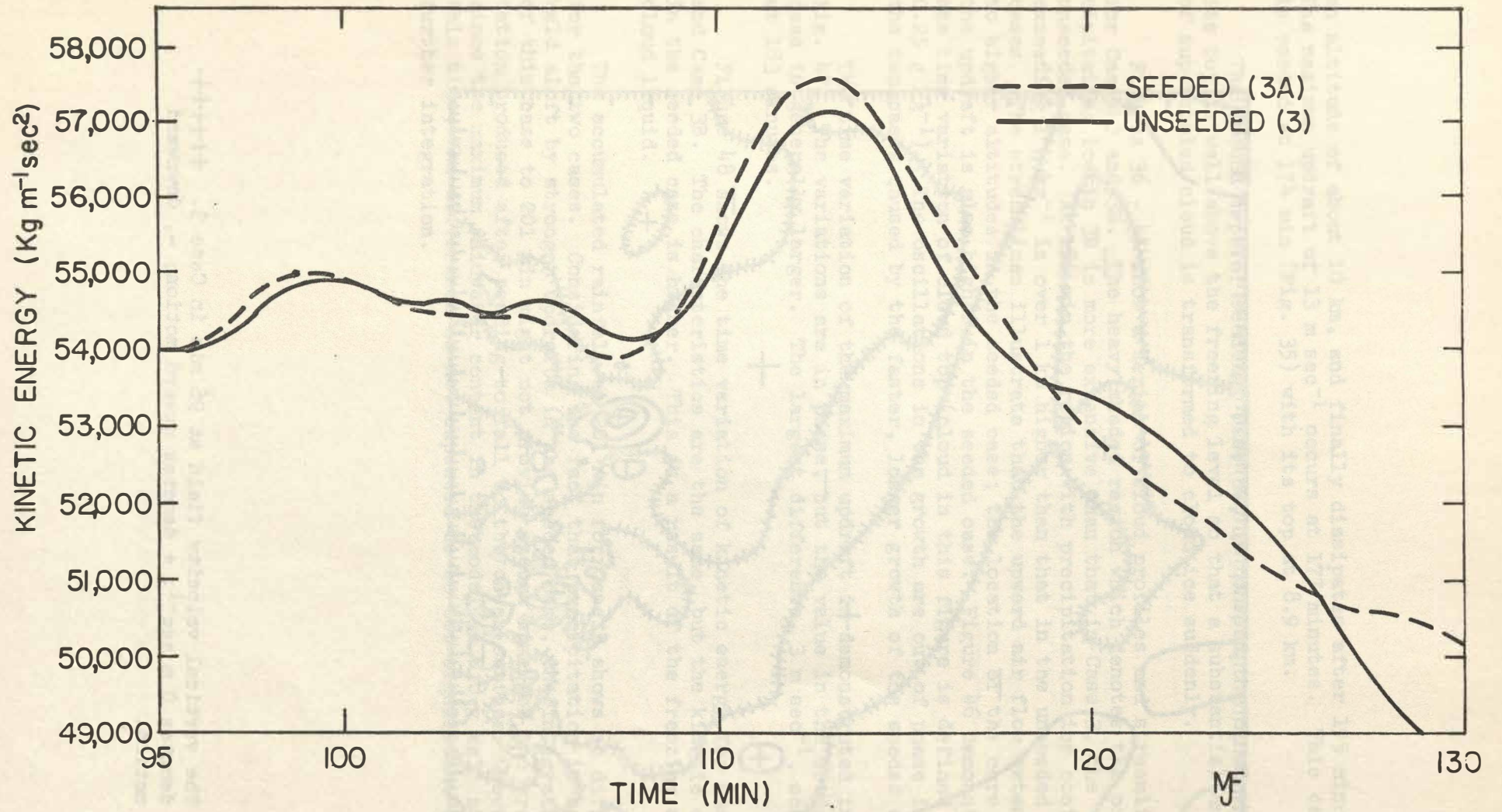


Fig. 33. Time variation of kinetic energy for Cases 3 and 3A.

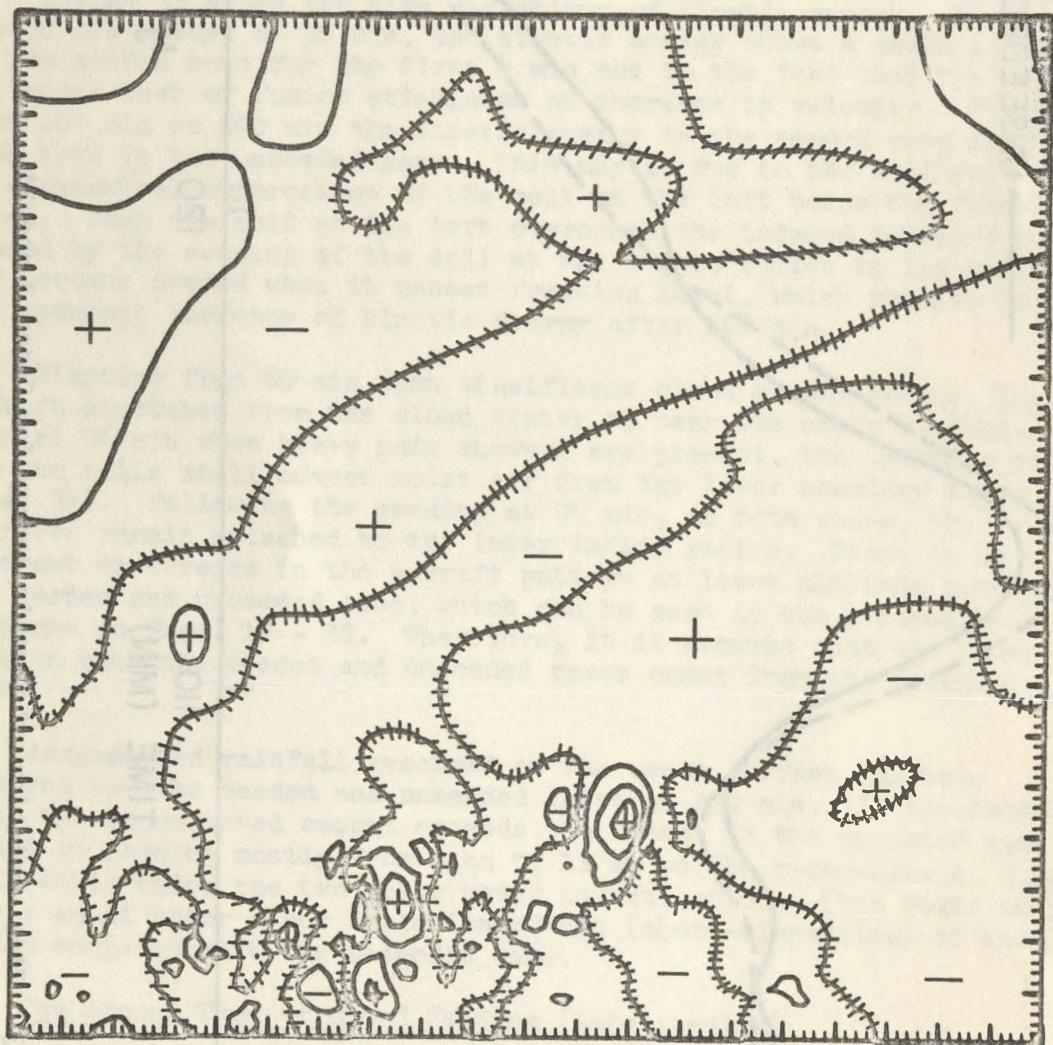


Fig. 34. The vertical velocity field at 96 min in Case 3. $+++++$ denotes 0 m sec^{-1} ; + denotes upward motion; -, downward motion.

an altitude of about 10 km, and finally dissipates after 195 minutes. The maximum updraft of 13 m sec^{-1} occurs at 177 minutes. This cell is seeded at 174 min (Fig. 35) with its top at 8.9 km.

The second type of seeding, Case 3B, is to seed the cloud when its top is well above the freezing level so that a substantial amount of supercooled cloud is transformed to cloud ice suddenly.

Figures 36 - 45 show a series of cloud profiles and streamlines for Cases 3 and 3B. The heavy shaded region which denotes the precipitating ice in 3B is more extensive than that in Case 3, the unseeded case. At 186 min the region with precipitation ice content exceeding 1 g kg^{-1} is over 1 km higher than that in the unseeded cases. The streamlines illustrate that the upward air flow extends to higher altitudes in the seeded case; the location of the core of the updraft is also higher in the seeded case. Figure 46 demonstrates the time variation of cloud top (cloud in this figure is defined as 0.25 g kg^{-1}). The oscillations in the growth are out of phase in the two cases caused by the faster, longer growth of the seeded cloud.

The time variation of the maximum updraft is demonstrated in Fig. 47. The variations are in phase, but the value in the seeded case is generally larger. The largest difference, 3 m sec^{-1} , occurs at 183 minutes.

Figure 48 shows the time variation of kinetic energy for Case 3 and Case 3B. The characteristics are the same, but the kinetic energy in the seeded case is higher. This is a result of the freezing of the cloud liquid.

The accumulated rainfall at 201 min for Case 3 shows no difference for the two cases. Considering the fact that precipitation is being held aloft by stronger updrafts in the seeded case, the integration of this case to 201 min might not provide enough time for the precipitation produced after seeding to fall to the ocean surface. However, since the maximum rainwater content in the model is 0.8 g kg^{-1} at this time, the difference is not expected to be too significant in further integration.

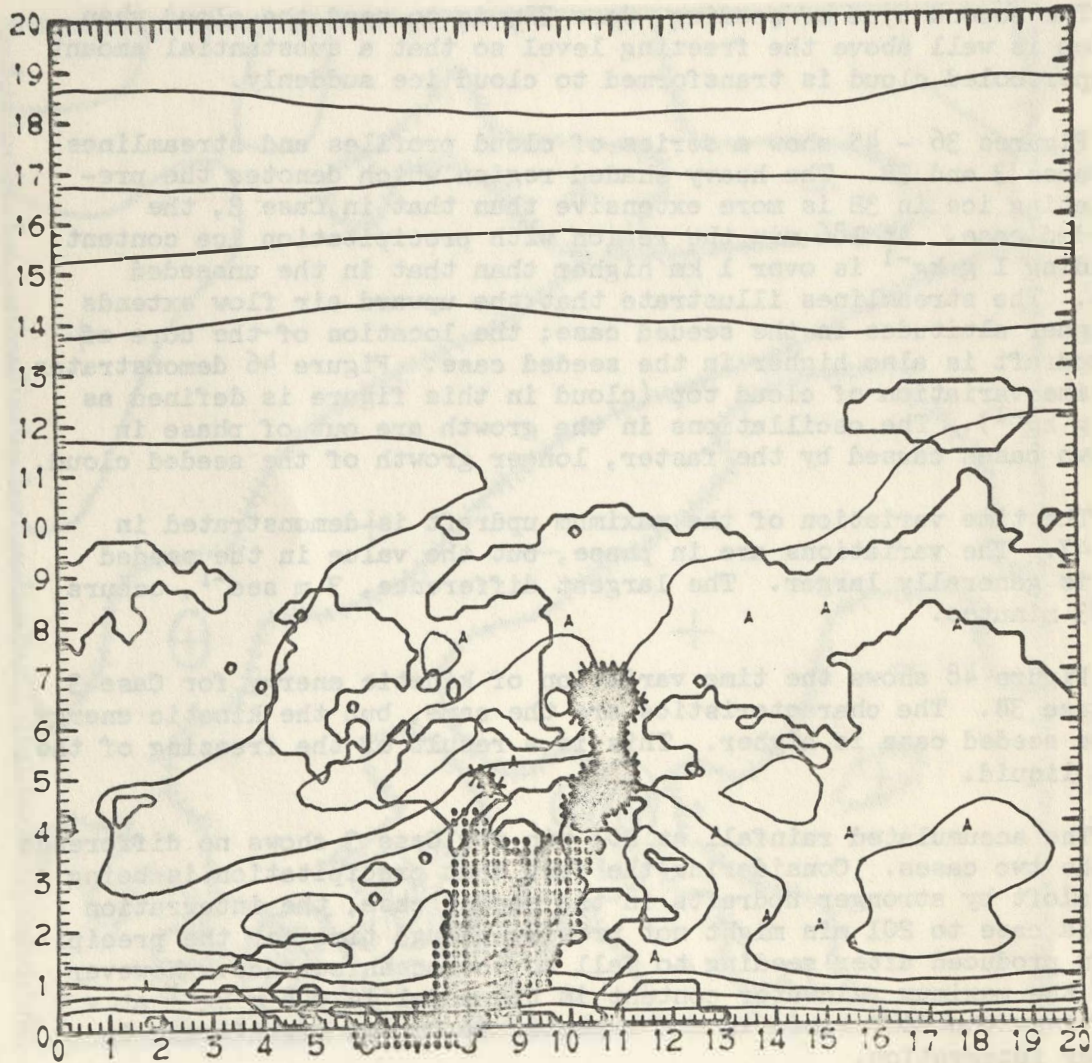


Fig. 35. Case 3 at 174 min.

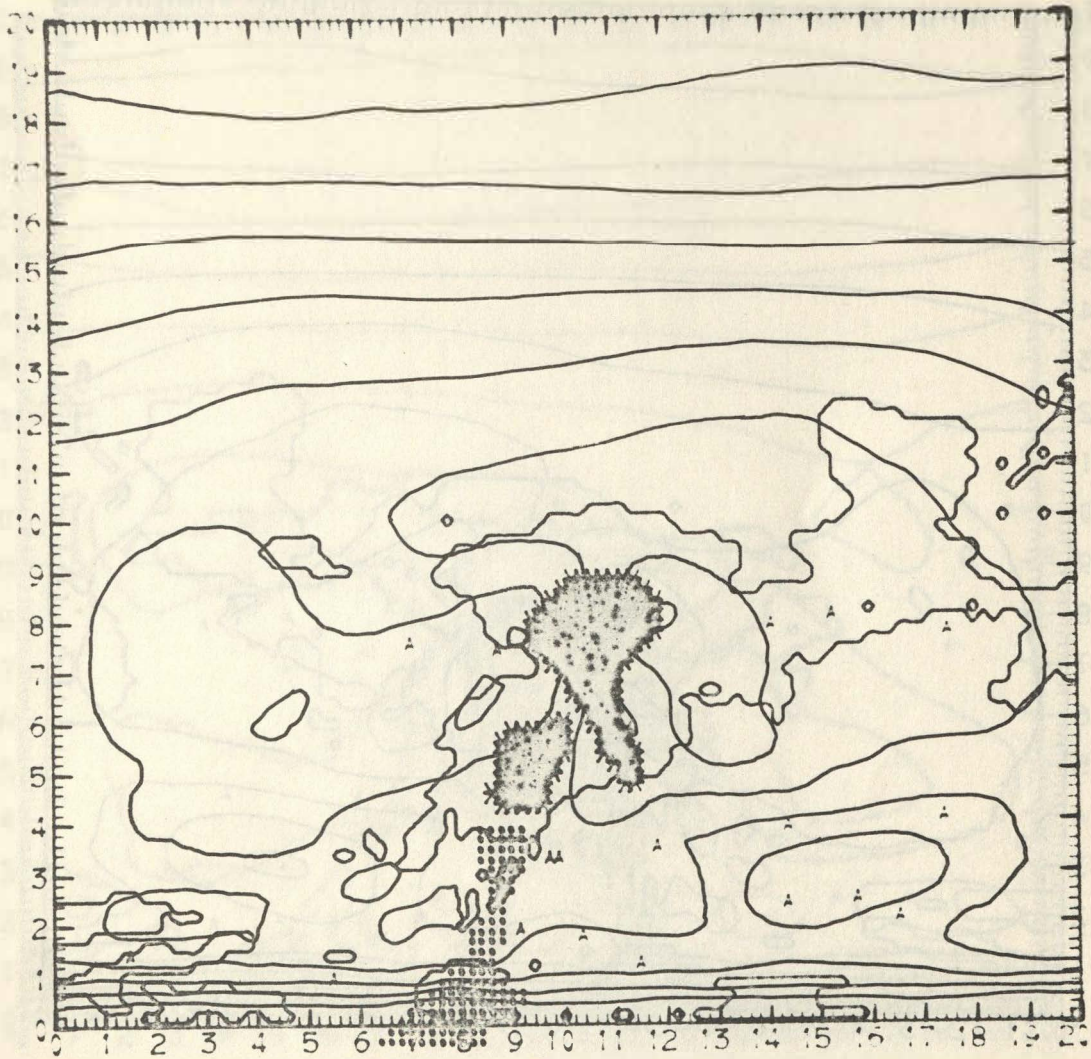


Fig. 36. Case 3 at 180 min.

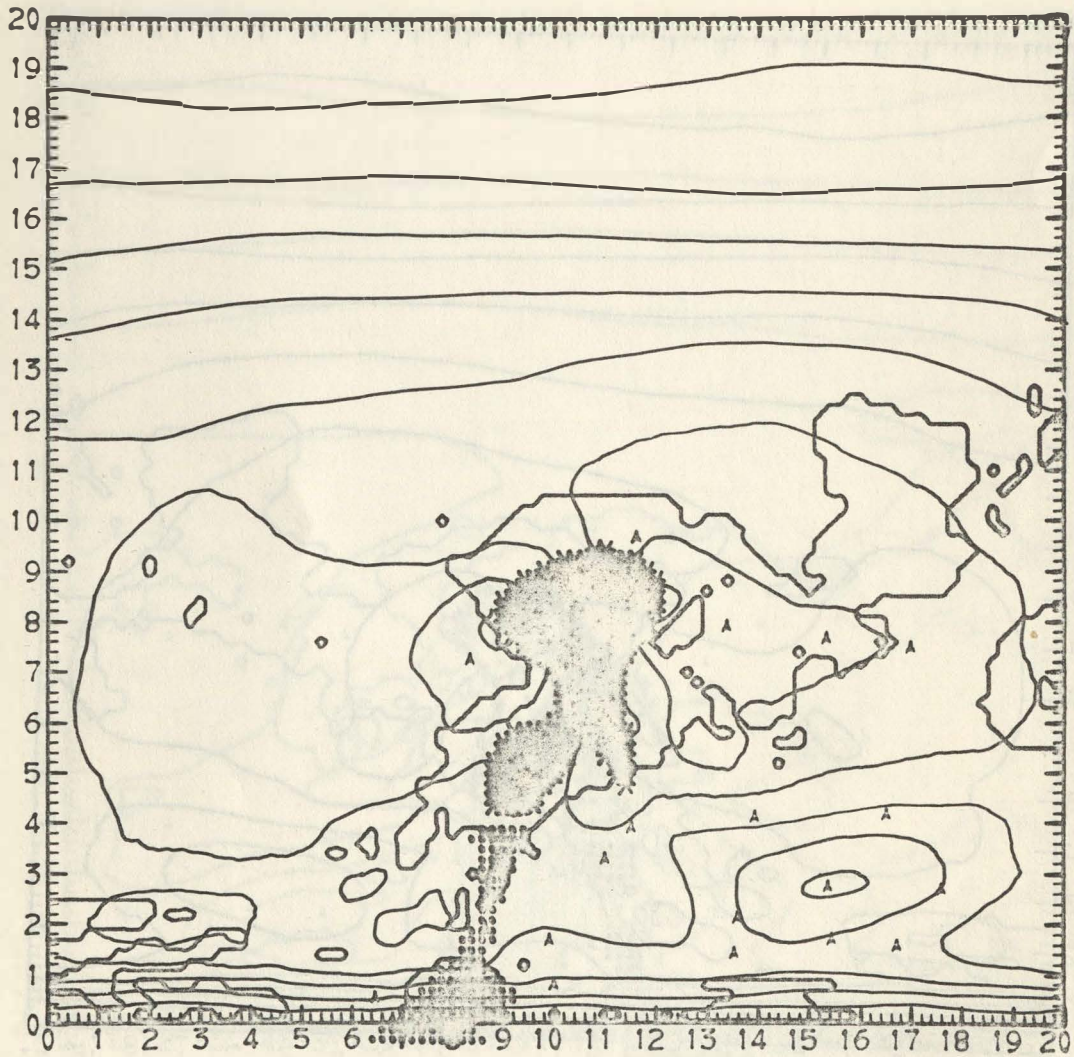


Fig. 37. Case 3B at 180 min.

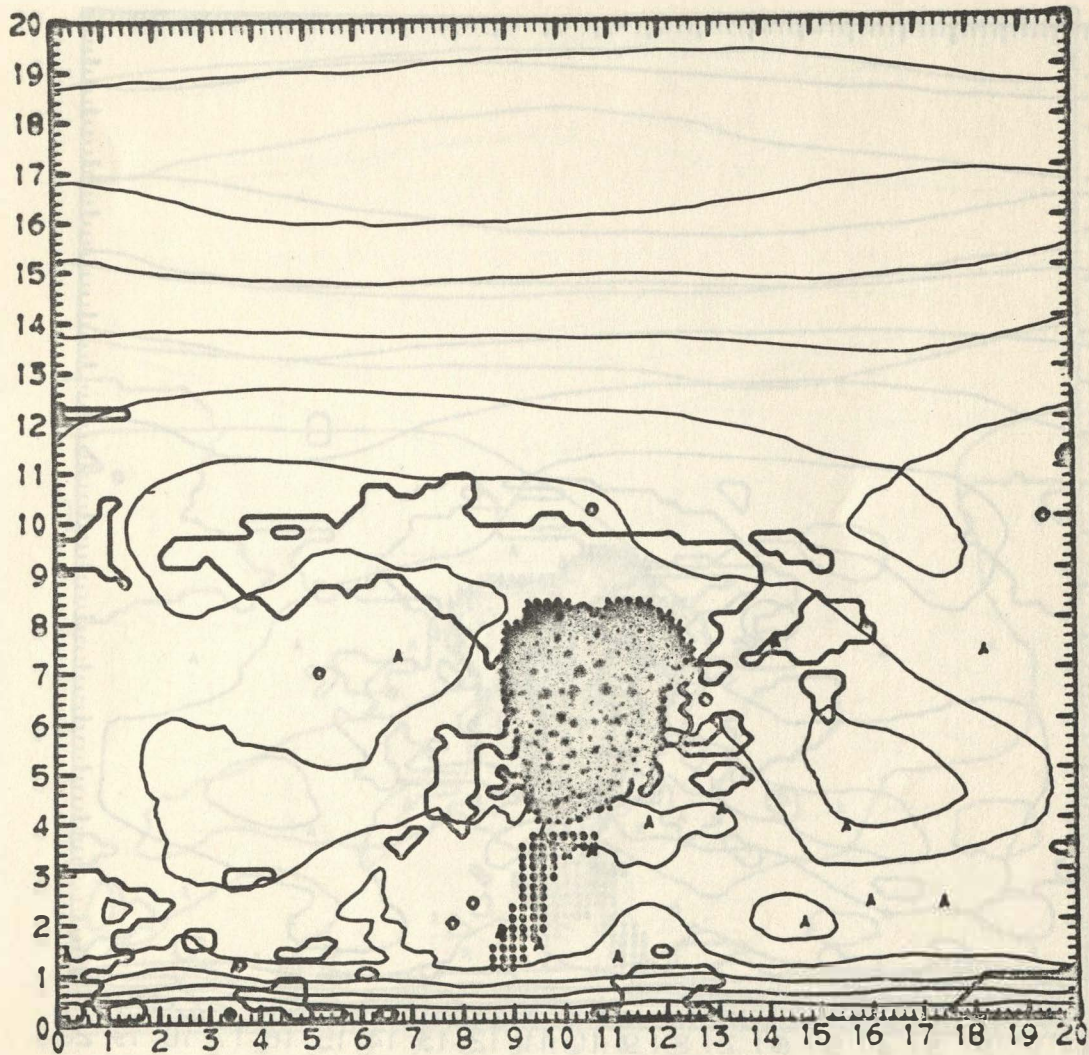


Fig. 38. Case 3 at 186 min.

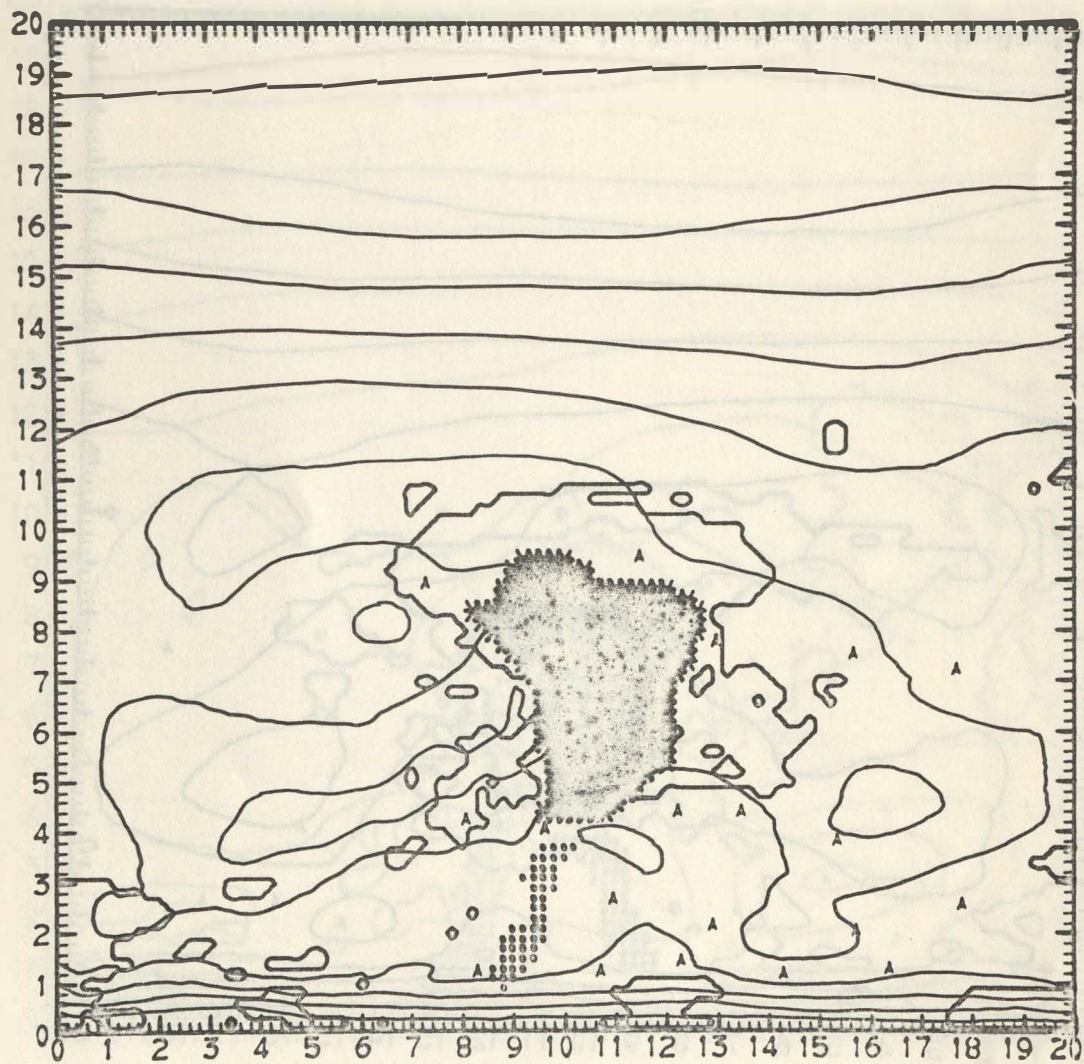


Fig. 39. Case 3B at 186 min.

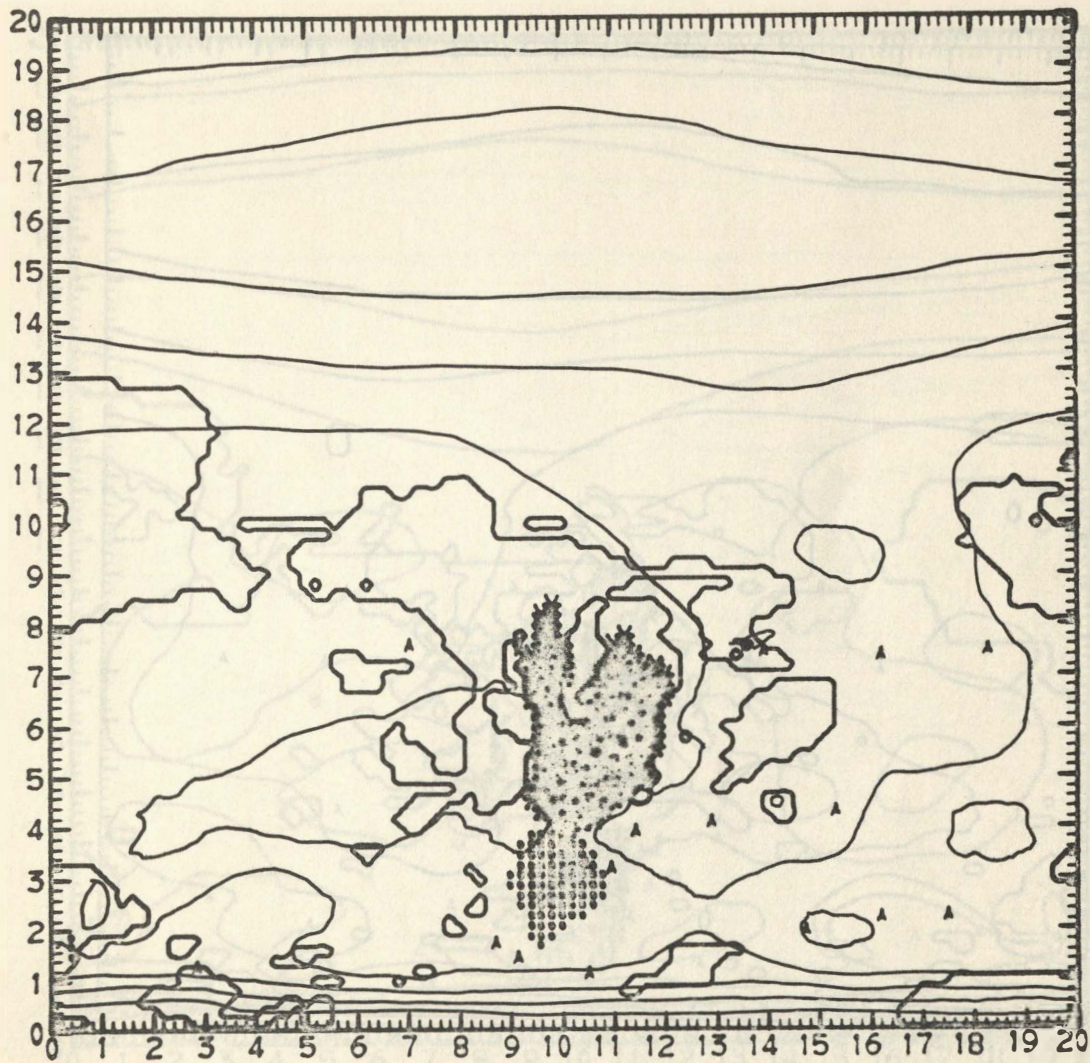


Fig. 40. Case 3 at 189 min.

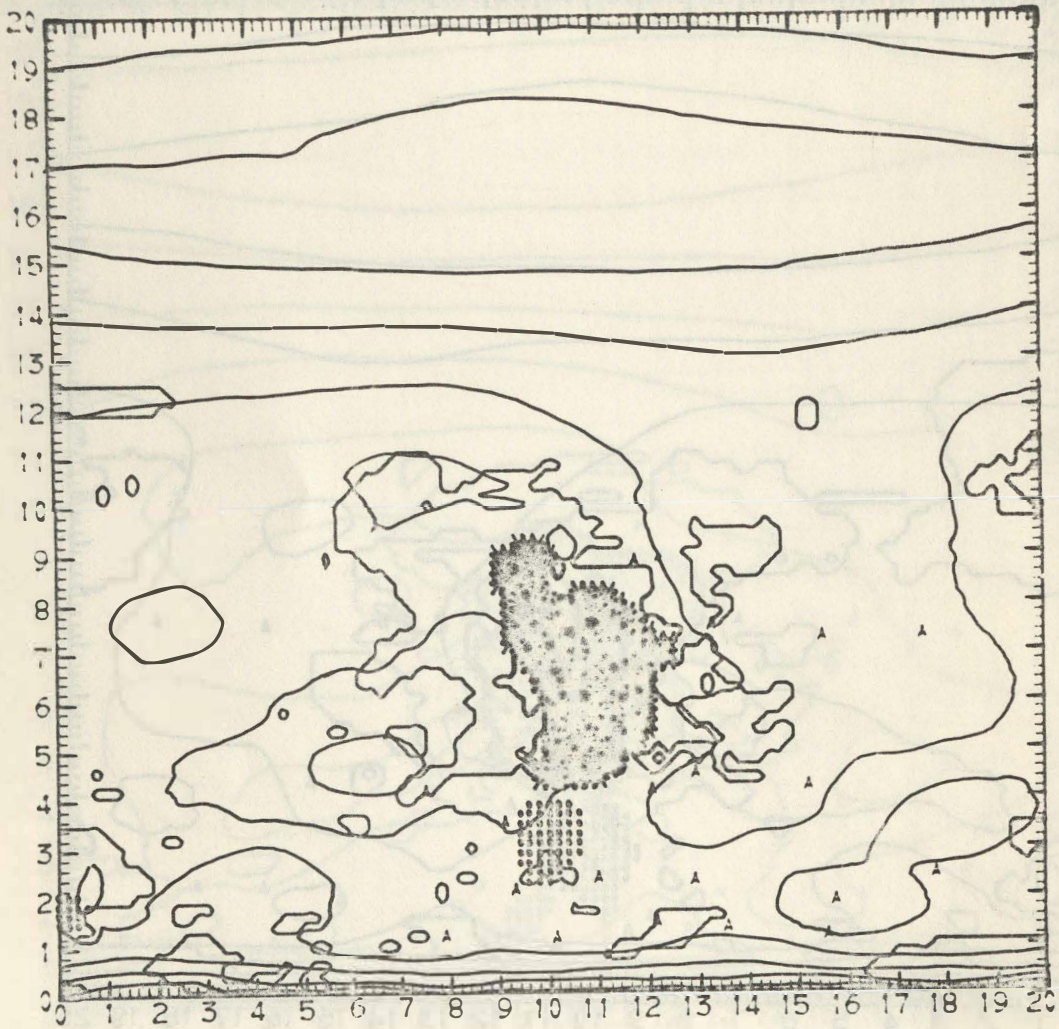


Fig. 41. Case 3B at 189 min.

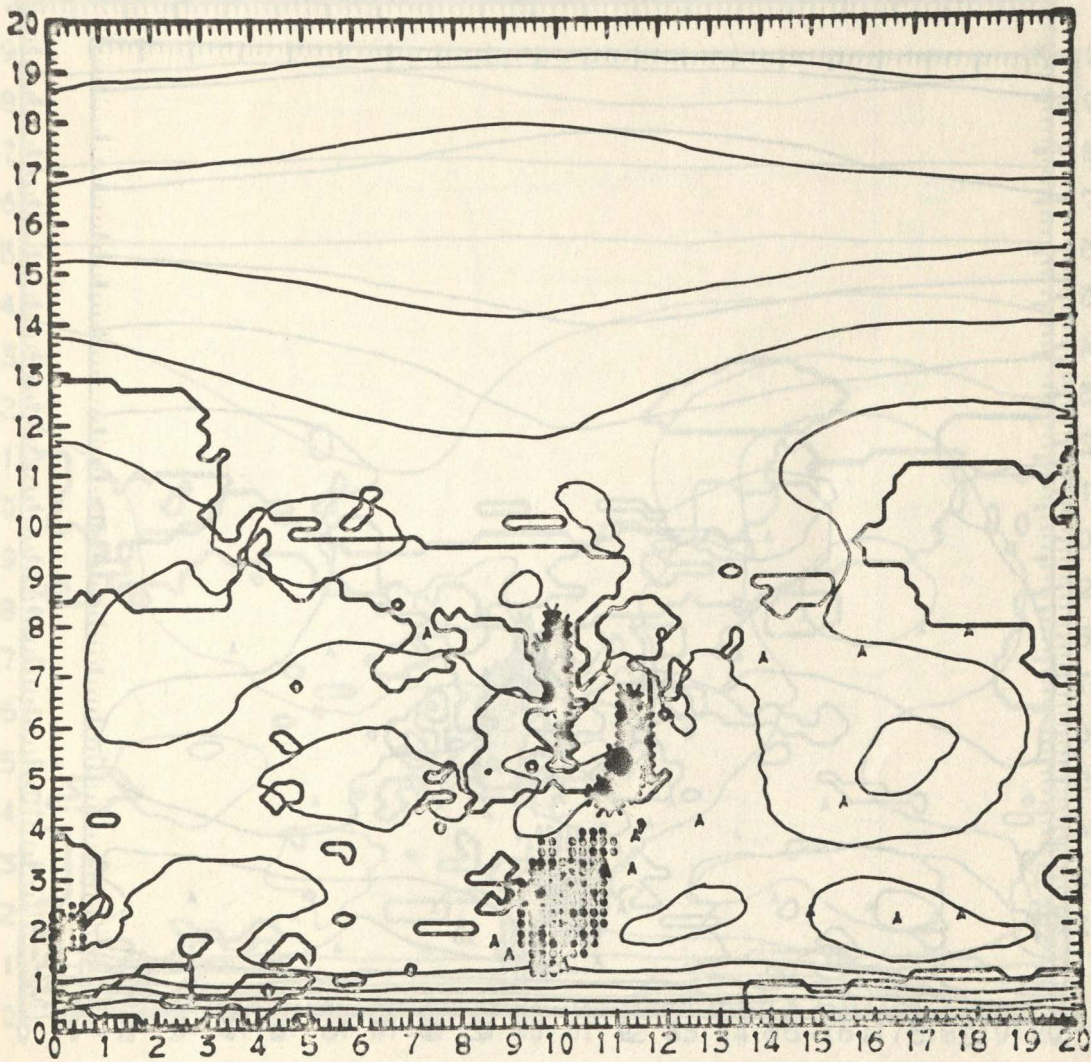


Fig. 42. Case 3 at 192 min.

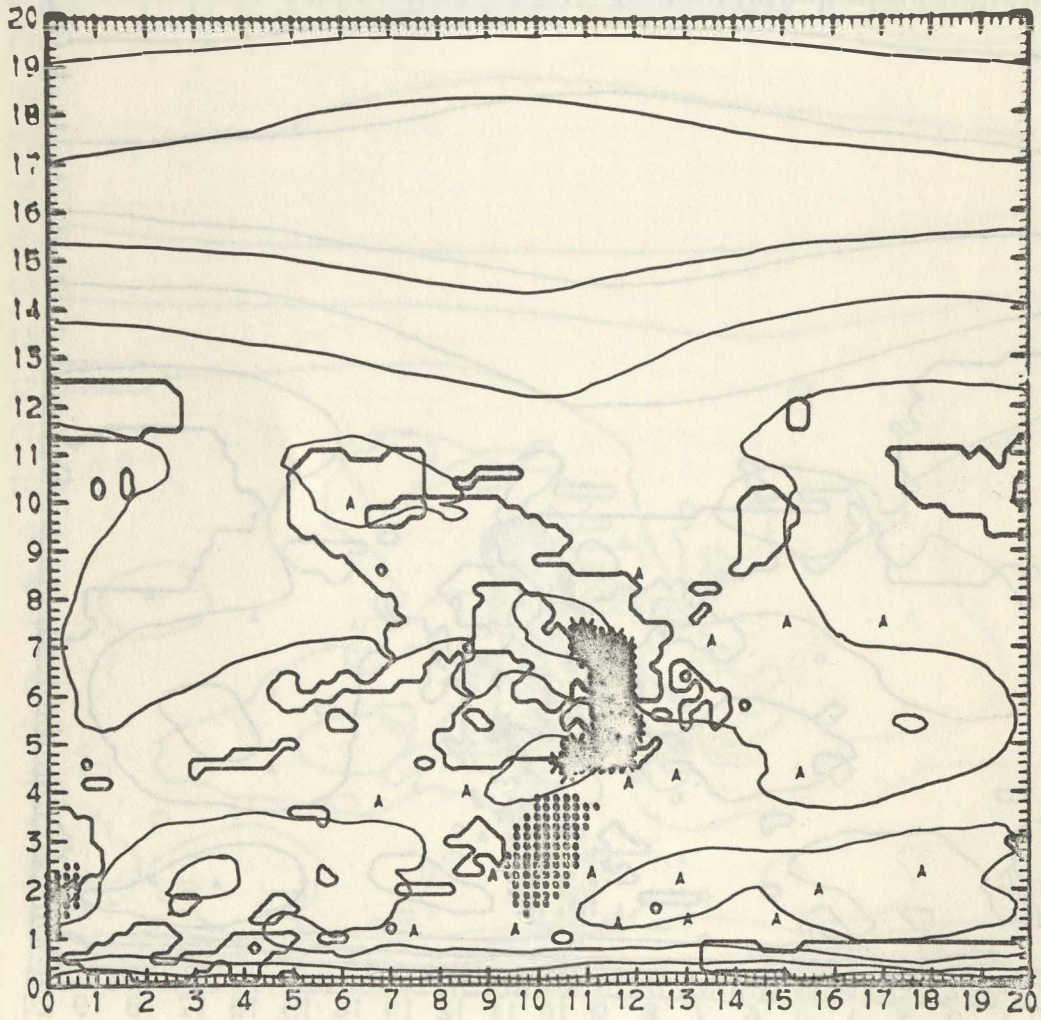


Fig. 43. Case 3B at 192 min.

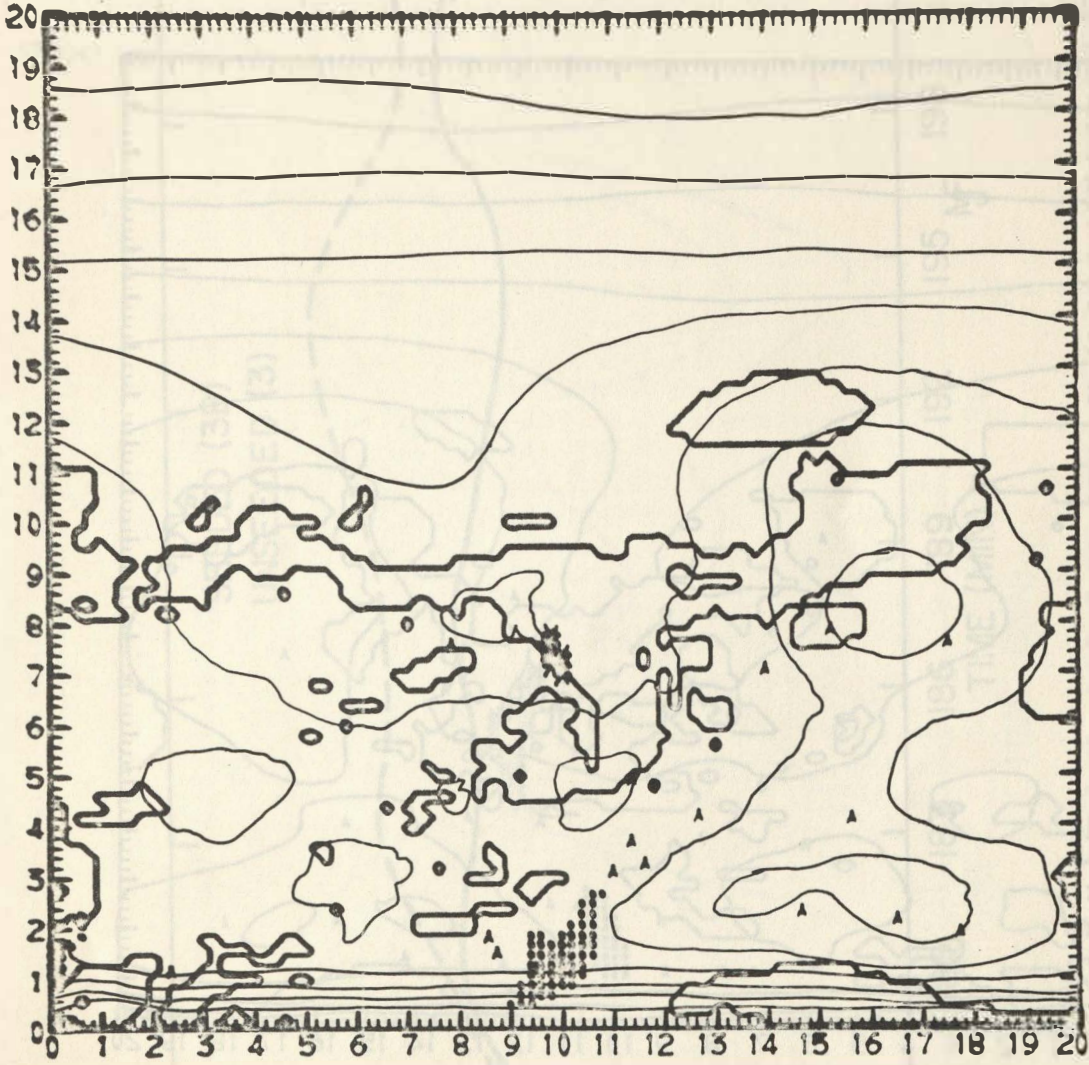


Fig. 44. Case 3 at 195 min.

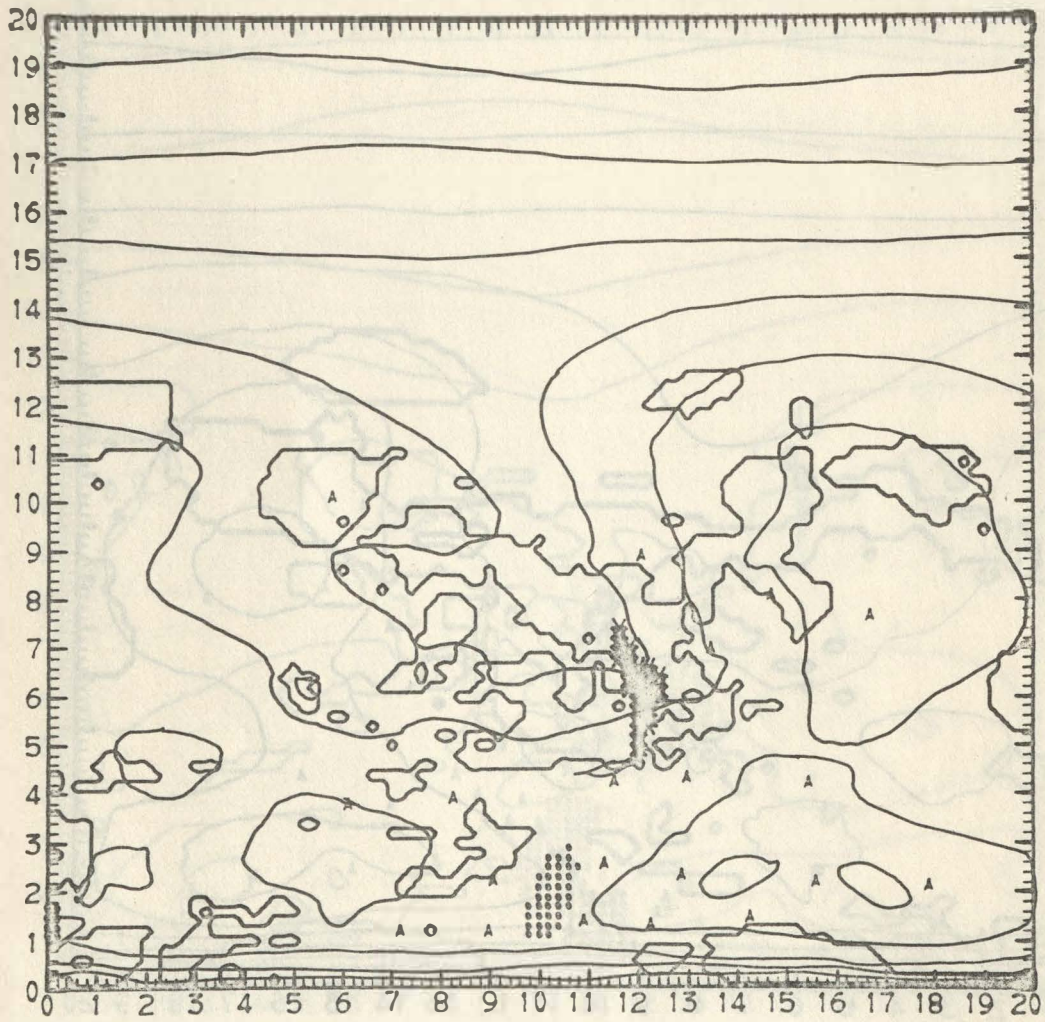


Fig. 45. Case 3B at 195 min.

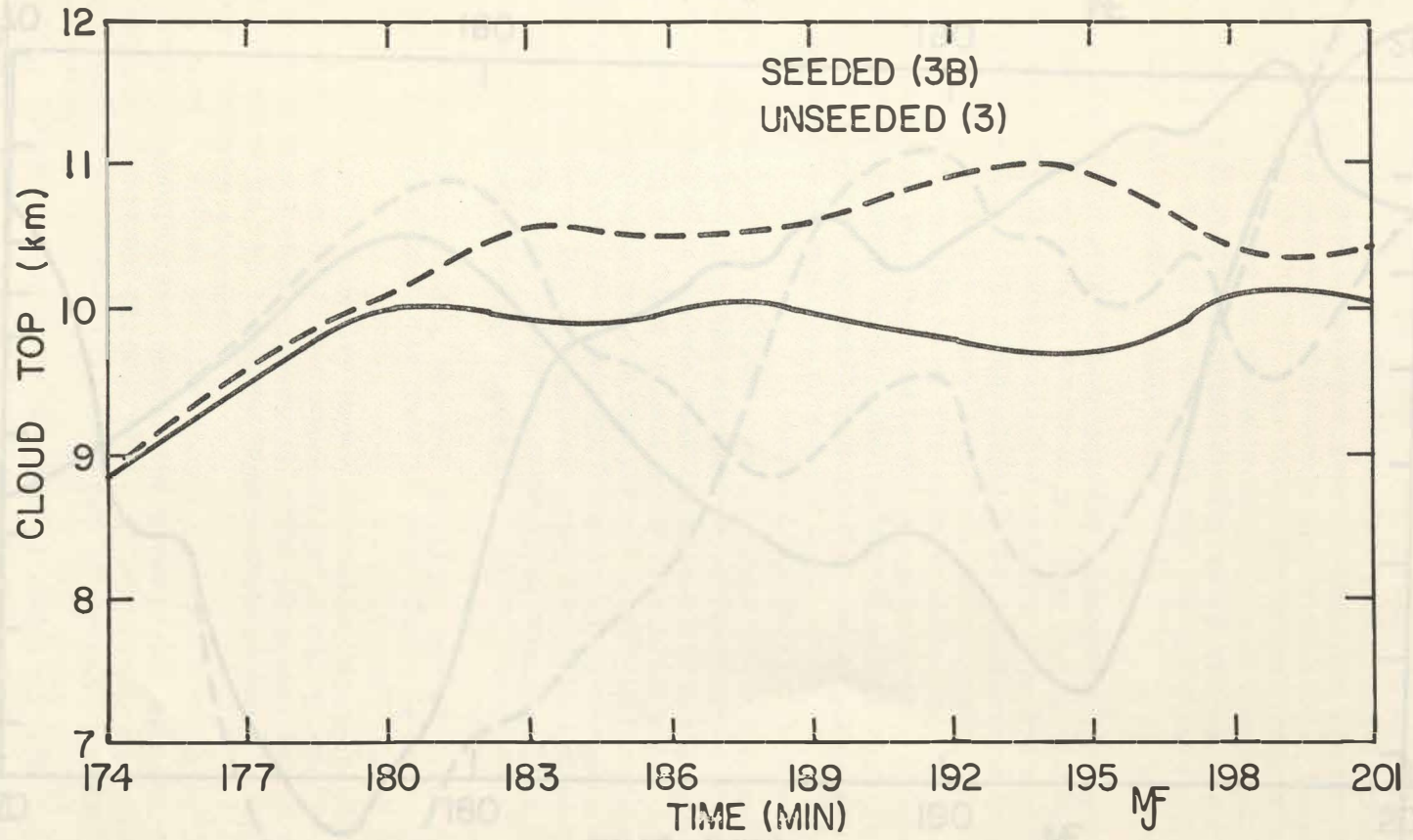


Fig. 46. Time variation of cloud tops in Case 3 and Case 3B. Cloud tops defined as 0.25 g kg^{-1} CWC heights.

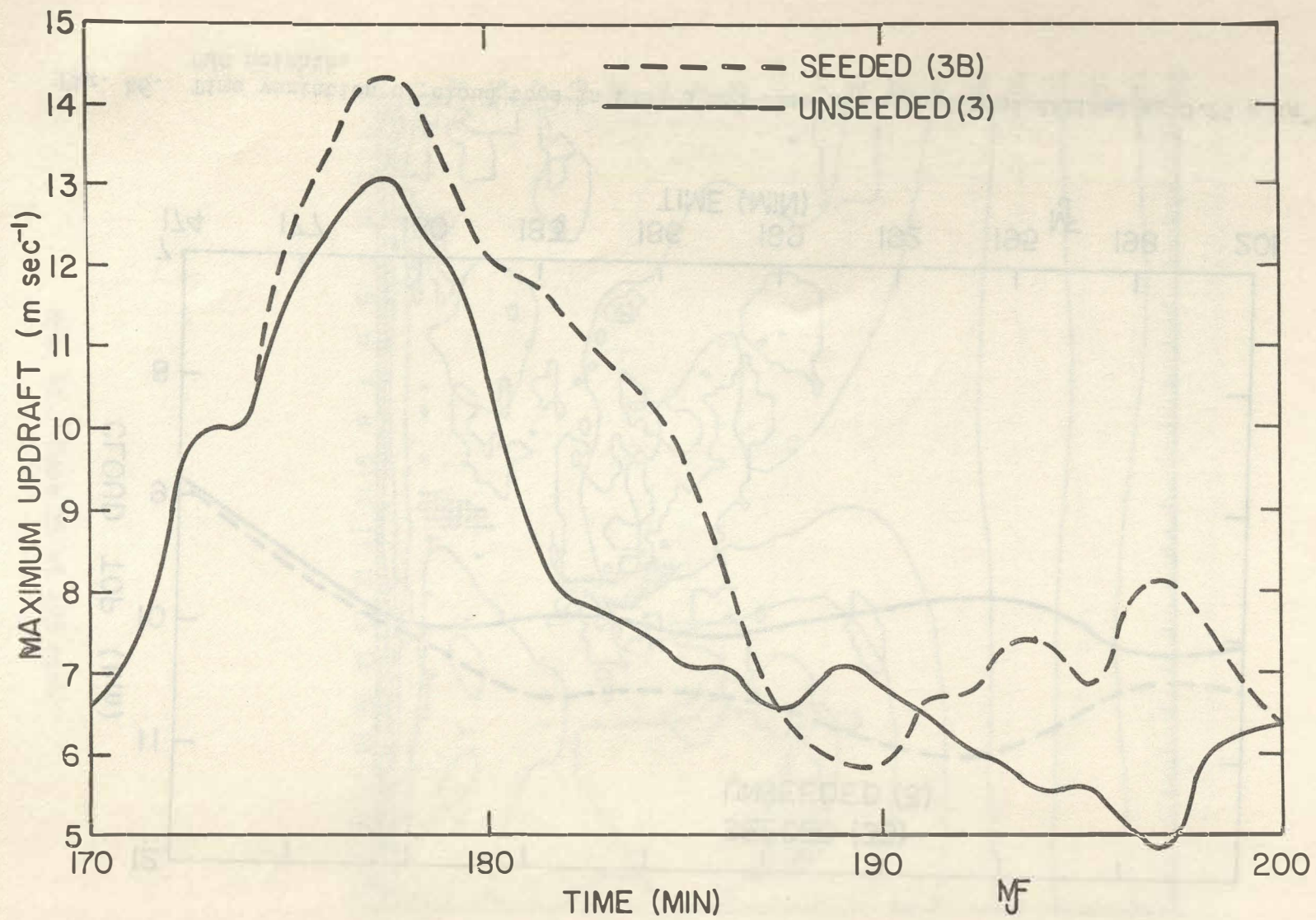


Fig. 47. Time variation of maximum updrafts in Cases 3 and 3B.

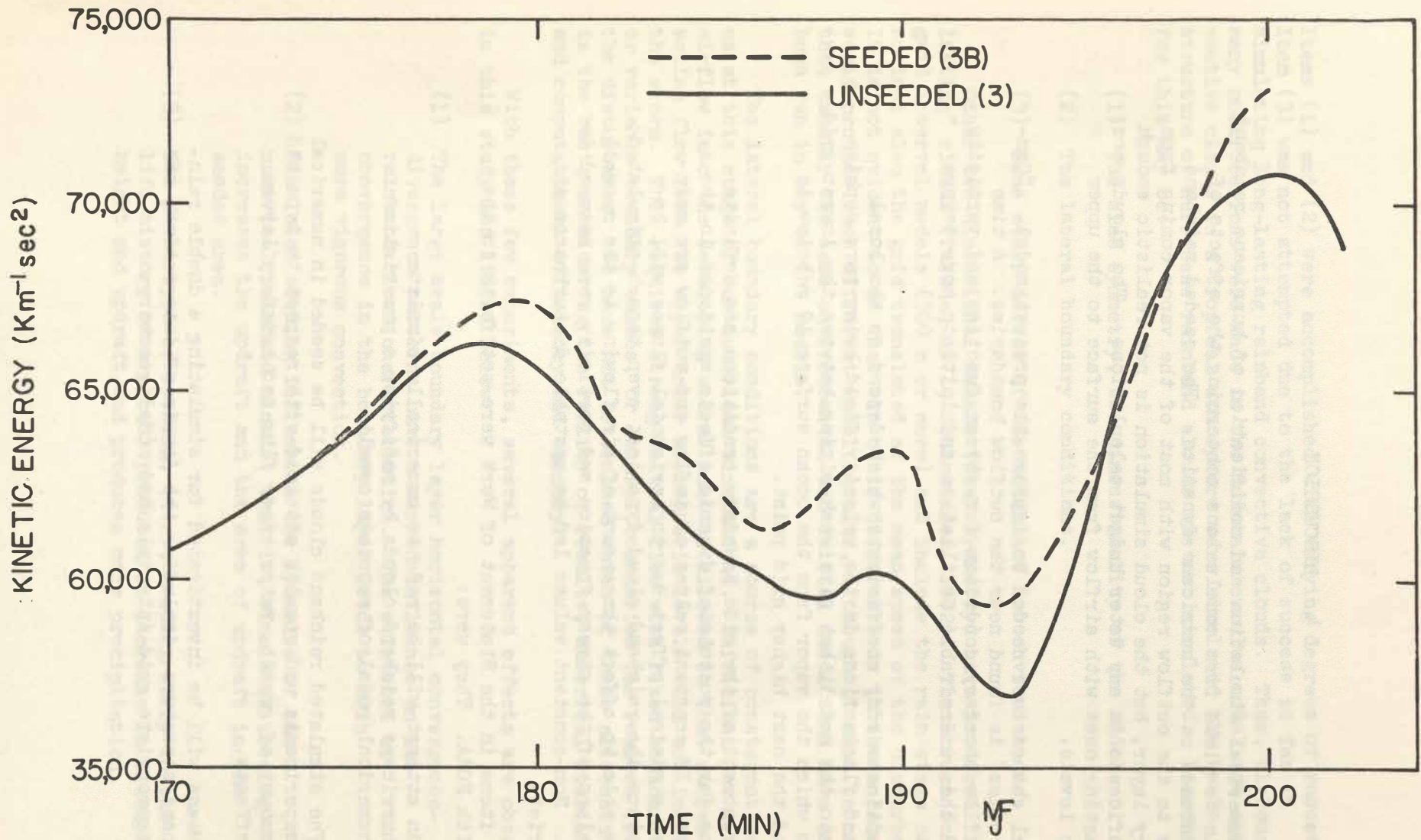


Fig. 48. Time variation of kinetic energy in Cases 3 and 3B.

4. DISCUSSION

This numerical simulation and modification of hurricane rainband clouds fails to yield firm conclusions concerning the effects of seeding rainbands on the hurricane dynamics. The seeded rainband clouds grow to the outflow region with most of the vapor coming from the boundary layer, but the cloud simulation is not realistic enough to give confidence in any water budget calculations. The clouds are not long lasting ones with airflow from the surface to the upper atmospheric levels.

Several changes are needed to improve the present model. "Computational noise" is found near the outflow boundaries. A time varying outflow boundary condition for stream function and vorticity might avoid this undesirable oscillation and initiate more severe convection.

The nonlinear eddy coefficients which depend on the local stability and fluctuations in the velocity field bring more sophistication into the model, but give weak mixing between the lowest grid points into which the vapor from the ocean surface 10 m below is diffused and the next higher grid point.

The treatment of the side boundary conditions has definite implications for the postulated dynamic effects mentioned in the introduction. If constant values of inflow and outflow are maintained, then a minimal effect due to horizontal fluxes will be observed, since the rainband cloud dynamics, even though stimulated, will not be able to affect the amount of air flowing to the eyewall. Constant values of the stream function and vorticity were assumed in this study. Non-constant values led to unstable disturbances at the boundaries.

Three items in the Statement of Work were set forth in the contract with NOAA. They were:

- (1) An attempt will be made to numerically simulate hurricane rainband clouds by modifying a preexisting numerical model of mountain cumuli.
- (2) The simulated rainband clouds will be seeded in numerical experiments and results obtained with respect to type and amount of growth, water vapor flux and boundary layer effects.
- (3) Means will be investigated for simulating a double rainband structure, including the domain of integration, the appropriate grid intervals and model geometry.

Items (1) and (2) were accomplished with varying degrees of success. Item (3) was not attempted due to the lack of success so far in simulating long-lasting rainband convective clouds. Thus, although many modifications were made in the mountain cumulus model and convective clouds in a tropical atmosphere were simulated the basic structure of hurricane rainband clouds was not simulated. Reasons for this may be:

- (1) The slab symmetry, two-dimensionality of the model.
- (2) The lateral boundary conditions.
- (3) Some other defect of the model not now obvious to us.

Other two-dimensional models (slab symmetry) have produced "long lasting" clouds (Takeda, 1971, Schlesinger, 1972). These were coarse grid interval models (500 m or more) and include the rain stage only--no ice; also the grid translated at the mean speed of the disturbance. It is not evident to us what the basic difference is in the models that would produce such different model results, although it must be noted that exactly the same environmental and initial conditions have not been run in any of the models.

The lateral boundary conditions are a source of consternation to us at this stage of our numerical simulations. Sufficient low level airflow into the developing storms must be allowed so that compensating flow from the upper drier atmospheric levels will not inhibit the storm. This requires strong initial flow with fixed boundaries, or variable boundary values, or lateral boundaries far removed from the disturbance. We have not determined which of these alternatives is the best, considering the reality of results, numerical stability, and computational efficiency and economy.

With these few experiments, several apparent effects are observed in this study and listed below:

- (1) The large scale boundary layer horizontal convergence-divergence patterns have a marked influence on the rainband cloud characteristics. The existence of convergence in the boundary layer leads to much more vigorous convection.
- (2) Simulated seeding influences the dynamics of the numerical rainband clouds; that is, simulated seeding increases the updraft and the area of updraft in the seeded area.
- (3) The first type of seeding, (i.e., seeding early in the life history of a cloud) produces an increase in cloud height and updraft and produces more precipitation.

- (4) The second type of seeding (i.e., seeding late in the life of a cloud) produces large increases in cloud updraft, but little increase, if any, in precipitation.
- (5) The model clouds are more vigorous when a low altitude jet exists in the rainband region.
- (6) Single cloud seeding or small scale seeding, suppresses nearby clouds in the rainband.

ACKNOWLEDGMENTS

The authors thank Dr. C. S. Chen who assisted in the formulation and discussion of the cloud physics equations.

The computations have been done at the Computation Center, South Dakota School of Mines and Technology, and the Computing Facility, National Center for Atmospheric Research, which is sponsored by the National Science Foundation. The personnel at these facilities have been most cooperative.

This research was performed under the sponsorship of the U. S. Department of Commerce, National Oceanic and Atmospheric Administration under a contract with the National Hurricane Research Laboratory, Grant No. N22-3-72(G).

REFERENCES

- Anthes, R. A., 1971: The response of a three-level axisymmetric hurricane model to artificial redistribution of convective heat release. Reprint of NHRL Tech. Memo.
- Berry, E. X., 1968: A parameterization of the collection of cloud droplets. Presented at the First Conference on Weather Modification, Albany.
- Bigg, E. K., 1953: The supercooling of water. Proc. Phys. Soc. B, 66, 668.
- Douglas, R. H., 1960: Size distributions, ice contents and radar reflectivities of hail in Alberta. Nubila, 3.
- Drake, R. L., 1969: Interacting convective cells in a two-dimensional anelastic system: dry convection. Preprint, National Center for Atmospheric Research, Boulder, Colorado.
- Kessler, E., 1969: On the distribution and continuity of water substance in atmospheric circulations. Meteor. Monogr., 10, No. 32, 84 pp.
- Lavoie, R. L., 1968: A mesoscale numerical model and lake-effect storm. Ph.D. Dissertation, The Penn State University.
- Liu, J. Y., and H. D. Orville, 1969: Numerical modeling of precipitation and cloud shadow effects on mountain-induced cumuli. J. Atmos. Sci., 26, 1283-1298.
- Orville, H. D., 1965: A numerical study of the initiation of cumulus clouds over mountainous terrain. J. Atmos. Sci., 22, 684-699.
- _____, 1968: Ambient wind effects on the initiation and development of cumulus clouds over mountains. J. Atmos. Sci., 25, 385-403.
- _____, and L. J. Sloan, 1970: A numerical simulation of the life history of a rainstorm. J. Atmos. Sci., 27, 1148-1159.
- Rosenthal, S. L., 1971: A circularly symmetric primitive-equation model of tropical cyclones and its response to artificial enhancement of the convective heating function. Mon. Wea. Rev., 99, 414-426.
- Saunders, P. M., 1957: The thermodynamics of saturated air: A contribution to classical theory. Quart. J. Roy. Meteor. Soc., 83, 342-350.

- Schlesinger, R. E., 1971: A Numerical Model of Deep Moist Convection: The Influence of Ambient Conditions and Internal Physical Mechanisms. Annual Report 1971: Studies of the Atmosphere Using Aerospace Probing, Vol. 1: Theoretical Studies. Space Science and Engineering Center, University of Wisconsin.
- Sheets, R. C., 1969: Some mean hurricane soundings. J. Appl. Meteor., 8, 134-146.
- Simpson, J., G. W. Brier, and R. H. Simpson, 1967: Stormfury cumulus seeding experiment 1965: statistical analysis and main results. J. Atmos. Sci., 24, 508-521.
- Srivastava, R. C., 1967: A study of the effects of precipitation on cumulus dynamics. J. Atmos. Sci., 24, 36-45.
- Takeda, T., 1971: Numerical simulation of a precipitating convective cloud: the formation of a "long-lasting" cloud. J. Atmos. Sci., 28, 350-376.
- Takeuchi, D. M., 1968: Analysis of Hydrometer Sampler Data for ESSA Cumulus Experiments. Miami, Fla., 14 pp.
- Wisner, C., 1970: A numerical model of a cumulus cloud. Master's Thesis, South Dakota School of Mines and Technology, 92 pp.
- _____, H. D. Orville, and C. G. Myers, 1972: A numerical model of a hail-bearing cloud. J. Atmos. Sci., 29, 1160-1181.

APPENDIX 1

Stream Function Formulation

The initial stream function value in a case with no horizontal convergence is generated by the mathematical expression:

$$\psi_0(z) = -Az - \frac{B}{2}z^2 \quad (A1)$$

where ρ_0 is the initial air density, A is the radial flow velocity at $z=x=0$, and B is the vertical shear of radial flow (assumed to be linear).
By (8),

$$\rho_0 u = A + Bz \quad \text{and} \quad w = 0$$

In a case with superimposed horizontal convergence, the stream function value is generated by

$$\psi(x,z) = \psi_0(z) + C_1 x z' \quad (A2)$$

with

$$z' = \begin{cases} 0 & , \quad z > z_0 \\ z & , \quad z \leq z_0 \end{cases}$$

where z_0 is the depth of boundary layer, and C_1 is the magnitude of the superimposed horizontal convergence; that is,

$$\frac{\partial \rho_0 u}{\partial x} = \begin{cases} -C_1 & , \quad z \leq z_0 \\ 0 & , \quad z > z_0 \end{cases}$$

By (A2) and (8), the general upward motion initiated by this horizontal convergence in the boundary layer is

$$\rho_0 w = C_1 z$$

and the corresponding horizontal velocity is

$$\rho_0 u = A + Bz - C_1 X$$

Hence, the horizontal convergence is compensated by the vertical divergence at every point given by (5),

$$\nabla \cdot \rho_0 \mathbf{V} = \frac{\partial \rho_0 u}{\partial x} + \frac{\partial \rho_0 w}{\partial z} = -C_1 + C_1 = 0$$

For mass conservation in the model, horizontal divergence must be superimposed. The stream function then is generated by

$$\Psi(x, z) = \Psi_0(z) + C_2 x z'$$

with

$$z' = \begin{cases} z - z_1 & , \quad z_1 \leq z \leq z_2 \\ 0 & , \quad \text{otherwise} \end{cases}$$

where $z_2 - z_1$ is the depth of horizontal divergence layer, the C_2 is the magnitude of horizontal divergence given by

$$C_2 = - \frac{z_0 C_1}{(z_2 - z_1)}$$

Thus, the total mass convergence in the model is zero.

APPENDIX 2

List of Symbols

A_1	ventilation factor, 10
A'	constant in freeze equation, 0.66 C^{-1}
a	constant in terminal velocity formula, 2115 cm sec^{-1}
B'	constant in freeze equation, $10^{-4} \text{ cm}^{-3} \text{ sec}^{-1}$
b	constant in terminal velocity formula, 0.8
C_D	drag coefficient in Eq. (32), 0.003
c_D	drag coefficient for precipitating ice, 0.25
C_I	specific heat of ice, $2.093 \cdot 10^7 \text{ erg g}^{-1} \text{ K}^{-1}$
C_P	specific heat of air at constant pressure, $1.003 \cdot 10^7 \text{ erg g}^{-1} \text{ K}^{-1}$
C_w	specific heat of water, $4.186 \cdot 10^7 \text{ erg g}^{-1} \text{ K}^{-1}$
D	relative dispersion of raindrops, 0.5
E	$1/m - 1$, 0.608
E_w	Collection efficiency between cloud ice and precipitating ice, 0.1
e_{si}	equilibrium vapor pressure with respect to ice, mb
e_{sw}	equilibrium vapor pressure with respect to water, mb
F_x	fractional acceleration in x-direction
F_z	fractional acceleration in z-direction
g	acceleration of gravity, 9.8 m sec^{-2}
h	distance between ocean surface and lower boundary of model, 10 m
K_a	thermal conductivity, $\text{erg cm}^{-1} \text{ sec}^{-1} \text{ K}^{-1}$
K_h	eddy coefficient for heat, $\text{m}^2 \text{ sec}^{-1}$

K_m	eddy coefficient for momentum, $m^2 \text{ sec}^{-1}$
K_1	lower limit for K_m , $8 \text{ m}^2 \text{ sec}^{-1}$
K_2	upper limit for K_m , $800 \text{ m}^2 \text{ sec}^{-1}$
K_3	upper limit for Richardson number used, 1
L	latent heat of condensation of sublimation, erg g^{-1}
L_f	latent heat of fusion, erg g^{-1}
L_s	latent heat of sublimation, erg g^{-1}
L_v	latent heat of condensation, erg g^{-1}
l_c	$l_{CI} + l_{CW}$, cloud substance, g g^{-1}
l_{CI}	cloud ice content, g g^{-1}
l_{CW}	cloud water content, g g^{-1}
l_I	graupel water content, g g^{-1}
l_R	rainwater content, g g^{-1}
m	ratio of molecular weights of dry air and water
N_{OR}	constant in parameterization of raindrop size distribution, 0.08 cm^{-4}
N_{OI}	constant in parameterization of graupel size distribution, 0.8 cm^{-4}
N_1	raindrop concentrate drops cm^{-3} preference pressure, 1,000 mb
P	pressure, mb
P_I	production of graupel from cloud substances, $\text{g g}^{-1} \text{ sec}^{-1}$
P_{IR}	production of graupel from rain, $\text{g g}^{-1} \text{ sec}^{-1}$
P_R	production of rain, $\text{g g}^{-1} \text{ sec}^{-1}$
R	universal gas content, $8.31436 \times 10^7 \text{ erg g}^{-1} \text{ K}^{-1}$
Re	Reynold number
R_v	gas constant for vapor, $0.4616 \times 10^7 \text{ erg g}^{-1} \text{ K}^{-1}$

r	water vapor mixing ratio, $g\ g^{-1}$
r_e	environment water vapor mixing ratio, $g\ g^{-1}$
r_s	saturation water vapor mixing ratio, $g\ g^{-1}$
r_{si}	r_s over ice
r_{sw}	r_s over water
S	saturation ratio
T	temperature, K
T_c	temperature, C
T_{∞}	reference temperature, 298.2 K
t	time, sec
u	horizontal velocity, $m\ sec^{-1}$
U_t	mass-weighted mean terminal velocity of precipitating ice, $m\ sec^{-1}$
V	resultant velocity, $m\ sec^{-1}$
V_t	mass-weighted mean terminal velocity of rain, $m\ sec^{-1}$
w	vertical velocity, $m\ sec^{-1}$
α_I	autoconversion rate of precipitating ice, $4 \times 10^{-3}\ sec^{-1}$
β	evaporation rate of precipitating ice, $3 \times 10^{-4}\ sec^{-1}$
Γ	gamma function
η	vorticity, $kg\ m^{-3}\ sec^{-1}$
Λ	parameter in rain size distribution, cm^{-1}
λ	mixing length, m
λ_I	parameter in precipitating ice size distribution, cm^{-1}
λ_R	parameter in raindrop size distribution, cm^{-1}
κ	R/CP , 0.2857
ν	kinematic viscosity, $cm^2\ sec^{-1}$
π	3.14159

π_0	a reference value for $\bar{\pi}$, 1
ρ	air density, g cm^{-3}
ρ_0	initial air density, kg m^{-3}
ρ_I	ice density, g cm^{-3}
ρ_w	water density, g cm^{-3}
θ	reference potential temperature, K
θ'	potential temperature deviation, K
ϕ'	deviation of entropy
ψ	stream function, $\text{kg m}^{-1} \text{sec}^{-1}$
ψ	diffusivity of water vapor in air, $\text{cm}^2 \text{sec}^{-1}$

APPENDIX 3

Personnel Effort and Special Reports

A3.1 Several persons contributed significantly to the research. They are listed below with their effort in man months appended.

<u>Persons</u>	<u>Man Months</u>
H. D. Orville	1.05
S. W. Chang	6.00
F. J. Kopp	3.50
C. S. Chen	2.09
Secretaries	0.24

A3.2 Two papers concerning the research were presented at American Meteorological Society meetings. One paper has been submitted to the Journal of the Atmospheric Sciences. A thesis was completed by W. J. Chang. The titles are listed below.

Orville, H. D., and W. J. Chang, 1971: Numerical simulation of hurricane rainband clouds. Presented at the Seventh Technical Conference on Hurricanes and Tropical Meteorology, St. Michael Barbados, West Indies, December 6-9, 1971.

Chang, W. J., 1972: A numerical simulation of hurricane rainband clouds. Master's Thesis, South Dakota School of Mines and Technology, Rapid City, South Dakota, 35 pp.

_____, and H. D. Orville, 1972: Modification of hurricane rainband clouds: a numerical simulation. Preprints, Third Conf. on Wea. Mod., American Meteorological Society, Boston, Massachusetts, 336 pp.

_____, and _____, 1972: Large scale convergence in a numerical cloud model. Submitted to Notes and Correspondence section, J. Atmos. Sci.